

Investigating the metabolic and genetic regulation of ageing using forward genetics screens

Inaugural-Dissertation zur
Erlangung des Doktorgrades
der Mathematisch-Naturwissenschaftlichen Fakultät
der Universität zu Köln




vorgelegt von

Felix Alois Mathias Cornelis Mayr

aus Nieuwegein, die Niederlande

14 Februar 2022, Köln, Deutschland

The image features three nematodes, likely C. elegans, arranged diagonally from the top-left to the bottom-right. The largest nematode on the left is curved and filled with many small, dark, oval-shaped eggs. The middle nematode is slightly smaller and also contains eggs. The smallest nematode on the right is very thin and appears to be a juvenile or young adult, with fewer and more distinct eggs visible. The background is a light, neutral color.

Getting old - is getting *old*.

Gutachter: Dr. Martin Denzel
Prof. Dr. Björn Schumacher

Tag der mündlichen Prüfung: 14 April 2022

Table of contents

Abstract.....	- 5 -
Abbreviations	- 6 -
1 Introduction.....	- 9 -
1.1 Ageing	- 9 -
1.1.1 Ageing demographics	- 9 -
1.1.2 Anti-ageing research funding.....	- 10 -
1.1.3 Life and characteristics of ageing	- 10 -
1.1.4 Theories of ageing	- 11 -
1.2 Model organisms for studying the ageing process.....	- 14 -
1.2.1 The roundworm <i>Caenorhabditis elegans</i>	- 14 -
1.2.2 The fruit fly <i>Drosophila melanogaster</i>	- 15 -
1.2.3 The mouse <i>Mus musculus</i>	- 15 -
1.3 Protein homeostasis	- 16 -
1.3.1 Protein homeostasis declines with ageing	- 16 -
1.3.2 Protein synthesis	- 17 -
1.3.3 Protein synthesis efficiency and fidelity	- 18 -
1.3.4 Chaperones are key to maintain protein homeostasis	- 19 -
1.4 Ribosome homeostasis	- 21 -
1.4.1 Ribosome biogenesis	- 21 -
1.4.2 Ribosome biogenesis (dys)regulation	- 22 -
1.4.3 Ribosome heterogeneity and mRNA translation specificity.....	- 23 -
1.5 Cellular metabolism.....	- 25 -
1.5.1 Amino acid homeostasis.....	- 26 -
1.5.2 Dietary restriction	- 26 -
1.5.3 Methionine restriction	- 27 -
1.5.4 Polyamine metabolism	- 28 -
1.5.5 Proline metabolism	- 30 -
1.6 Forward genetic screens	- 32 -
1.7 Aims of this thesis	- 33 -
2 Results	- 34 -
2.1 The <i>wrm22</i> allele ameliorates G418 toxicity and extends lifespan	- 34 -
2.2 The SNP in <i>pycr-1</i> is the causal mutation of the <i>wrm22</i> allele	- 35 -
2.3 Alignment of <i>C. elegans</i> PYCR-1 and PYCR-1(<i>wrm22</i>) with <i>H. sapiens</i> PYCR1.....	- 36 -
2.4 <i>pycr-1(wrm22)</i> fecundity is mildly reduced	- 39 -

2.5	<i>pycr-1(wrm22)</i> G418 resistance is independent of proline level	39 -
2.6	<i>pycr-1(wrm22)</i> protein synthesis is mildly protected from inhibition	40 -
2.7	<i>pycr-1(wrm22)</i> is broadly resistant to ribosome inhibitors	41 -
2.8	<i>pycr-1(wrm22)</i> is resistant to oxidative and heat stress	42 -
2.9	SAM depletion leads to G418 resistance	43 -
2.10	SAM repletion abolishes G418 resistance and longevity in <i>pycr-1(wrm22)</i>	45 -
2.11	Proteome and translome analysis of <i>pycr-1(wrm22)</i>	46 -
2.12	<i>pycr-1(wrm22)</i> mitochondrial stress is not rescued by SAM repletion	48 -
2.13	<i>pycr-1(wrm22)</i> <i>irg-1</i> signaling is not rescued by SAM repletion	49 -
2.14	Dysregulated rRNA maturation in <i>pycr-1(wrm22)</i> associates with NRDE-3 nuclear localization, but not G418 resistance	49 -
2.15	Low SAM associates with small nuclei and is rescued by SAM repletion	53 -
2.16	<i>pycr-1(wrm22)</i> transcriptional changes match with histone H3 markers	54 -
2.17	HSF-1 target genes confer G418 resistance and longevity in <i>pycr-1(wrm22)</i>	56 -
2.18	SAM depletion is linked to HSF1 target gene expression in flies and mice	57 -
3	Discussion	60 -
3.1	G418 resistance screen enriches for novel long-lived mutants	61 -
3.2	The SNP in <i>pycr-1</i> is the causal mutation of the <i>wrm22</i> allele	61 -
3.3	Dimerization of PYCR-1 is possibly perturbed in <i>pycr-1(wrm22)</i>	62 -
3.4	Impaired <i>de novo</i> proline biosynthesis indirectly depletes SAM	62 -
3.5	Improved stress resilience of <i>pycr-1(wrm22)</i>	63 -
3.6	<i>pycr-1(wrm22)</i> phenocopies key aspects of methionine and dietary restriction	64 -
3.7	Does mTORC1 signaling play a role in <i>pycr-1(wrm22)</i> ?	64 -
3.8	Does the integrated stress response play a role in <i>pycr-1(wrm22)</i> ?	65 -
3.9	Does low SAM trigger a ribosome mediated hormetic stress response?	66 -
3.10	Which alternative mechanisms could link SAM depletion to longevity?	67 -
3.11	Therapeutic potential of PYCR1 inhibition	68 -
4	Materials & Methods	69 -
4.1	<i>C. elegans</i> strains and culture	69 -
4.2	Unbiased forward genetics G418 developmental resistance screen	69 -
4.3	Mutant Hawaiian SNP mapping and sequence analysis	69 -
4.4	Protein sequence alignment	69 -
4.5	Protein structures	70 -
4.5	Lifespan assays	70 -
4.6	RNAi experiments	70 -
4.7	Developmental G418 resistance assays	71 -

4.8	Developmental paraquat resistance assays	71 -
4.9	Heat stress survival assays.....	72 -
4.10	Generation time	72 -
4.11	Brood size assay	72 -
4.12	Metabolite analysis sample preparation.....	72 -
4.13	Polysome profiling.....	73 -
4.14	Polysome sequencing	74 -
4.15	Immunofluorescence assays	74 -
4.16	Quantitative Reverse Transcription-PCR (qRT-PCR).....	76 -
4.17	Protein extraction for proteomics.....	76 -
4.18	LC-MS/MS analysis for proteomics	76 -
4.19	Protein identification and quantification	77 -
4.20	Fly maintenance and survival analysis	77 -
4.21	RNA-Sequencing sample preparation of fly samples	78 -
4.22	Mouse dietary restriction (DR) protocol.....	78 -
4.23	Statistical analysis	79 -
Reference list		80 -
Supplementary Information		94 -
Appendix.....		104 -
Acknowledgments		104 -
Work contributions.....		106 -

Tuning of the proline-polyamine-SAM axis determines *C. elegans* lifespan extension

Abstract

Metabolic state, protein biogenesis, and the tuning of stress response pathways become dysregulated with ageing and their modification can prolong survival. Their coordinated interaction, however, remains poorly understood. In a forward genetic screen in *Caenorhabditis elegans* for resistance to the ribosomal inhibitor geneticin (G418), I discovered a mutation in the gene encoding for *pyrroline-5-carboxylate reductase-1* (*pycr-1*), responsible for the last step in *de novo* proline biogenesis. *pycr-1* mutant worms were long-lived, but had only slightly reduced proline levels. Intriguingly, I identified that low SAM induced by impaired *de novo* proline biosynthesis is required for *pycr-1* mutant G418 resistance and lifespan extension since dietary supplementation of methionine fully suppressed these phenotypes. Strikingly, treatment of wildtype (WT) worms with polyamine precursors mimicked *pycr-1* mutant resistance to G418 toxicity. Thus, tuning of the proline-polyamine-SAM axis is the metabolic mechanism of *pycr-1* mutant longevity.

SAM is required for ribosomal RNA (rRNA) maturation and thus essential for ribosome biogenesis (ribogenesis). I detected altered rRNA levels, and a selective reduction in translation of messenger RNAs involved in ribogenesis, including ribosomal proteins. Ribosomal stress activates heat shock transcription factor HSF-1, and a transcriptome analysis of *pycr-1* mutants revealed significant HSF-1 target gene expression. Consistently, *pycr-1* longevity and G418 resistance was *hsf-1* dependent, directly linking the metabolic state of *pycr-1* mutants to their stress resilience. Strikingly, transcriptional changes of *pycr-1(wrm22)* mutants strongly associate with the presence of histone modifications in WT worms. This observation provides a plausible alternative mode-of-action by which low SAM modulates gene transcription and regulates HSF-1 target gene expression. Of note, long-lived fruit flies under methionine restriction (MR) and mice under dietary restriction (DR) also showed decreased SAM levels and upregulation of HSF-1 target genes, suggesting that this mechanism is conserved from worms and flies to mammals. Overall, my data demonstrate that low SAM induced by impaired *de novo* proline biosynthesis is a shared characteristic with polyamine supplementation regimes, as well as DR and MR. Intriguingly, all three have been shown to extend lifespan in various model organisms. Therefore, my data imply inhibition of PYCR-1 as potential therapeutic approach to prolong health- and lifespan in humans.

Abbreviations

6-phosphogluconic acid	6-PG
Ribosome complex	80S
Adenine	A
Adenosine diphosphate	ADP
AHCY-like 1/2	AHCYL1/2
Arginase	ARG
Adenosine triphosphate	ATP
Betaine homocysteine methyltransferase	BHMT
Cytosine	C
<i>Caenorhabditis elegans</i>	<i>C. elegans</i>
Cystathione beta-synthase	CBS
Cystathionase	CTH
<i>Drosophila melanogaster</i>	<i>D. melanogaster</i>
Decoding center	DC
Decarboxylated S-adenosylmethionine	dcSAM
Dietary restriction	DR
Erythrose 4-phosphate	E-4-P
<i>Escherichia coli</i>	<i>E. coli</i>
Eukaryotic initiation factor 2 α	eIF2 α
Eukaryotic translation factor 5A	eIF5A
Ethyl methanesulfonate	EMS
Endoplasmatic reticulum	ER
Fructose-6-phosphate	F-6-P
Guanine	G
Glyceraldehyde 3-phosphate	G-3-P
Glutamate-5-semialdehyde	G-5-S
Glucose-6-phosphate	G-6-P
Gamma-glutamyl phosphate reductase	γ -TIP
Geneticin	G418
Glutamate 5-kinase	G5K
General control non-derepressible 2	GCN-2
Heat shock factor 1	Hsf1
Heat-shock protein	HSP
Insulin/insulin-like growth factor signaling	IIS
Integrated stress response	ISR
<i>Mus musculus</i>	<i>M. musculus</i>
Methionine adenosyltransferase	MAT
Mega bases	Mb
Cystathione beta-synthase	metC/CYS4
Methionine restriction	MetR
Mitochondrial unfolded protein response	mitoUPR

Multiple myeloma	MM
Messenger RNA	mRNA
Methionine synthase	MS
Mammalian target of rapamycin	mTOR
Mammalian target of rapamycin complex 1	mTORC1
Methyl transferases	MTs
Nascent polypeptide-associated complex	NAC
Nicotinamide adenine dinucleotide phosphate	NADP+
Nicotinamide adenine dinucleotide phosphate hydrogen	NADPH
Ornithine amino transferase	OAT
Ornithine decarboxylase	ODC
Pyrroline-5-carboxylate	P-5-C
Phosphorylated mTOR	p-mTOR
Protein phosphatase 2A	PP2A
Proline	Pro
Proline dehydrogenase	PRODH
Permeability transition	PT
Peptidyltransferase center	PTC
Pyrroline-5-carboxylate reductase	PYCR
Pyrroline-5-carboxylate reductase-1	PYCR-1
Pyrroline-5-carboxylate reductase 1	PYCR1
Pyrroline-5-carboxylate reductase 3	PYCR3
Ribose 5-phosphate	R-5-P
Ribosome biogenesis	Ribogenesis
antisense ribosome silencing RNAs	risiRNA
RNA interference	RNAi
RNA sequencing	RNAseq
Reactive oxygen species	ROS
Ribosomal protein	RP
Ribosomal protein of the large ribosome subunit	RPL
Ribosomal protein of the small ribosome subunit	RPS
Ribosomal RNA	rRNA
Ribulose 5-phosphate	Ru-5-P
Dedoheptulose 7-phosphate	S-7-P
S-adenosyl-homocysteine	SAH
S-adenosylhomocysteine hydrolase	SAHH/AHCY
S-adenosylmethionine	SAM
S-adenosylmethionine synthase	SAMS
Small nucleolar RNA	snoRNA
Single nucleotide polymorphism	SNP
Thymine	T
Target of rapamycin complex 1	TORC1
Transfer RNA	tRNA

	Ubiquitin	Ub
	Unfolded protein response	UPR
	Endoplasmic reticulum unfolded protein response	UPR ^{ER}
	Wildtype	WT
	Xylulose 5-phosphate	X-5-P
	Mitochondrial membrane potential	$\Delta\psi_m$

1 Introduction

1.1 Ageing

1.1.1 Ageing demographics

Over the course of just a few centuries human life expectancy has dramatically increased, especially in countries with good health care. This staggering achievement is largely due to reduced child mortality, better nutrition and advanced medical practices. While the health and lifespan of humans has drastically improved, this has resulted in a historically new phenomenon: starkly aged populations. As reported in *World Population Prospects 2019* by the United Nations department of economic and social affairs, Japan currently holds the record with the most aged population with a median age of 48.4 in 2020, coming from 28.8 in 1970 and projected to increase to 54.7 in 2050. In general, high-income countries see a similar trend: from 29.3 in 1970 to 41.0 in 2020, and projected to increase to 46.0 in 2050. An aged population has a big impact on the disposable income of its working population. The potential support ratio (25-64 year-olds compared to 65+ year-olds) will drop and increasingly stress disposable income (Figure 1). In 2019, the potential support ratio in Japan was just 1.8 and for high-income countries this averages at 3.0. This is expected to significantly drop in the coming decades¹. While more people reaching pensioning age is a great accomplishment of the developed world, this does present a historically new challenge to facilitate support and healthcare for this increasingly large group.

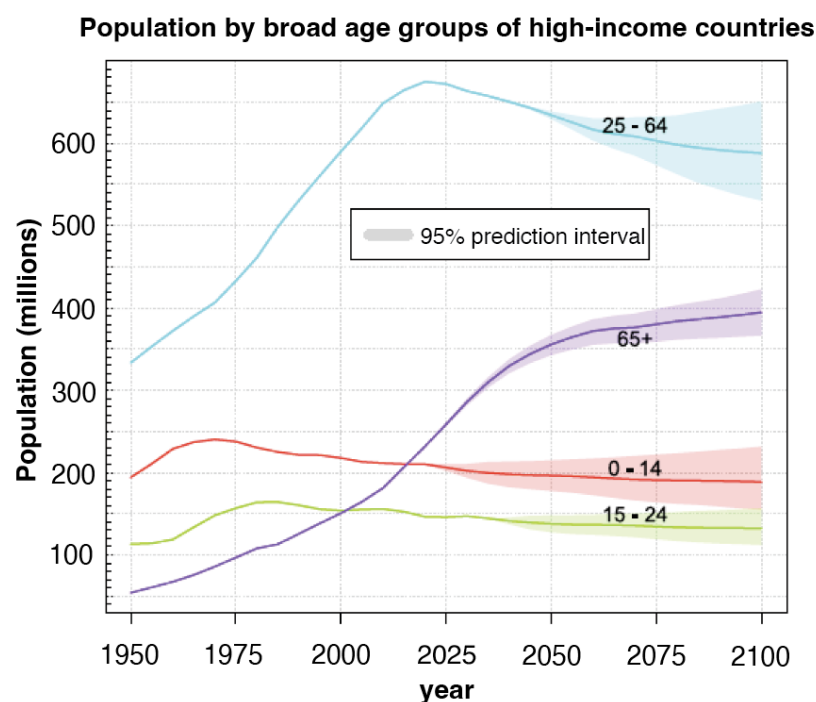


Figure 1: Demographic profile projections of high-income countries. Age distribution projections of population groups of high-income countries are projected until the year 2100. The four age groups are: 0-14 years old (red), 15-24 years old (green), 25-64 years old (blue), and 65 and older (purple). Taken from United Nations Department of Economic and Social Affairs, *Population Division World Population Prospects 2019*¹.

1.1.2 Anti-ageing research funding

Good healthcare for the elderly is a pillar of modern societies, however, with ageing demographics, governments seek solutions to mitigate the financial burden. In the hope to limit compounding expenses of elderly healthcare, governments are increasing their budgets for research on anti-ageing therapies, with a focus on effective (preventative) treatments to combat age-related diseases. The commercial sector wants to tap into this growing market and is attracting billions of dollars in funding. The 2022 startup Altos Labs, which aims to transform medicine through cellular rejuvenation, launched with a 3-billion-dollar budget, making it the largest biotech start-up to date and gaining instant unicorn status. It is important to note that generally the goal of anti-ageing research is not to prolong lifespan, but to improve health at advanced age. Consequentially, improvements to healthcare are likely to increase life expectancy. Although some researchers argue a fundamental or absolute limit of human lifespan of about 120 to 150 years as the culmination of complete loss of resilience², the resourcefulness of humans should not be underestimated. In recent years, discoveries on the biology of ageing have made their entrance on the public market with anti-ageing treatments that promise to slow down or reverse aspects of biological ageing, for example hormone replacement therapy³, nutritional regimes such as intermittent fasting⁴, or repurposing of drugs such as the anti-diabetic drug metformin⁵, to name a few. Since unravelling the determinants of ageing and the development of tools to prevent and reverse the ageing process has only just begun, it has the potential to significantly alter future demographics. Although there might be unforeseen bottlenecks that limit human lifespan, I like to be hopeful that we might be at the start of a run-off of increasingly effective interventions that promote healthy ageing and rejuvenate our bodies. The richness of life makes this pursuit worthwhile.

1.1.3 Life and characteristics of ageing

While there is no consensus regarding the definition of life, it is generally accepted that living organisms must have the capacity to grow and reproduce, have functional activity such as a metabolism and responses to stimuli, and be able to evolve⁶. The ageing process is the time-dependent change of these capacities, and although some organisms cheat by impressive feats of regeneration or cloning⁷, this normally leads to death. Ageing is well characterized by phenotypical signs such as frailty, loss of eye-sight and memory⁸. To understand the underlying mechanisms researchers have uncovered nine hallmarks of ageing, including genomic instability, telomere attrition, epigenetic alterations, loss of proteostasis, deregulated nutrient sensing, mitochondrial dysfunction, cellular senescence, stem cell exhaustion, and altered

intercellular communication (Figure 2)⁹. These essential cellular processes are functionally interconnected and this complicates research that tries to uncover the underlying mechanism of health and longevity-promoting interventions.

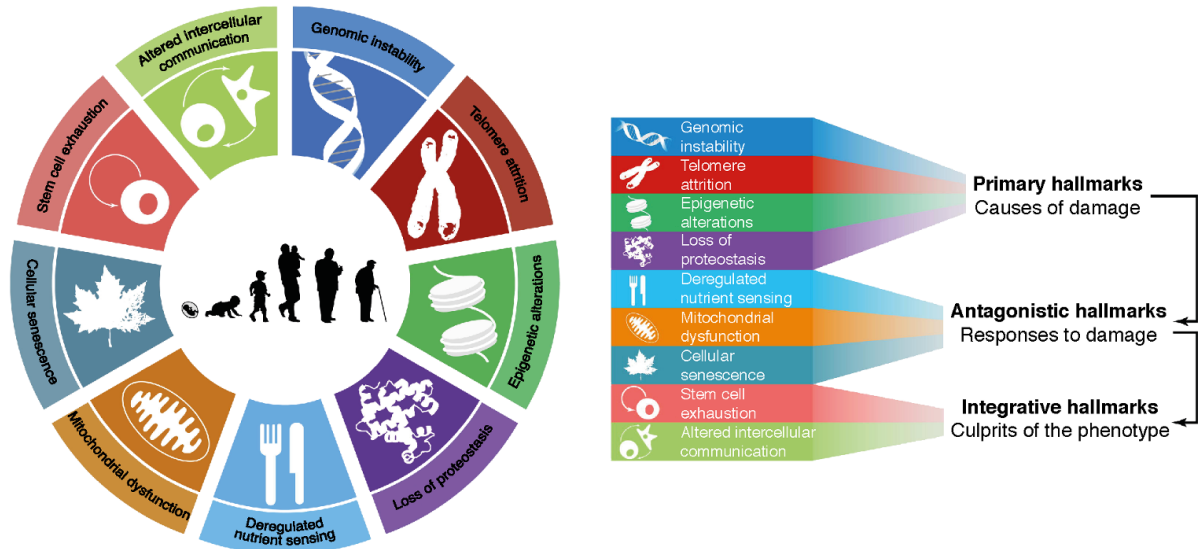


Figure 2: Functional interconnections between the hallmarks of ageing. The proposed nine hallmarks of ageing are grouped into three categories (right). (top right) Those hallmarks considered to be the primary causes of cellular damage. (middle right) Those considered to be part of compensatory or antagonistic responses to the damage. These responses initially mitigate the damage, but eventually, if chronic or exacerbated, they become deleterious themselves. (bottom right) Integrative hallmarks that are the end result of the previous two groups of hallmarks and are ultimately responsible for the functional decline associated with ageing. Adapted from López-Otín et al., *Cell* 2013⁹ by Kira Almeroth.

1.1.4 Theories of ageing

Organisms have wildly varying lifespans - interspecies as well as intraspecies. For example, a pygmy goby, as small fish, lives on average 58 days, while a Greenland shark can live over 250 years^{10,11}. While genetics are likely to play a large role in the potential lifespan of a species, a genetically homogenous species like humans can have drastically different lifespans. Environmental factors, nutritional intake and exposure to toxins are only some of the known modulators. It is important to separate two aspects of this discourse. On the one hand is the question why a species has the average lifespan that it has. On the other hand, is the question why within the species the lifespan varies between individuals. To current knowledge there is no sole determinant for an organism's lifespan. An organism's health depends on a multitude of biological networks of genetics, proteins and molecules that are interlinked: toxins can interfere with protein function, which can lead to DNA damage, and *vice versa*, DNA damage can lead to the malfunctioning of proteins and thereby lead to a toxic build-up of molecules and aggregates.

A renowned theory of ageing is the 'Damage Accumulation Theory of Ageing' that postulates that over the course of a lifetime damage accumulates, which increases the risk of fatal injury¹². A key characteristic of cancer is the derangement of its chromosomes, which is thought to be triggered upon DNA damage¹³. Similarly, the accumulation of toxic plaques, consisting of misfolded proteins, are a key characteristic of neurological diseases such as Alzheimer's disease¹⁴. Curiously, some age-associated diseases that occur in humans, do not naturally occur in genetically similar organisms: Alzheimer's disease does not occur naturally in mice, while naked and blind mole rats are not susceptible to cancer¹⁵. It is likely that evolutionary adaptations lead to varying susceptibility of potential age-related diseases. Evolutionary pressure can stress or relax resistance to life-threatening agents, depending on the requirements that the environment sets for the organism to successfully procreate. This additionally helps explain why certain genes that are important early in life remain active later in life, even when this is detrimental¹⁶. This is consistent with the 'Disposable Soma Theory of Ageing', which postulates that resources are finite and there is an evolutionary drive for reproduction, at the expense of damage regulation in somatic cells¹⁷.

The 'Antagonist Pleiotropy Theory of Ageing' suggests that organisms are genetically wired to live to a certain age¹⁸. Indeed, organisms can be genetically engineered to live longer and more resilient lives. In rare cases a single nucleotide polymorphism (SNP) can drastically increase an organism's lifespan, as is the case for the *Caenorhabditis elegans* (*C. elegans*) *age-1(mg44)* mutant that lives 9.6 times as long as wildtype worms¹⁹. To varying degrees, increased longevity can be accompanied by increased resilience to certain stresses, such as heat stress, but as well trade-offs to, for example, reduced fertility. Stress relaxation can be achieved by reducing protein synthesis, which reduces protein misfolding by improving translation fidelity and by increasing chaperone availability²⁰. In the case of *age-1(mg44)* mutant worms the trade-off to their extreme longevity is drastic: they are sterile^{19,21}. In other cases, trade-offs to increased longevity can be mild or non-apparent to researchers. However, for simple genetic alterations, such as SNPs, that lead to increased longevity under laboratory conditions, it is likely that they are detrimental to the success of the organism in the wild, as it is highly likely that the wildtype strain would have evolved accordingly. I conclude that the longevity of organisms is impacted by both intrinsic and extrinsic determinants, with a magnitude that is shaped by adaptive evolution for optimal success of the organism to succeed in its environment. In other words, the longevity of an organism adapts as a consequence of its evolution to best

fit its niche. In a world where our environment is shaped by ourselves, we should also be the masters of our longevity.

1.2 Model organisms for studying the ageing process

In this thesis I present data that was obtained from mouse, fly and worm experiments. Each of these model organisms has distinct advantages and disadvantages for ageing research, which I will highlight in the following section. The experiments with mice and flies were done in collaboration at the Max Planck Institute for Biology of Ageing (MPIage) with the laboratory of Linda Partridge. All worm work was done by me or in collaboration with my direct colleagues in the laboratory of Martin Denzel.

1.2.1 The roundworm *Caenorhabditis elegans*

The roundworm *C. elegans* is a perfect genetic tool to interrogate the genome using genetic mutagenesis and investigate its effects on lifespan. This easy to maintain and small worm species has a short median lifespan of 3 weeks. It generates about 300 larval offspring that are genetically identical, as the worm is generally kept as hermaphrodites that are able to self-reproduce. When genetic crosses are required, it is straightforward to generate males by subjecting hermaphrodites to an acute stress such as heat shock. The genome of this metazoan (100 mega bases (Mb)) is about half the size of the human genome (234 Mb), and its genes are generally well conserved. Key regulatory genes in *C. elegans* often have homologues in humans and kept a similar function throughout evolution. The reduced complexity of *C. elegans*' genetics makes it highly suitable for primary genetic research. Additionally, *C. elegans*' anatomy is transparent and invariant. The complete cell lineage of all of its 959 somatic cells is available. *C. elegans* is easy to maintain at ambient conditions and grown on agar plates spread with a monoculture of *Escherichia coli* (*E. coli*), which is their food source under laboratory conditions. *E. coli* libraries are available that over-express double stranded RNAs that serve to inhibit the expression of *C. elegans* genes by RNA interference (RNAi), when consumed²². The large and open research community facilitates easy access to public data sets, research tools and mutant strains. For these reasons, I use this model organism to generate mutants by ethyl-methane-sulfonate (EMS) mutagenesis that are resistant to a wildtype (WT) lethal level of the aminoglycoside antibiotic G418, which I use as a novel proxy to select for long-lived mutants.

1.2.2 The fruit fly *Drosophila melanogaster*

While roundworms are simple organisms with a limited diversity of tissues, fruit fly physiology is more complex with features akin to humans, including eyes, blood vessels and a heart. These organs show similar declines with age as those found in humans. Moreover, the wiring of the biological and biochemical processes is well conserved. With a maximum lifespan of about a hundred days, fruit flies live about three times as long as roundworms, but with their higher complexity they are a highly useful model organism to help learn more about human ageing processes. Collaboration with the Partridge department allowed me to test for conservation of newly found discoveries I made in the roundworm with existing and new fly data sets with relative speed, in a more complex ageing model.

1.2.3 The mouse *Mus musculus*

Compared to roundworms and fruit flies, mice are more closely related to humans and, therefore, important for validation of discoveries made in simpler model organisms before advancing to human trials. Due to their longevity of over 800 days, expensive maintenance and social complexity, mice are, however, generally not a good model organism for large scale experiments or screening purposes. Of note, the degree of conservation between the genomes of these model organisms is very high. Data-mining of existing mouse data sets previously acquired by the Partridge department at the MPIage allowed me to verify that the discoveries I did in the roundworm are likely conserved in vertebrates.

1.3 Protein homeostasis

The biosynthesis of proteins and metabolites that is required for an organism to grow is an energy intensive process that requires stringent regulation to conserve energy levels for other vital cellular and bodily functions. On a cellular level this includes, among others, the removal of toxins, clearance of accumulated proteins and the repair of DNA damage. These activities are carried out by specialized proteins that rely on protein homeostasis to function optimally. Protein homeostasis is, among others, regulated by protein synthesis and folding, which I will describe in more detail in this section.

1.3.1 Protein homeostasis declines with ageing

Protein synthesis is highly active during the developmental and reproductive phase of an organism. Over its lifetime the accumulation of DNA damage²³, toxic protein aggregates and the accumulation of toxic metabolites increasingly impair vital biological processes of the cell, leading to a reduced efficiency. Overall, all aspects of protein homeostasis change with age. Proteome integrity of the proteostasis network is safe-guarded by macromolecular complexes that collaborate to promote healthy ageing²⁴. Ageing is a multifaceted and interconnected process, where deterioration of one process negatively affects other processes. For example, accumulated erroneous proteins aggregate with other proteins, deterring them from functioning²⁵.

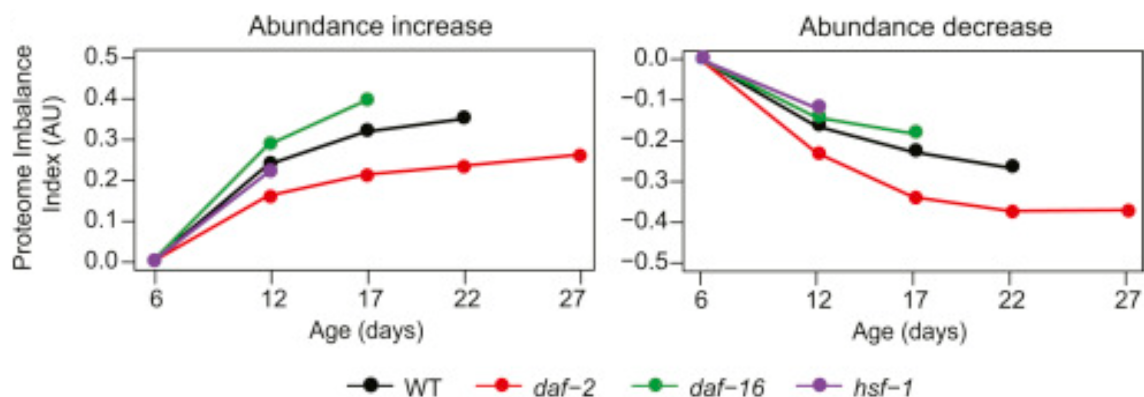


Figure 3: Proteome changes in WT and IIS mutant worms. Proteome imbalance in WT, *daf-2*, *daf-16* and *hsf-1* mutant animals expressed as proteome imbalance index. Abundance differences of proteins that increased (left) or decreased (right) during ageing relative to day 6 were summed up for each strain and normalized to the number of quantified proteins. The total number of quantified proteins was similar in the different worm strains and ranged from 3743 to 4700 proteins. Taken from Walther et al. *Cell* 2015²⁵.

As protein homeostasis deteriorates with age, protein synthesis is slowed down due to the diminished capacity for efficient protein synthesis and damage removal. Damage accumulation is reduced when protein synthesis is slowed down^{26,27}. Indeed, impairment of protein synthesis

by intervention such as dietary restriction or mutation can promote healthy ageing and extend lifespan of model organisms^{20,26,28}, as well as humans²⁹. The downregulation of translation is an evolutionary conserved response to reduced insulin/insulin-like growth factor signaling (IIS)³⁰. As expected, long-lived insulin receptor *daf-2* mutants, which are characterized by reduced translation and protein turnover³¹, better balance their proteome over time than WT worms, while short-lived transcription factor mutants *daf-16* or *hsf-1* do worse (Figure 3)²⁵. Thus, a thorough understanding of protein synthesis is key to a better understanding of resilience and longevity.

1.3.2 Protein synthesis

Ribosomes are large and highly abundant ribonucleoprotein complexes that are responsible for the biosynthesis of proteins. Translation of the genetic code into functional proteins happens by interpreting messenger RNAs (mRNAs) at a trade-off between speed and fidelity. The ribosome decodes the message into a string of amino acids, a polypeptide chain (Figure 4). Amino acids are shuttled to the ribosome by transfer RNAs (tRNAs), which dock to the A-site (acceptor) upon binding with eukaryotic elongation factor eEF1A in a GTP-dependent manner. After codon recognition by the tRNA, the aminoacyl-tRNA forms a peptide-bond with the growing polypeptide chain on the peptidyl-tRNA located in the P-site and the nascent peptide is transferred to the aminoacyl-tRNA. The P-site is the peptidyl transferase center that forms a cavity that allows for the catalysis of the peptide bond formation. It consists primarily of conserved ribosomal RNA (rRNA) of the large ribosomal subunit. Translocation to the E-site (exit) requires the eukaryotic elongation factor eEF2. Hydrolysis of GTP accommodates this step. The deacetylated tRNA occupies the E-site and the peptidyl-tRNA is in the P-site. The A-site is now vacant and available for the next aminoacyl-tRNA in complex with eEF1A³².

During its passage through the exit tunnel of the ribosome, the polypeptide chain forms the first alpha-helices. Specialized proteins, called chaperones, help guide the newly synthesized polypeptide nascent of the exit tunnel through a complex folding energy landscape to ultimately complete its secondary structure. This co-translational protein folding process is intrinsically error-prone and requires the constant surveillance for misfolding. I will describe chaperone-mediated protein folding in more detail in section 1.3.4.

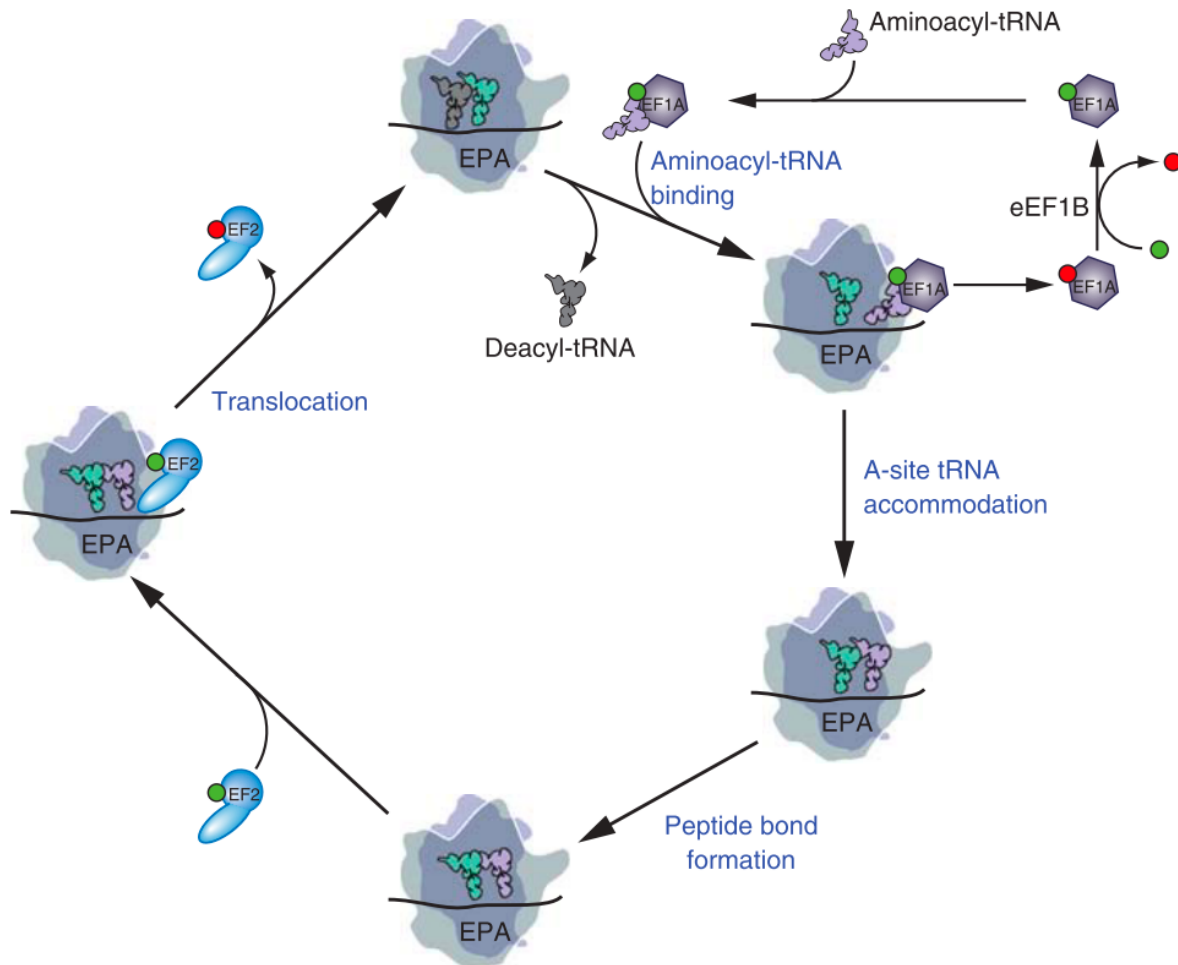


Figure 4: Model of the eukaryotic translation elongation pathway. In this model the large ribosomal subunit is drawn transparent to visualize tRNAs, factors, and mRNA binding to the decoding center at the interface between the large and small subunits and tRNAs interacting with the peptidyl transferase center in the large subunit. Starting at the top, an eEF1A.GTP.aminoacyl-tRNA ternary complex binds the aminoacyl-tRNA to the 80S ribosome with the anticodon loop of the tRNA in contact with the mRNA in the A-site of the small subunit. Following release of eEF1A.GDP, the aminoacyl-tRNA is accommodated into the A-site, and the eEF1A.GDP is recycled to eEF1A.GTP by the exchange factor eEF1B. Peptide bond formation is accompanied by transition of the A- and P-site tRNAs into hybrid states with the acceptor ends of the tRNAs moving to the P- and E-sites, respectively. Binding of eEF2.GTP promotes translocation of the tRNAs into the canonical P- and E-sites, and is followed by release of eEF2.GDP, which unlike eEF1A does not require an exchange factor. The ribosome is now ready for the next cycle of elongation with release of the deacylated tRNA from the E-site and binding of the appropriate eEF1A.GTP.aminoacyl-tRNA to the A-site. Throughout, GTP is depicted as a green ball and GDP as a red ball; also, the positions of the mRNA, tRNAs, and factors are drawn for clarity and are not meant to specify their exact places on the ribosome. Taken from T.E. Dever and R. Green, *Cold Spring Harbor Perspectives in Biology* 2012³².

1.3.3 Protein synthesis efficiency and fidelity

Protein synthesis is inherently error-prone. In fact, mRNA decoding errors occur with an estimated frequency of 10^{-4} in a mostly stochastic manner. Translation fidelity is orders of magnitude less accurate than DNA replication or transcription, and thus represents the limiting factor in the accuracy of gene expression³³. Protein synthesis is the result of a multistep mechanism consisting of initiation, elongation and termination stages as described above.

Recognition of the correct sense codon by a tRNA relies on the energy state of the interaction, where a cognate codon:anticodon match results in a low energy state. This allows for the relative slow interaction with eIF1A to bind to the A-site. A non-cognate codon:anticodon interaction results in a high energy state, which generally results in the non-cognate aminoacyl-tRNA to leave to A-site before it interacts with eIF1A to bind to the A-site³⁴. Importantly, binding at the A-site requires hydrolysis of GTP. This proofreading mechanism represents one of several mechanisms that promote translational fidelity^{35,36}.

Aminoglycosides are ribosome inhibitors that target all stages of translation and have the propensity to induce miscoding errors by binding to the decoding center³⁷. They promote accommodation of near-cognate aminoacyl-tRNAs to bind to the A-site, resulting in misincorporation of amino acids into the polypeptide chain and generation of aberrant proteins³⁸. While protein synthesis inhibition can promote healthy ageing^{26,39}, it is likely that toxicity of the aminoglycoside geneticin (G418), used in this thesis, stems from the generation of aberrant proteins. This may lead to protein homeostasis collapse. Reduced protein synthesis can be compensated for by increased protein stability and recovery of protein synthesis by stress signaling to enhance biogenesis⁴⁰. In this thesis I screened mutagenized worms for resistance to a WT lethal concentration of G418.

1.3.4 Chaperones are key to maintain protein homeostasis

Chaperones assist with the proper folding of proteins at the nascent polypeptide chain of the translating ribosome, but also assist with refolding of proteins that have become misfolded (Figure 5). Endogenous and external stressors can impair the folding process, strain protein homeostasis and promote ageing⁴¹. A well-studied family of chaperones are heat shock proteins under the control of transcription factor heat shock factor 1 (Hsf1), which are upregulated for example upon heat stress⁴² or endoplasmic reticulum (ER) stress by the antibiotic tunicamycin⁴³. Heat stress triggers global pausing of translation elongation and affects the stability of proteins, causing them to unfold⁴⁴. Tunicamycin on the other hand, inhibits N-linked glycosylation, which is required for folding of newly synthesized proteins in the ER⁴⁵. Perturbations that lead to stalling of the polypeptide chain, such as non-stop proteins, are sensed by a ribosome-bound complex termed the ribosome quality control complex (RQC). RQC signals a distinct translation stress signal that is mediated by Hsf1 that results in the ubiquitination and subsequent proteasomal degradation of the stalled ribosome⁴⁶. Additionally, a nascent polypeptide-associated complex (NAC) associates with ribosomes to promote translation and protein folding. Upon disbalances of protein homeostasis, NAC dissociates to

protein aggregates where it functions as a chaperone. This results in a negative feed-back mechanism that leads to the functional depletion of NAC from the ribosome and reduced mRNA translation. Importantly, increased NAC dissociation is observed during ageing, in response to the synthesis of aggregation-prone proteins and upon heat stress⁴⁷.

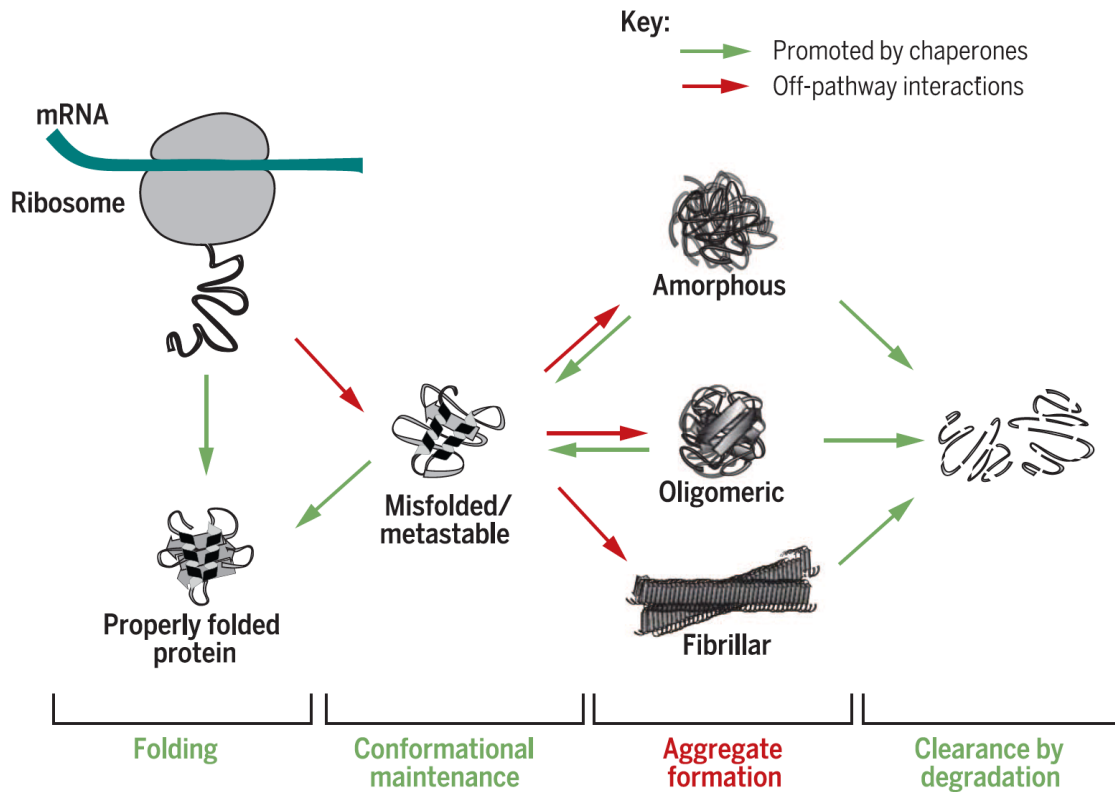


Figure 5: Molecular chaperones are key players in the cellular protein homeostasis network and serve to maintain a balanced proteome. They promote the folding of newly synthesized proteins, function in conformational maintenance, and prevent potentially toxic off-pathway aggregation. Chaperones also cooperate with other components of the proteostasis network, such as the proteasome system and autophagy, in the removal of terminally misfolded and aggregated proteins through proteolytic degradation. Taken from Balchin et al., *Science* 2016⁴¹.

In conclusion, Hsf1 monitors a broad range of stressors to help maintain protein homeostasis by regulating chaperone gene transcription⁴⁸. In the absence of chaperones, aggregation of misfolded proteins becomes toxic and shortens lifespan⁴⁹. Thus, by ensuring proper folding of proteins, chaperones play an important role in protein homeostasis. Their protective effects can be harnessed to combat protein aggregation and promote healthy ageing and extend lifespan⁵⁰.

1.4 Ribosome homeostasis

Organismal development and protein turnover put a high demand on *de novo* protein biosynthesis, and thus large numbers of ribosomes are required. In fact, a mammalian cell harbors up to 10 million ribosomes and devotes up to 60% of its energy on ribosome biogenesis (ribogenesis). This easily makes it the most energy-demanding process in the cell, and thus requires tight regulation and coordination of rRNAs and ribosomal proteins (RPs)⁵¹.

1.4.1 Ribosome biogenesis

Ribosomes are ribonucleoprotein complexes comprising of rRNA and up to 79 different RPs⁵². rRNAs are the most abundant and universal non-coding RNAs. The small ribosomal subunit (40S) consists of 18S rRNA and 33 RPs, whereas the large ribosomal subunit (60S) consists of 5S, 5.8S and 25S/28S rRNAs, and 46 RPs (Figure 6). Together, 40S and 60S form the fully assembled ribosome complex (80S)⁵²⁻⁵⁴.

A complex sequence of processing steps is required to gradually release mature RNAs from its long polycistronic pre-ribosomal RNA precursor (Figure 6). The maturation of pre-rRNAs and their assembly with RPs takes place in a specialized organelle in the nucleus called the nucleolus^{52,53}. There, hundreds of trans-acting assembly factors chaperone maturation of the pre-rRNA with high fidelity in tight coordination with an RNA chaperone and RPs. The ribosome biogenesis factors engulf and direct subdomains of the pre-rRNA to distinct compartments. This allows for processing of domains that are not accessible in the mature subunit. Sequentially, conformational freedom is limited to facilitate flexible proteins to incorporate dynamic subcomplexes into the ribonucleoprotein complex, culminating in the 40S and 60S subunits⁵⁵.

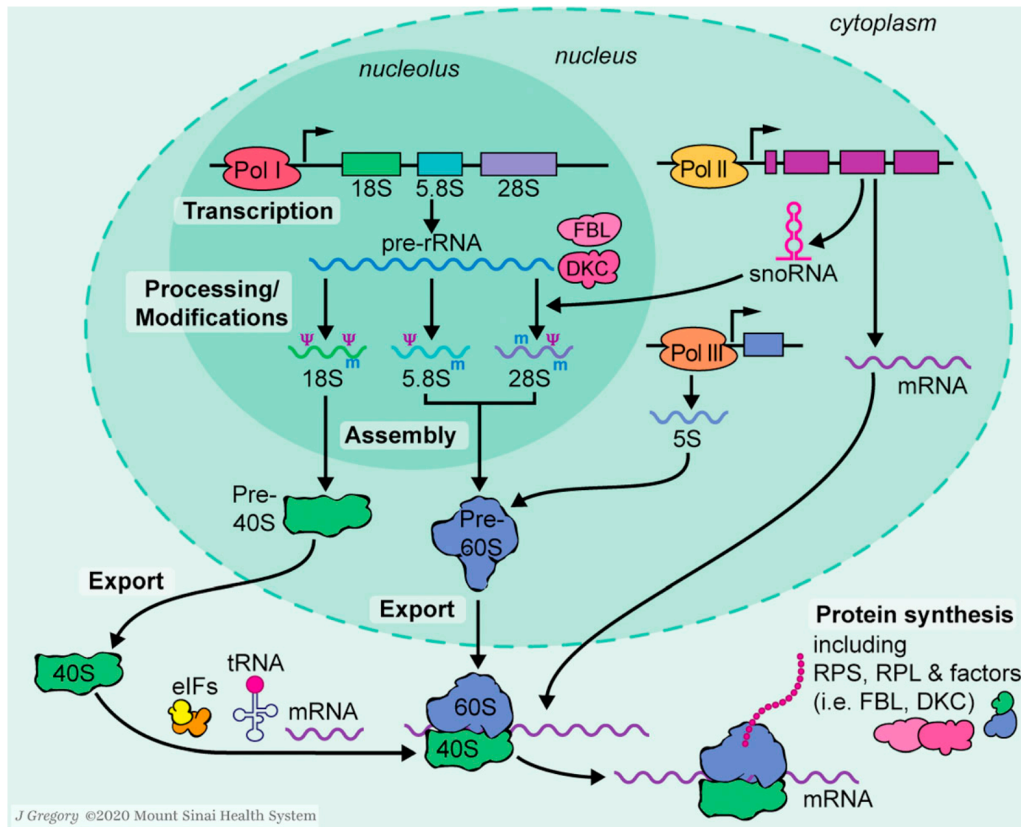


Figure 6: Schematic diagram of ribosome biogenesis. In the nucleolus, RNA Pol I transcribes a polycistronic pre-rRNA, which is subsequently processed and modified into mature rRNAs (18S, 5.8S, and 28S). Another rRNA, 5S, is transcribed by RNA Pol III in the nucleoplasm. RNA Pol II transcribes small nucleolar RNAs (snoRNAs) (which aid the maturation of pre-rRNA) and mRNAs in the nucleus. mRNAs are transported to the cytoplasm and then translated by ribosomes. RPs can be reimported to the nucleus to assemble pre40S/60S with rRNAs, which are then exported to the cytoplasm and matured to function in mRNA translation. Illustration by Jill K. Gregory from Mount Sinai Health System. Taken from Li and Wang, *Journal of Cell Biology* 2020⁵⁴.

1.4.2 Ribosome biogenesis (dys)regulation

The sheer complexity of ribogenesis allows for disruption of virtually any step, which can result in cell cycle arrest, senescence or apoptosis, primarily through the activation of the tumor suppressor protein p53. Additionally, disruption of ribogenesis is often associated with cancer and ageing-related degenerative diseases⁵¹. Moreover, alteration of any step of the assembly process may impact growth by perturbation of protein homeostasis⁵⁶.

Impaired rRNA processing results in downregulation of pre-rRNAs, triggered by a signaling cascade following the generation of antisense ribosomal silencing RNAs (risRNAs). These are products of degenerated misprocessed rRNAs and are sensed by the argonaute protein NRDE-3. Subsequently, through the nuclear RNAi-mediated silencing pathway, NRDE-3 translocates to the nucleus and downregulates pre-rRNA transcription. This adds an additional layer of

quality control to maintain ribosome homeostasis⁵⁷. Dysregulation of ribogenesis can lead to imbalances in the synthesis of RPs. Accumulation of newly synthesized RPs tend to rapidly form aggregates that compromise essential cellular processes. Cells respond by upregulating chaperones to help dissolve RP aggregation. Moreover, exogenously improved chaperone capacity protects from ribosome assembly insults from genetic, environmental and xenobiotic perturbations that generate orphan RPs⁵⁸. These examples highlight the different layers involved in safe-guarding ribosome homeostasis and promote healthy ageing.

1.4.3 Ribosome heterogeneity and mRNA translation specificity

The catalytic activity of the peptidyltransferase center (PTC) and the decoding center (DC) is mainly formed by an rRNA pocket of the large or small ribosomal subunit, respectively. rRNA maturation involves extensive modification of pre-rRNAs. rRNA modifications generally function to stabilize rRNA folding, but they also cluster at functionally active sites such as the PTC and DC. The rRNA nucleotide modifications include methylation and pseudouridylation. Loss of rRNA modifications of the DC impairs translation and strongly impairs pre-rRNA processing⁵⁹. Contributors to ribosome heterogeneity include rRNA variants and modifications, and the stoichiometry, composition, and presence of paralogues of ribosomal proteins. Not all modifications are constitutively present on all ribosomes⁵⁴.

Ribosome heterogeneity provides translational control that potentially allows cells to quickly alter translation of preferential mRNAs in response to stimuli that demand quick changes to protein abundances. A diverse landscape of rRNA modification patterns have been found in response to environmental changes, during development and in disease⁵⁹. Alternatively, RP activity might be highly regulated and provide a layer of translational control of mammalian development⁶⁰. Together, this suggests that ribosome heterogeneity contributes to translational control of gene expression and could play an important role in ageing.

Ribosome footprinting is a technique that identifies ribosome-protected mRNA fragments. It allows for comprehensive and quantitative measuring of translation by deep sequencing of ribosome-protected mRNA fragments (Figure 7). The identity of these fragments signifies the precise position of ribosomes. This technique depends on a pull-down step using a tagged ribosomal protein, and thus, by choosing which ribosomal protein to select for, can be used to enrich for ribosomes with alternative compositions and investigate translational control by ribosome heterogeneity.

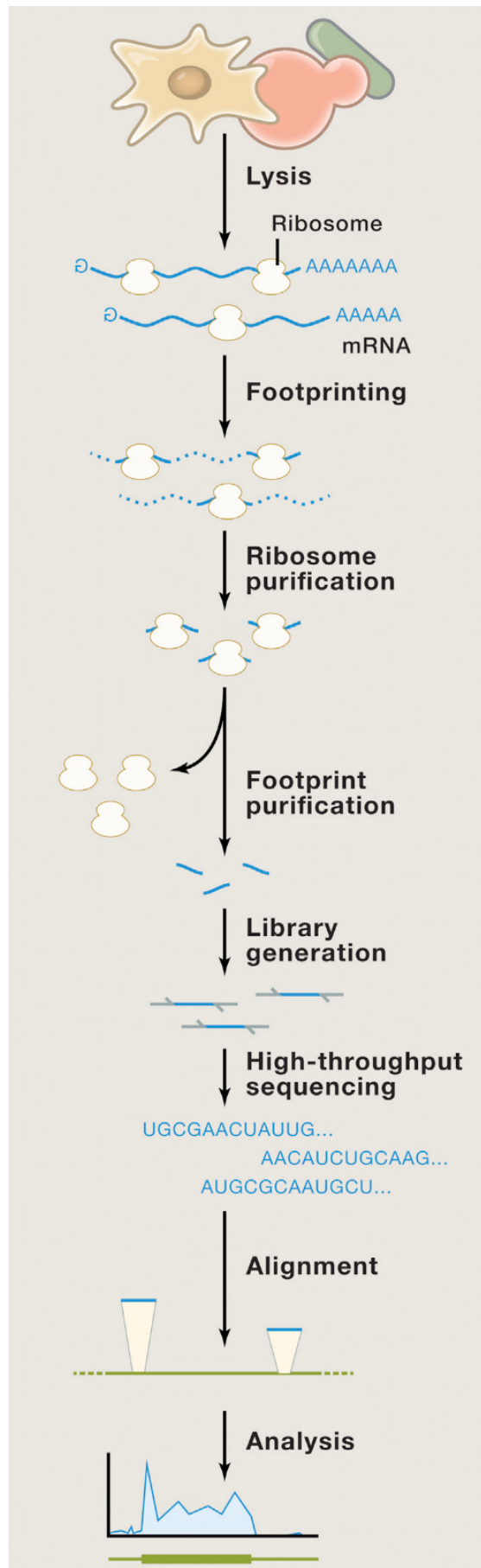


Figure 7: Schematic of ribosome footprint profiling of translation. The workflow for ribosome profiling in different cell types follows the same basic steps: isolation of mRNAs on polysomes, nuclease digestion of the mRNA sequences unprotected by bound ribosomes, and purification of the remaining mRNA fragments followed by library generation, deep sequencing, and computational analysis. Taken from Ingolia, *Cell* 2016⁶¹.

In general, ribosome footprinting allows for distinguishing between altered transcriptional or translational control upon changes in protein synthesis. Comparing abundance of actively translated mRNAs with total mRNA levels allows identification of mRNAs that are either under transcriptional or translational control⁶¹. This technique, performed by Dr. Maxime Derisbourg, proved useful in preparation of this thesis to help identify relevant and distinct transcriptional and translational programs.

1.5 Cellular metabolism

Catabolic and degradation processes break down fats, sugars, proteins, nucleotides and other molecules to provide the substrates for anabolic and biochemical processes that are important for the functioning of our cells. This process is called cellular metabolism. Indeed, these molecules are broken down to provide energy and basic building blocks in an efficient recycling process. While nutrition has a direct impact on our metabolism, environmental and genetic factors also play key roles to determine our metabolic state. Given the high energy demand of ribogenesis, it is optimally positioned as a sensor for imbalances in the metabolic state.

The metabolic state impacts the rates of both new ribosome assembly, as well as ribosome recycling⁶². Moreover, poor nutrition results in low levels of amino acids, which are the building blocks of protein synthesis. Therefore, ribosome biogenesis and activity are tightly regulated to ensure protein homeostasis and to conserve energy when nutrient availability is limited⁶³. Nutrient and energy sensing pathways that respond to limitations of key metabolites directly affect survival^{64,65}. Since *de novo* protein synthesis is required to maintain protein homeostasis and depends on adequate metabolite levels, stress signaling pathways are activated upon depletion of metabolites or low energy. These stress responses exist to limit energy expenditure by enhancing protein stabilization via chaperone overexpression and the breakdown of non-essential proteins via proteasomal degradation, amongst others. A mild exogenous activation of stress response pathways in non-stress conditions have been shown to be protective against perturbation of protein homeostasis and age-related disease, and thereby extend lifespan⁵⁰. Signaling of metabolite levels has been extensively studied and lead to new insights for dietary recommendations to promote healthy ageing⁶⁶. Nevertheless, the mechanisms involved in metabolite sensing and its effects on ribogenesis or activation of stress signaling pathways are not fully understood.

In this thesis I will elucidate the metabolic changes due to a point mutation in pyrrolyine-5-carboxylate reductase 1, a key enzyme in *de novo* proline biosynthesis. Therefore, I will discuss in detail amino acid metabolism with a focus on proline biosynthesis in detail. Additionally, due to their interaction with *de novo* proline biosynthesis, I will also discuss polyamine and one-carbon metabolism in detail below.

1.5.1 Amino acid homeostasis

mRNA translation culminates with the release of the polypeptide chain that was synthesized from amino acids delivered by tRNAs. Amino acids are recycled by protein turnover, but there is a net loss due to amino acid oxidation. Homeostasis is maintained through conversion of non-essential amino acids to essential amino acids, and the transfer of amino groups from oxidized amino acids to *de novo* amino acid biosynthesis. The breakdown of cellular proteins through autophagy and slowed protein synthesis is under the control of mammalian target of rapamycin complex 1 (mTORC1), which is inactivated upon amino acid depletion⁶⁷. Amino acid depletion might also activate the general control non-depressible 2 (GCN2)-ATF4 pathway⁶⁸. This results in the upregulation of the biosynthesis of non-essential amino acids, and the transcription of genes involved in amino acid transport⁶⁷. Amino acid homeostasis is furthermore regulated by active oxidation of excess amino acids, resulting in urea production. In short-term fasting conditions, blood plasma amino acid levels are generally not reduced, due to a coordinated response to downregulate protein synthesis and upregulate autophagy. Long-term malnutrition, however, activates a protein specific response by the central nervous system that triggers avoidance of nutrient-poor diets. Conversely, high protein diets that provide excess abundance of amino acids trigger satiety to reduce food intake⁶⁷.

1.5.2 Dietary restriction

Dietary restriction (DR), which constitutes long-term reduced food intake while avoiding malnutrition, promotes healthy ageing across species (Figure 8)^{20,69}. DR regimes attains its beneficial effects due to reduced oxidative stress, growth hormone and mTOR signaling, and improved insulin sensitivity, DNA repair and proteostasis⁷⁰⁻⁷². This reduces cellular senescence and inflammation, improves stem cell maintenance, mitochondrial function, and immune tolerance, and activates autophagy and tissue repair. The overall beneficial effects to organ function and stress resistance result in improved health and longevity. Studies have demonstrated that a reduction in specific nutrients in the diet, rather than overall caloric intake, are primarily responsible, and nutrient sensing is believed to play a key role. Accumulating evidence points to a positive effect of reduced essential, but not non-essential, amino acids in the diet. In particular, reduced dietary methionine induces specific protective molecular mechanisms⁶⁹. Recently, an inhibitor of activity of mTORC1, the evolutionary conserved protein Sestrin, was discovered as a sensor of amino acids *in vitro*. *Sestrin* null mutant flies were shown to have a blunted lifespan extension by DR⁶⁹. Nevertheless, the molecular mechanism by which DR exerts its beneficial effects remains elusive.

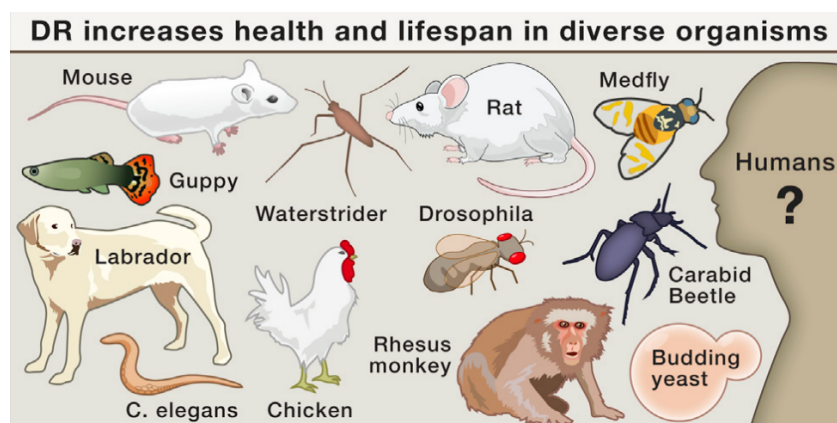


Figure 8: Dietary restriction increases healthy lifespan in diverse single-celled, invertebrate, and vertebrate animals. Taken from L. Fontana and L. Partridge, *Cell* 2015⁶⁶.

1.5.3 Methionine restriction

Metabolite levels reflect the cellular energy state and changing metabolite concentrations can trigger stress responses. Of all the dietary amino acids, methionine restriction (MetR) has been found to exert the strongest beneficial effects, mimicking DR. Indeed, like with DR, MetR extends lifespan across different species and improves resilience. Methionine feeds into complex metabolic pathways, including the methionine cycle, the trans-sulfuration pathway, the salvage cycle, and *de novo* polyamine biosynthesis pathway (Figure 9), for each of which manipulation can extend lifespan. The potential mechanism by which MetR exerts its beneficial effects to lifespan is by reducing S-adenosylmethionine (SAM) level. SAM is the universal methyl donor, and methylation regulates a wide variety of processes, including those regulated by MetR⁷³. Replenishing SAM requires either its recycling in the methionine salvage pathway or new synthesis from dietary methionine⁷³. The methionine salvage pathway is energy demanding and the essential amino acid methionine is generally limiting, which makes SAM levels sensitive to the metabolic state of the cell. Methionine restriction and SAM depletion have been implicated in longevity^{73–75} and their effect is associated with epigenetic changes⁷⁶ and reduced translation⁷⁷. The molecular mechanism by which low SAM extends lifespan is unknown, but it may act by reducing the rate of translation, modifying gene expression by reducing histone methylation, upregulation of autophagy, or improving mitochondrial function or antioxidant defense⁷³.

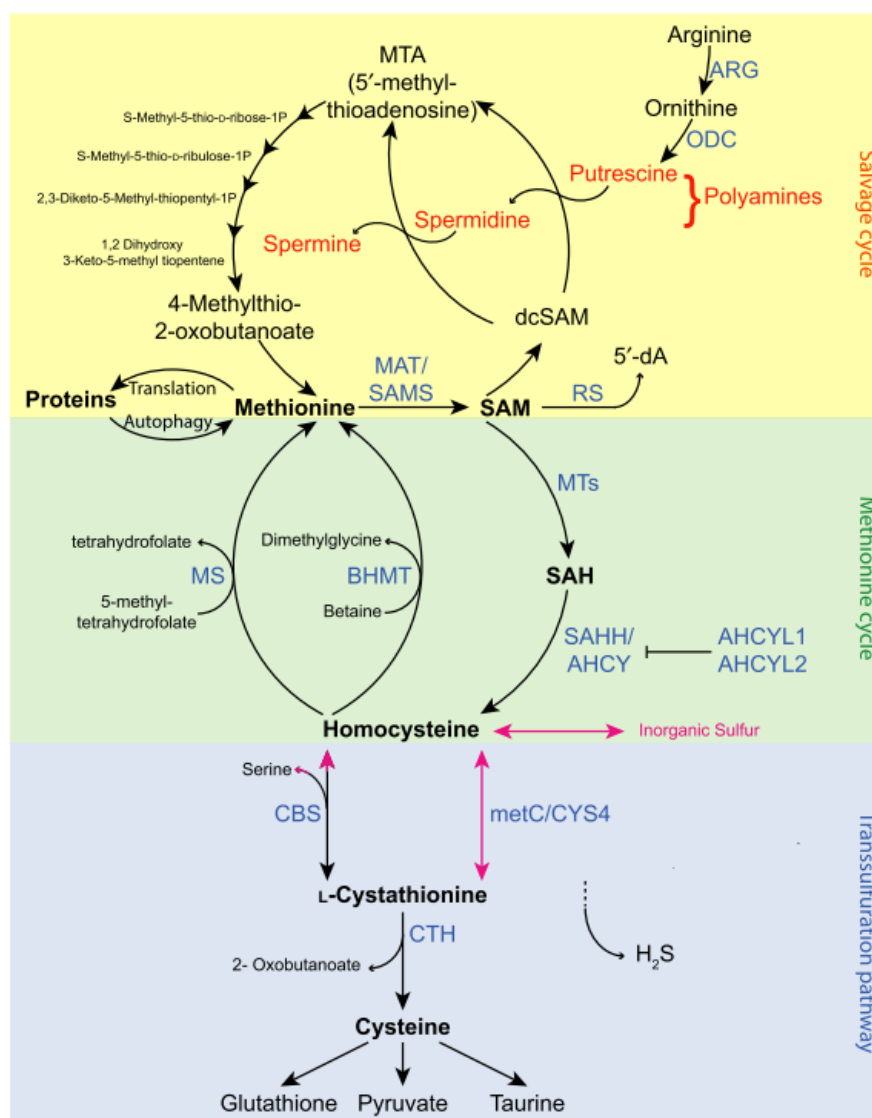


Figure 9: Schematic of methionine metabolism. ARG = arginase, ODC = ornithine decarboxylase, MAT = methionine adenosyltransferase, SAMS = S-adenosylmethionine synthase, MTs = methyl transferases, MS = methionine synthase, BHMT = betaine homocysteine methyltransferase, SAHH/AHCY = S-adenosylhomocysteine hydrolase, AHCYL1/2 = AHCY-like 1/2, CBS = cystathione beta-synthase, metC/CYS4 = cystathione beta-synthase, CTH = cystathionase. Taken from Parkhitko et al., *Aging Cell* 2019⁷³.

1.5.4 Polyamine metabolism

In addition to its role as a methyl donor, decarboxylated SAM is utilized as an aminopropyl donor in polyamine biosynthesis to synthesize spermidine and spermine^{78,79}, but whether polyamine biosynthesis affects SAM level remains elusive. Polyamines exhibit various functions in the cytoplasm, mitochondria and nucleus, and are involved in the regulation of cell proliferation and necrosis (Figure 10). They are polycations that interact with negatively charged molecules such as DNA and RNA. In effect they modulate histone acetylation by their interaction with DNA, and improve protein synthesis by interaction with ribosomes⁸⁰. Contrary to the general trade-off between translation rate and fidelity, polyamines improve overall

ribosome function and increase translation rate and fidelity⁷⁹. Of note, in *E. coli* over 500 polyamines stably associate to each single ribosome⁸¹.

Spermidine is a precursor for the essential post-translational modification of eukaryotic translation factor 5A (eIF5A) to form the amino acid hypusine from lysyl residues. The hypusine modification is critically required for protein synthesis. eIF5A promotes the formation of the first peptide bond, is especially important for poor substrates like proline, essential for translation of polyproline tracts and required for translation termination⁷⁹.

Polyamine abundance declines with ageing. Conversely, high polyamine diets extend lifespan in model organisms⁸². However, they have also been found to be increased in cancer cells⁸⁰. In general, polyamine levels are tightly regulated, but modulating their levels has the potential to improve healthy ageing.

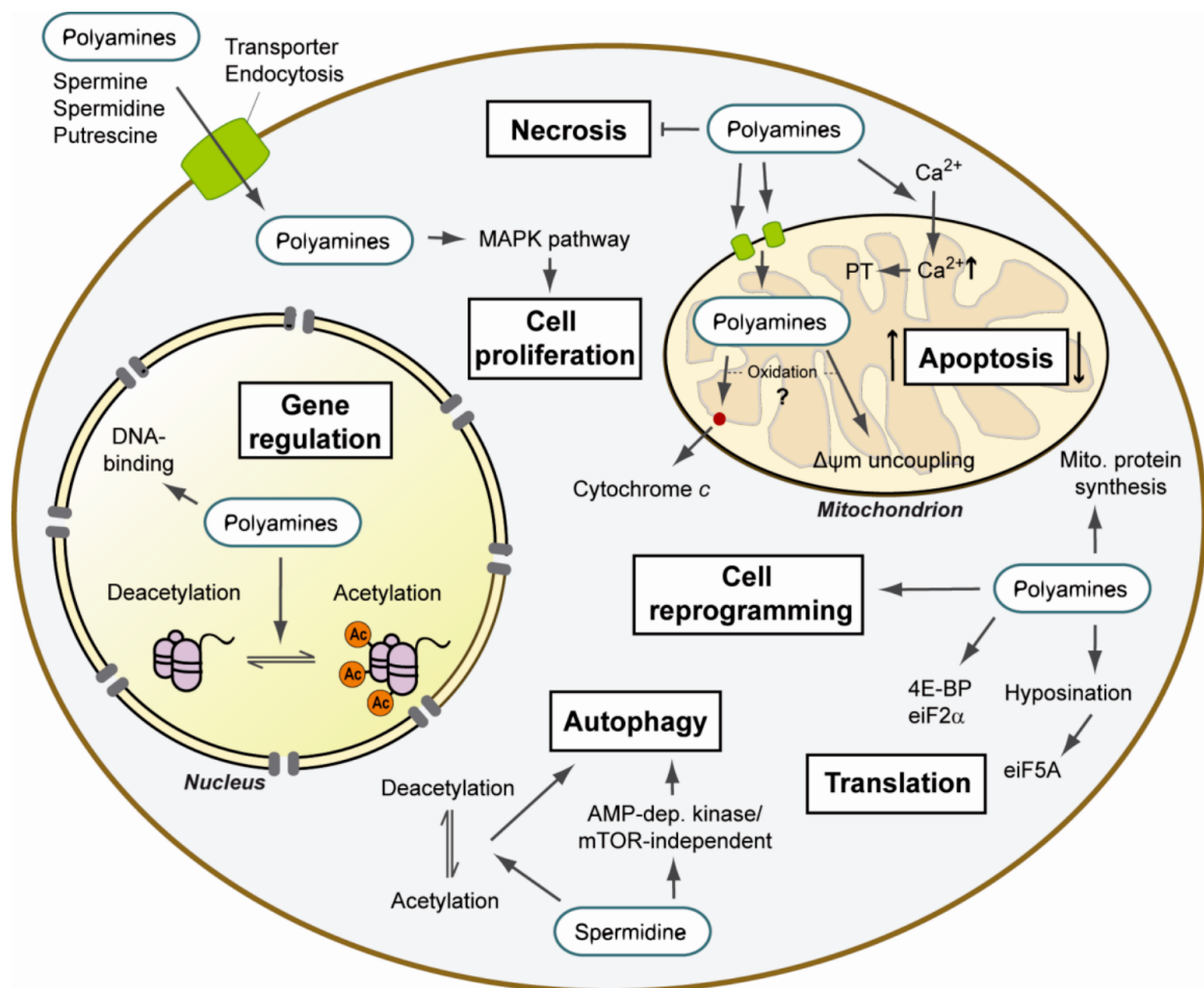


Figure 10: Summary of the cellular mechanisms of action of polyamines. Upon entering the cell, polyamines exhibit various functions in the cytoplasm, nucleus and mitochondria. Polyamines are involved in the regulation of cell death and cell proliferation as well as in protein synthesis at the level of both gene expression and translation. Recent evidence also assigned polyamines functions in cell reprogramming and autophagy regulation. Thus, polyamines are involved in a broad array of processes and cellular responses that suggest a complex and important role in the control of cellular life and death. PT: permeability transition; $\Delta\psi_m$: mitochondrial membrane potential. Taken from Minois et al., *Aging* 2011⁸⁰.

1.5.5 Proline metabolism

It is generally believed that polyamines are synthesized from arginine. However, the polyamine biosynthesis pathway utilizes glutamate 5-semialdehyde (G-5-S), an intermediate it shares with *de novo* proline biosynthesis pathway⁷⁸. Recently, studies in chickens and suckling pigs have shown that proline, not arginine, is the primary substrate for polyamine biosynthesis^{78,83}.

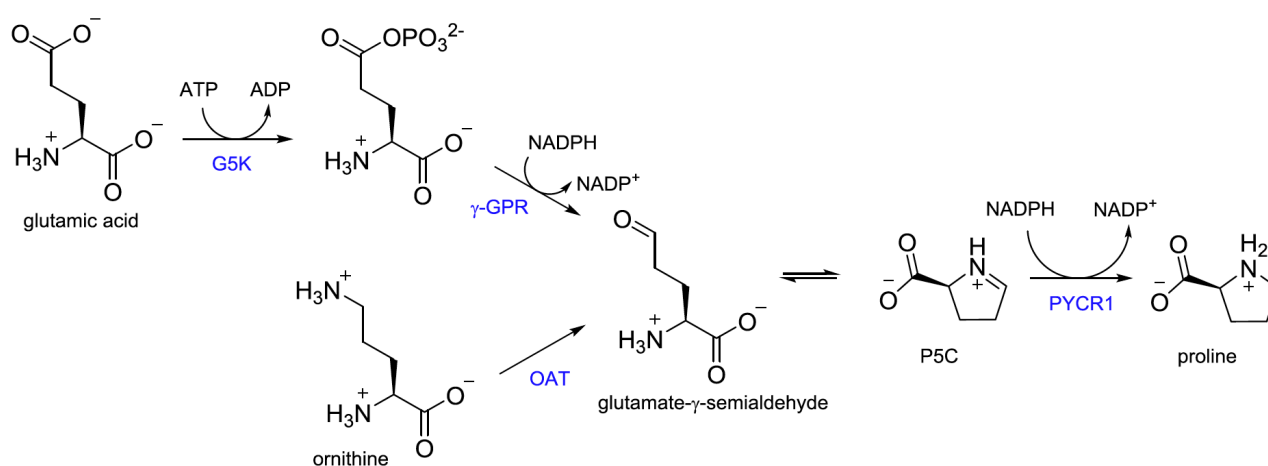


Figure 11: The proline biosynthesis pathway. G5K = glutamate 5-kinase, γ -GPR = gamma-glutamyl phosphate reductase, OAT = ornithine amino transferase, PYCR1 = pyrroline-5-carboxylate reductase 1. Taken from Milne et al., *Bioorganic and Medicinal Chemistry Letters* 2019⁸⁴.

Proline is a non-essential amino acid that can be synthesized from glutamic acid or ornithine by pyrroline-5-carboxylate reductases (PYCRs) (Figure 11). Proline and its derivative hydroxy-proline are the main residues found in collagen, which is the most abundant protein within the body⁸⁴. It is the only proteogenic amino acid that is also an imidic acid, as it contains both an imine ($>C=NH$) and carboxyl ($-C(=O)-OH$) group.

Collagen acts as a proline sink, which can be catalyzed by proline dehydrogenase (PRODH). PRODH is activated by p53 under genotoxic stress, to generate reactive oxygen species (ROS) for programmed cell death. Alternatively, it is upregulated by nutrient stress through the mTOR pathway to generate adenosine triphosphate (ATP) for survival⁸⁵. Together with PYCR, PRODH forms a metabolic relationship known as the proline cycle (Figure 12), which has been implicated in ATP production, protein and nucleotide synthesis, anaplerosis, and redox

homeostasis⁸⁶. PRODH oxidates proline to P5C in the mitochondria. Regeneration of proline from P5C by PYCR in the cytoplasm produces nicotinamide adenine dinucleotide phosphate (NADP⁺) in the process, which is fed into the pentose-phosphatase pathway, which eventually produces ribose 5-phosphate (R-5-P). R-5-P can be utilized for the synthesis of nucleotides or undergo further transformations to reach fructose 6-phosphate (F-6-P), which is able to produce ATP through glycolysis⁸⁴.

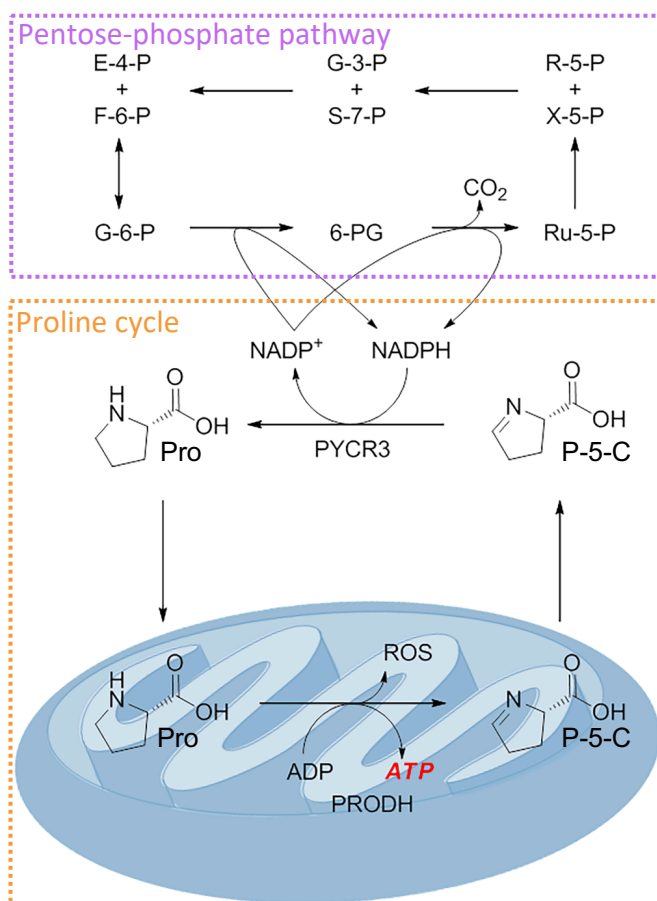


Figure 12: The proline cycle and pentose-phosphate pathway. E-4-P = erythrose 4-phosphate, F-6-P = fructose-6-phosphate, G-3-P = glyceraldehyde 3-phosphate, S-7-P = sedoheptulose 7-phosphate, R-5-P = ribose 5-phosphate, X-5-P = xylulose 5-phosphate, G-6-P = glucose-6-phosphate, 6-PG = 6-phosphogluconic acid, Ru-5-P = ribulose 5-phosphate, NADP⁺ = nicotinamide adenine dinucleotide phosphate, NADPH = nicotinamide adenine dinucleotide phosphate hydrogen, Pro = proline, P5C = pyrroline-5-carboxylate, ATP = adenosine-triphosphate, ADP = adenosine diphosphate, ROS = reactive oxygen species, PYCR3 = pyrroline-5-carboxylate reductase 3, PRODH = proline dehydrogenase. Adapted from Milne et al., *Bioorganic and Medicinal Chemistry Letters* 2019⁸⁴.

In certain cancers, including breast, prostate and some lung and skin cancers, PYCR1 has been found to be upregulated^{84,85}. PYCR1 knockdown or inhibition can halt tumor growth, or even promote tumor regression in mouse models. Moreover, PYCR1 inhibitors have been developed and entered clinical trials for their potential as anti-tumor drugs^{84,87}. However, the potential for PYCR1 inhibition to extend lifespan remains unknown, but will be investigated in this thesis.

1.6 Forward genetic screens

C. elegans is an excellent invertebrate animal model to quickly and easily generate millions of mutagenized worms for screening purposes. It has a short generation time of about four days and produces about 300 larval offspring from self-fertilization or mating. Exposure to ethyl methanesulfonate (EMS) results in genomic single nucleotide polymorphisms (SNPs), where in effect G/C base pairs are transformed into A/T base pairs⁸⁸. Occasionally, the toxin can lead to deletions or frame shifts. However, an A/T to G/C transformation is very rare. Consequently, it is unlikely to generate new codons for hydrophobic amino acids leucine (CC.) and valine (GC.), and the small neutral amino acid glycine (GG.). This is a limitation of using EMS for mutagenesis. Nevertheless, forward genetic screens are extremely powerful in that they can help identify loss-of-function and gain-of-function mutations at the single nucleotide and amino acid resolution. Forward genetic screens helped me identify a novel gain-of-function mutation for glutamine-fructose-6-phosphate amidotransferase GFAT-1 (published with Sabine Ruegenberg in *Nature Communications* in 2021⁸⁹), collaborate on a loss-of-function kinesin OSM-3 mutant (published with Gabriel Guerrero and Maxime Derisbourg in *eLife* in 2021⁹⁰), and identify a novel loss-of-function pyrroline-5-carboxylate reductase 1 PYCR-1 mutant (the focus of this thesis).

1.7 Aims of this thesis

This thesis interrogates a multitude of phenotypes associated with hallmarks of ageing to investigate the longevity of a novel *de novo* proline biosynthesis *C. elegans* mutant *pycr-1(wrm22)*. In short, using an unbiased approach applying chemical mutagenesis⁸⁸ in *C. elegans*, I screened for genes whose mutation protects against the ribosomal inhibitor geneticin (G418). I identified a causal mutation in *pyrroline-5-carboxylate reductase-1* (*pycr-1*) of the *de novo* proline biosynthesis pathway. *pycr-1* mutants were long-lived and I detected reduced S-adenosylmethionine (SAM) levels as a consequence of altered proline and polyamine metabolism. SAM depletion in turn likely depleted histone methylation to promote HSF-1 target gene expression, extending lifespan. Evidently, ageing research has not pinpointed a singular cause for ageing, but several hallmarks for which protective mechanisms interconnect to safe-guard organism survival. This interconnectivity plays a key role in the research presented in this thesis.

The aims to uncover in this thesis are:

- Aim 1:** Is G418 toxicity a useful proxy to select mutagenized worms for longevity?
- Aim 2:** Which molecular mechanisms protect from G418 toxicity?
- Aim 3:** Are the same mechanisms involved in extending lifespan?
- Aim 4:** Are these mechanisms evolutionarily conserved?

2 Results

2.1 The *wrm22* allele ameliorates G418 toxicity and extends lifespan

To genetically probe the role of the ribosome as a stress sensor and potential links to resilience and longevity, I performed a developmental G418 resistance screen in *C. elegans*. G418 is a protein synthesis inhibitor⁹¹ and perturbs translational fidelity^{92,93}. The screen was adapted from Denzel et al.⁴³ to select ethyl methanesulfonate (EMS) mutagenized *C. elegans* nematodes for developmental resistance to the wildtype (WT) lethal dose of 1 mM G418. I screened approximately 1,250,000 genomes for G418 resistance and isolated 16 independent mutants (Figure 13a, b). Importantly, to increase the chance of finding novel regulators of longevity I showed that well-characterized longevity mutants *daf-2(e1370)*, *glp-1(e2141ts)* and *rsk-1(sv31)* failed to develop in the presence of 1 mM G418 (Figure 13c). Lifespan analyses of G418 resistant mutants were performed after outcrossing to the maternal WT strain. I found an enrichment (10/16) for long-lived strains (Figure 13b) and focused my investigation on the *wrm22* allele, which conferred strong G418 resistance (Figure 13d) and the largest lifespan extension (Figure 13b, e).

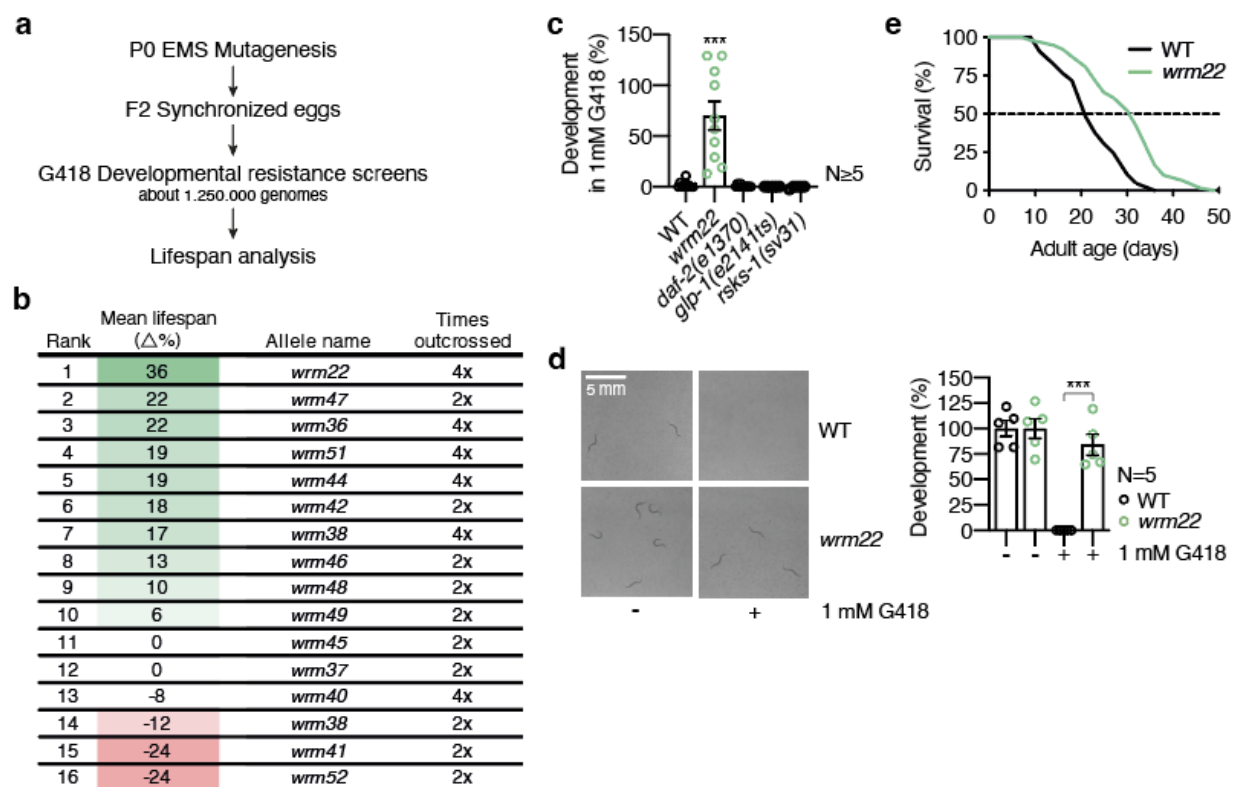


Figure 13: The *wrm22* mutation ameliorates G418 toxicity and extends lifespan

a, Whole genome forward genetic screening strategy. **b**, Lifespan table of G418 resistant EMS mutagenized worm strains displaying how many times the strains were outcrossed to WT before lifespan analysis and the mean and median percent difference to WT lifespan. **c**, Developmental G418 resistance assay of WT and

indicated mutants treated with 1 mM G418 (error bars represent means \pm SEM, two-sided Student's t-test, *** $p < 0.001$ vs WT worms treated from hatch with 1 mM G418, N=10 for WT, *pycr-1(wrm22)* and *daf-2(e1370)*, N=5 for *glp-1(e2141ts)* and *rsk-1(sv31)* mutants). **d**, Developmental G418 resistance assay of WT and *wrm22* mutants treated from hatch with 1 mM G418. (left) Images of worms grown on NGM plates with 1 mM G418 in the agar. (right) Quantification of worms grown in liquid culture containing 1 mM G418 (error bars represent means \pm SEM, two-sided Student's t-test, *** $p < 0.001$ vs WT worms treated with 1 mM G418). **e**, Survival of WT and *wrm22* mutant worms grown on OP50 bacteria under standard conditions, log-rank (Mantel-Cox) test $p < 0.0001$. See Supplementary Table 1 for lifespan statistics.

2.2 The SNP in *pycr-1* is the causal mutation of the *wrm22* allele

To identify causal mutations, *wrm22* was outcrossed to the Hawaiian WT strain CB4856, and whole genome sequencing, followed by single nucleotide polymorphism (SNP) mapping, was performed to identify candidate causative SNPs for *wrm22*, as previously described⁹⁴ (Figure 14a). Normalized linkage score identified SNPs in exons of six candidate genes located on the X chromosome (Figure 14b). I reasoned that RNA interference (RNAi) mediated knockdown⁹⁵ could phenocopy loss-of-function alleles. Indeed, knockdown by RNAi of M153.1, which is predicted to be the worm homolog of human PYCR1, in WT worms resulted in resistance to otherwise lethal levels of G418, while the knockdown of other candidates had no effect on G418 resistance (Figure 14c). Therefore, I termed *M153.1 pycr-1*. To validate the *pycr-1(wrm22)* EMS mutant, I tested whether CRISPR mutants phenocopy *pycr-1(wrm22)*. Indeed, *pycr-1* deletion or G246E substitution in *pycr-1(syb2745)* and *pycr-1(syb2974)* respectively, obtained by CRISPR-Cas9 genome editing, resulted in G418 resistance. Both mutants showed similar G418 resistance as the EMS mutant *pycr-1(wrm22)* of around 75% compared to WT worms (Figure 14d). I conclude that G246E is a loss-of-function mutation that was causal for the *pycr-1(wrm22)* phenotypes.

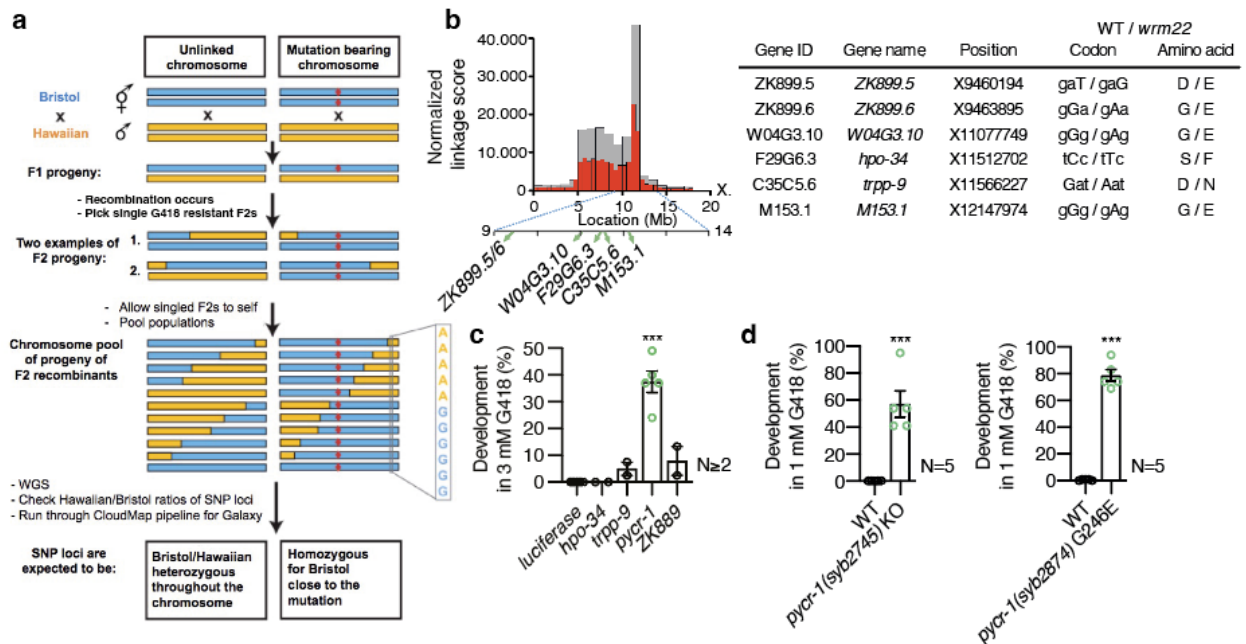


Figure 14: The SNP in *pycr-1* is the causal mutation of the *wrm22* allele

a, Hawaiian outcrossing and SNP mapping strategy. Adapted from Doitsidou et al., *PloS one* 2010⁹⁶. **b**, (left) Frequency plot of normalized parental alleles on the X-chromosome of *wrm22*. The CloudMap Hawaiian Variant Mapping With WGS tool displays regions of linked loci where pure parental allele SNPs instead of Hawaiian SNPs are over-represented. Gray bars represent 1-Mb and red bars represent 0.5-Mb sized bins. (right) Table of candidate non-synonymous EMS SNPs between 9 and 14-Mb on the X-chromosome of *wrm22* mutants. **c**, Developmental G418 resistance assay of synchronized WT progeny of worms grown a full generation on target RNAi, treated from hatch with 3 mM G418 and target RNAi (error bars represent means \pm SEM, 2-way ANOVA multiple comparisons Tukey test, *** p <0.001 vs worms treated from hatch with *luciferase* RNAi and 3 mM G418). **d**, (left) Developmental G418 resistance assay of WT and *pycr-1*(*syb2745*) deletion mutants treated from hatch with 1 mM G418 (error bars represent means \pm SEM, two-sided Student's t-test, *** p <0.001 vs WT). (right) Developmental G418 resistance assay of WT and *pycr-1*(*syb2874*) G246E mutants treated from hatch with 1 mM G418 (error bars represent means \pm SEM, two-sided Student's t-test, *** p <0.001 vs WT).

2.3 Alignment of *C. elegans* PYCR-1 and PYCR-1(*wrm22*) with *H. sapiens* PYCR1

M153.1 is well conserved between *C. elegans* and its *Homo sapiens* homolog pyrroline-5-carboxylate reductase 1 (PYCR1): 50% of amino acid (AA) sequence is identical (Figure 15a). Therefore, I formally designated M153.1 as pyrroline-5-carboxylate reductase-1 (PYCR-1). PYCR-1 potentially synthesizes proline from 1-pyrroline-5-carboxylate or 4-hydroxyproline from 1-pyrroline-3-hydroxy-5-carboxylate, using proton donor NAD(P)H, as its human homologue. The *wrm22* mutant carries a SNP in *pycr-1* that translates into a codon change from gGg (glycine) to gAg (glutamic acid) at the conserved amino acid position 246 (Figure 15a).

The structure of human PYCR1 has previously been resolved⁹⁷ (Figure 15b). I superimposed the human PYCR1 monomer with the predicted secondary structure of worm PYCR-1 that I generated using Alphafold (Figure 15c). The predicted secondary structure of worm PYCR-1 is strikingly similar to that of human PYCR1; thus, it is plausible that worm PYCR-1 similarly is an obligate dimer. It was reported that human PYCR1 catalytic activity is the property of PYCR1 dimers, whereas the physiological structure is a pentamer-of-dimers decamer⁹⁸. The *pycr-1(wrm22)* G246E mutation, however, is not located at the catalytic or NAD(P)H binding site, but, interestingly, at the two-fold symmetry of the two monomers where they are positioned next to each other (Figure 15b, d and e). AlphaFold does not predict that the two glutamates in *pycr-1(wrm22)* sterically interfere, but the strong negative charges of the two glutamates next to each other could have a repulsive effect interfering with dimerization, and thus, catalytic activity.

Molecular Biology 2006⁹⁷. **c**, Superimposition of human PYCR1 (grey) and WT *C. elegans* PYCR-1 (green). The structure of PYCR-1 has been generated by AlphaFold. **d**, **e**, Close-up view of the position of G247 (**d**) and G247E (**e**) (sticks) shows that G247E orientation is predicted to be outward.

2.4 *pycr-1(wrm22)* fecundity is mildly reduced

Under standard culture conditions *pycr-1(wrm22)* worms showed no obvious phenotypes, but careful analysis showed that development was slightly delayed by about 6 hours (Figure 16a) and fecundity was slightly reduced (Figure 16b), compared to WT worms. Egg laying was slightly decreased for the first three days of adulthood, and slightly improved for the days thereafter (Figure 16c). Although reduced fecundity is linked to longevity⁹⁹, the mild effect on fecundity is unlikely to explain the drastic lifespan extension of *pycr-1(wrm22)* mutants.

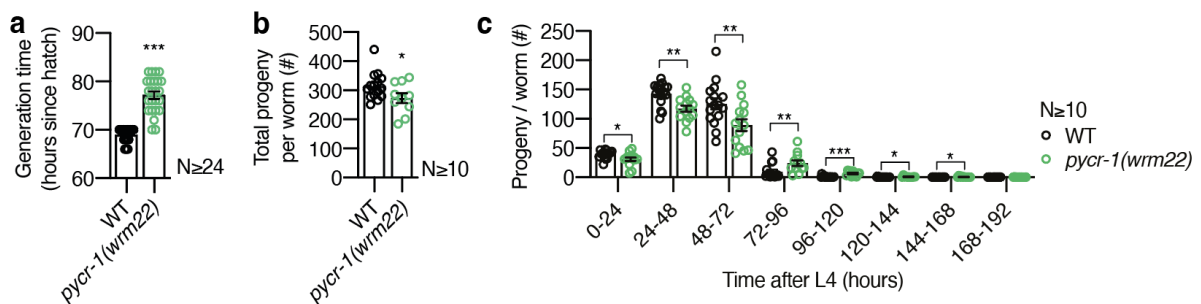


Figure 16: *pycr-1(wrm22)* fecundity is mildly reduced

a, Generation time of WT and *pycr-1(wrm22)* mutants (error bars represent means ± SEM, two-sided Student's t-test, ***p<0.001 vs WT worms). **b**, Total progeny of WT and *pycr-1(wrm22)* mutants (error bars represent means ± SEM, two-sided Student's t-test, *p<0.05 vs WT worms). **c**, Progeny in 24h bins from L4 stage on of WT and *pycr-1(wrm22)* mutants (error bars represent means ± SEM, two-sided Student's t-test, *p<0.05, **p<0.01, ***p<0.001 vs WT worms in the same bin).

2.5 *pycr-1(wrm22)* G418 resistance is independent of proline level

Since PYCR-1 loss-of-function, knockout or knockdown by RNAi resulted in G418 resistance in WT worms, G418 resistance of *pycr-1(wrm22)* mutants might plausibly be explained by a reduced proline level. To test this possibility, I supplemented *pycr-1(wrm22)* worms with 25 mM proline in the food and tested for G418 resistance. Surprisingly, feeding proline to *pycr-1(wrm22)* worms did not abolish G418 resistance (Figure 17a), although proline was readily taken up by the animals as measured by LC-MS analysis (Figure 17b).

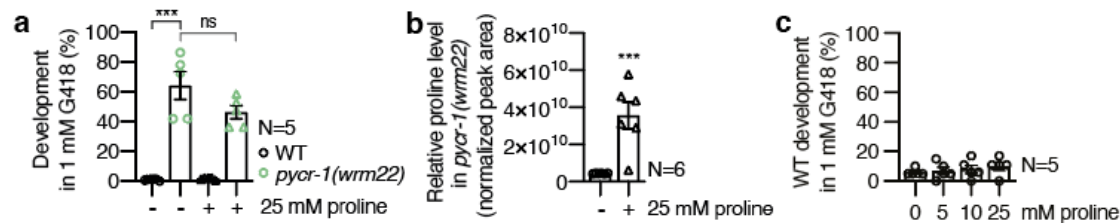


Figure 17: *pycr-1(wrm22)* G418 resistance is independent of proline levels

a, Developmental G418 resistance assay of WT and *pycr-1(wrm22)* mutants treated from hatch with 25 mM proline and 1 mM G418 (error bars represent means \pm SEM, 2-way ANOVA multiple comparisons Tukey test, ns = not significant, *** $p < 0.001$). **b**, Relative proline levels of day 1 adult *pycr-1(wrm22)* mutants treated with 25 mM proline for 3h, measured by LC-MS (error bars represent means \pm SEM, two-sided Student's t-test, *** $p < 0.001$). **c**, Developmental G418 resistance assay of WT worms treated from hatch with 5, 10 or 25 mM proline and 1 mM G418 (error bars represent means \pm SEM, 2-way ANOVA multiple comparisons Tukey test showed no significant differences).

Alternatively, *pycr-1(wrm22)* G418 resistance could possibly be explained by a potential accumulation of pyrroline-5-carboxylate (P5C). Moreover, PYCR1 activity is inhibited by a high concentration of its product proline¹⁰⁰, thus, I speculated that supplementing WT worms with proline could inhibit PYCR-1 activity and lead to a buildup of P5C. Unfortunately, we were unable to confirm elevated P5C levels by liquid chromatography-mass spectrometry (LC-MS), as this metabolite is highly unstable. Nevertheless, proline supplementation was not sufficient to induce G418 resistance in WT worms (Figure 17c). Together, this indicates that G418 resistance is modulated through an alternative mechanism than proline level.

2.6 *pycr-1(wrm22)* protein synthesis is mildly protected from inhibition

Aminoglycosides such as gentamicin and G418 target the small ribosomal subunit and thereby hinder protein synthesis, leading to misincorporation of amino acids into the polypeptide chain and an overall reduction of protein synthesis³⁹. It is believed that it is the generation and aggregation of aberrant proteins that causes G418 toxicity^{93,101}. Ribosomes are not all assembled equally, but there exists a degree of heterogeneity in composition, post-transcriptional and post-translational modification of ribosomal RNAs (rRNAs) and ribosomal proteins^{102–104}.

I speculated that ribosomal composition or function could be altered in *pycr-1(wrm22)* mutants, and that this would lead to reduced interaction with G418. To test this, I performed puromycin incorporation assays, which is a measure of elongation activity of protein synthesis. Surprisingly, elongation activity is slightly increased in *pycr-1(wrm22)* mutants, and, similarly to WT inhibited by G418 (Figure 18a). WT puromycin incorporation was approximately

halved upon cycloheximide or 5 mM G418 treatment and a similar trend was observed for *pycr-1(wrm22)*. Interestingly, there is a trend that puromycin incorporation was higher for *pycr-1(wrm22)* upon cycloheximide or G418 treatment than for WT worms (Figure 18a), thus

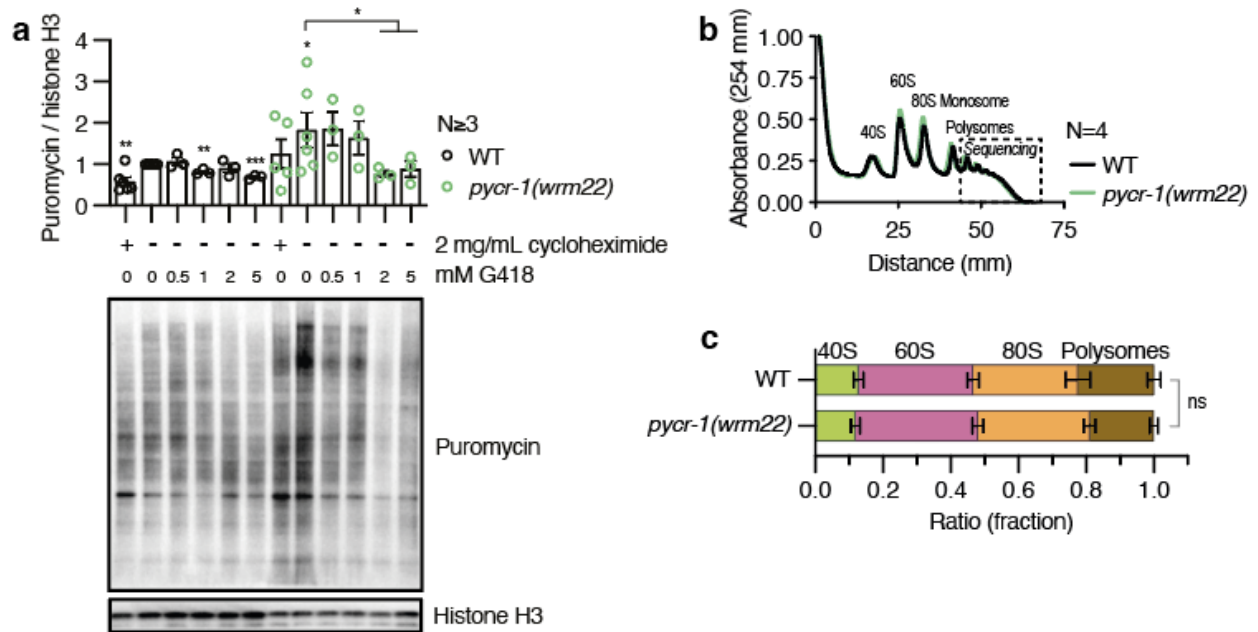


Figure 18: *pycr-1(wrm22)* protein synthesis is mildly protected from inhibition

a, Representative western blot analysis and its quantification of puromycin incorporation of WT and *pycr-1(wrm22)* mutants treated from L4 with 2 mg/mL cycloheximide as a positive control or 0.5, 1, 2 or 5 mM G418 for 3h (error bars represent means \pm SEM, 2-way ANOVA multiple comparisons Tukey test, *p<0.05, **p<0.01, ***p<0.001 vs untreated WT worms unless indicated otherwise). **b**, **c**, Polysome profiling and quantification of day 1 adult WT worms and *pycr-1(wrm22)* mutants. Quantification represents the relative abundance of ribosomal 40S and 60S subunits, monosomes and polysomes (error bars represent means \pm SEM, 2-way ANOVA Dunnett's post hoc test, ns = not significant).

it is possible that protein synthesis is mildly protected from its inhibition by ribosome inhibitors. However, I did not find evidence of altered composition of ribosomes by polysome profiling (Figure 18b, c). In summary, it is unlikely that ribosomal function or composition is significantly altered and causative to mediate G418 resistance in *pycr-1(wrm22)* mutants.

2.7 *pycr-1(wrm22)* is broadly resistant to ribosome inhibitors

Cycloheximide and G418 both obstruct mRNA-tRNA translocation of the elongation step, however, other ribosome inhibitors such as anisomycin and blasticidin S interfere with peptide-bond formation to inhibit elongation (Figure 19a)³⁹. To investigate whether *pycr-1(wrm22)* mutants are only resistant to a specific class of ribosome inhibitors, I performed developmental assays in presence of lethal concentrations of these inhibitors. Interestingly, *pycr-1(wrm22)* mutants showed resistance to all three inhibitors (Figure 19b, c, d), which was strongest for

cycloheximide (Figure 19d) and weakest for blasticidin S (Figure 19c). These results show that *pycr-1(wrm22)* is broadly resistant to ribosome inhibitors, and thus, that G418 resistance is unspecific.

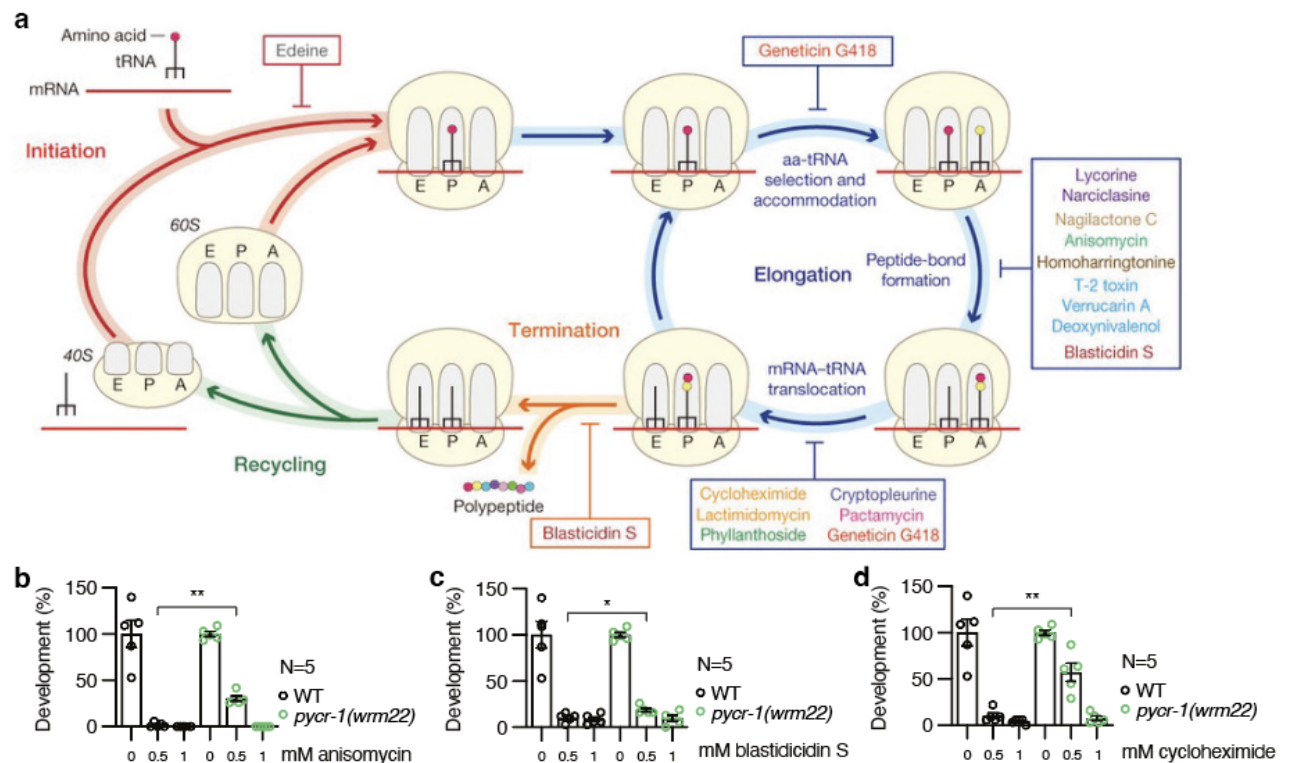


Figure 19: *pycr-1(wrm22)* is broadly resistant to ribosome inhibitors

a, Schematic showing the steps of protein synthesis in eukaryotes targeted by ribosome inhibitors. Taken from de Loubresse et al., *Nature* 2014³⁹. **b**, **c**, **d**, Developmental G418 resistance assays of WT and *pycr-1(wrm22)* mutants treated from hatch with 0.5 or 1 mM anisomycin (**b**), blasticidin S (**c**) or cycloheximide (**d**) (error bars represent means \pm SEM, two-sided Student's t-test, *p<0.05, **p<0.01 vs equally treated WT worms).

2.8 *pycr-1(wrm22)* is resistant to oxidative and heat stress

The broad resistance of *pycr-1(wrm22)* mutants to ribosome inhibitors suggests that it might have a more general improved stress resistance. Paraquat induces oxidative stress by generation of reactive oxygen species (ROS)¹⁰⁵, and increased temperatures induce endoplasmic reticulum (ER) stress by misfolding of proteins^{106,107}. Survival analyses confirmed that *pycr-1(wrm22)* mutants were broadly resistant to multiple stressors, including oxidative stress (Figure 20a) and heat stress (Figure 20b). A general and broad resistance to diverse stressors hint to enhanced activation of stress response pathways in *pycr-1(wrm22)* mutants.

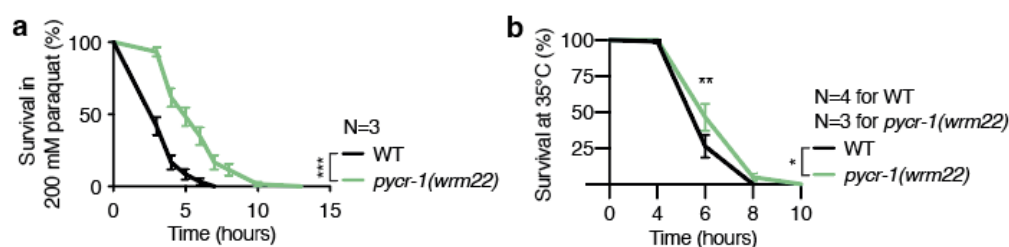


Figure 20: *pycr-1(wrm22)* is resistant to oxidative and heat stress

a, Developmental paraquat resistance assay of WT and *pycr-1(wrm22)* mutants treated from hatch with 200 mM paraquat (error bars represent means ± SEM, Mantel-Cox log-rank statistical test, *** $p < 0.001$ vs treated WT worms). **b**, Heat stress survival of day 1 adult WT and *pycr-1(wrm22)* mutants at 35°C (error bars represent means ± SEM, Mantel-Cox log-rank statistical test, * $p < 0.05$, ** $p < 0.01$ vs treated WT worms).

2.9 SAM depletion leads to G418 resistance

Since G418 resistance was independent of proline levels (Figure 17), I investigated other related metabolic pathways. The *de novo* proline biosynthesis pathway shares glutamate-5-semialdehyde (G-5-S) as substrate with the *de novo* polyamine biosynthesis pathway (Figure 21a). I speculated that *pycr-1* loss-of-function might impact the polyamine biosynthesis pathway indirectly. To identify potential metabolic changes underlying the *pycr-1(wrm22)* phenotypes, I performed LC-MS and profiled proteinogenic amino acids, polyamines, and compounds of the methionine cycle. *pycr-1(wrm22)* worms showed a 28% reduction of proline and 33% reduction of 4-hydroxyproline levels (Figure 21b, c). This suggests that under replete culture conditions, proline levels were largely maintained although *de novo* proline biosynthesis was perturbed. This is in line with the observation that proline supplementation did not rescue the *pycr-1(wrm22)* G418 resistance (Figure 17a).

The most pronounced metabolic change in *pycr-1(wrm22)* mutants was a 75% reduction in S-adenosyl methionine (SAM) level (Figure 21b), resulting in a reduced SAM versus S-adenosyl homocysteine (SAH) ratio (Figure 21d). Interestingly, the methionine salvage pathway is linked to proline biosynthetic intermediates through the polyamine biosynthesis pathway (Figure 21a): G-5-S is an intermediate of *de novo* proline biosynthesis and the precursor of ornithine. Polyamine biosynthesis depends on the methionine cycle as it consumes decarboxylated SAM (dcSAM)^{73,108} that is synthesized by SAM decarboxylases from SAM and methionine¹⁰⁹. Increased precursor levels resulting from *pycr-1(wrm22)* mutation might thus elevate polyamine pathway activity, depleting SAM. To test this possibility, I artificially elevated polyamine levels by supplementing ornithine (Figure 21e). Indeed, ornithine supplementation significantly depleted SAM (Figure 21f) and resulted in developmental G418

resistance in WT worms (Figure 21g). Supplementation of the downstream intermediate for polyamine biosynthesis, putrescine, was also sufficient to induce G418 resistance (Figure 21h), but supplementation of the polyamine spermidine was not (Figure 21i).

SAM is synthesized from methionine by SAM synthases. The depletion of methionine or inhibition of SAM synthases (SAMS-1, SAMS-3, SAMS-4 and SAMS-5) are an alternative, albeit direct, route to deplete SAM level (Figure 21j). Indeed, the quadruple, but not singular, knockdown by RNAi of the four *C. elegans* SAM synthases induced G418 resistance in WT

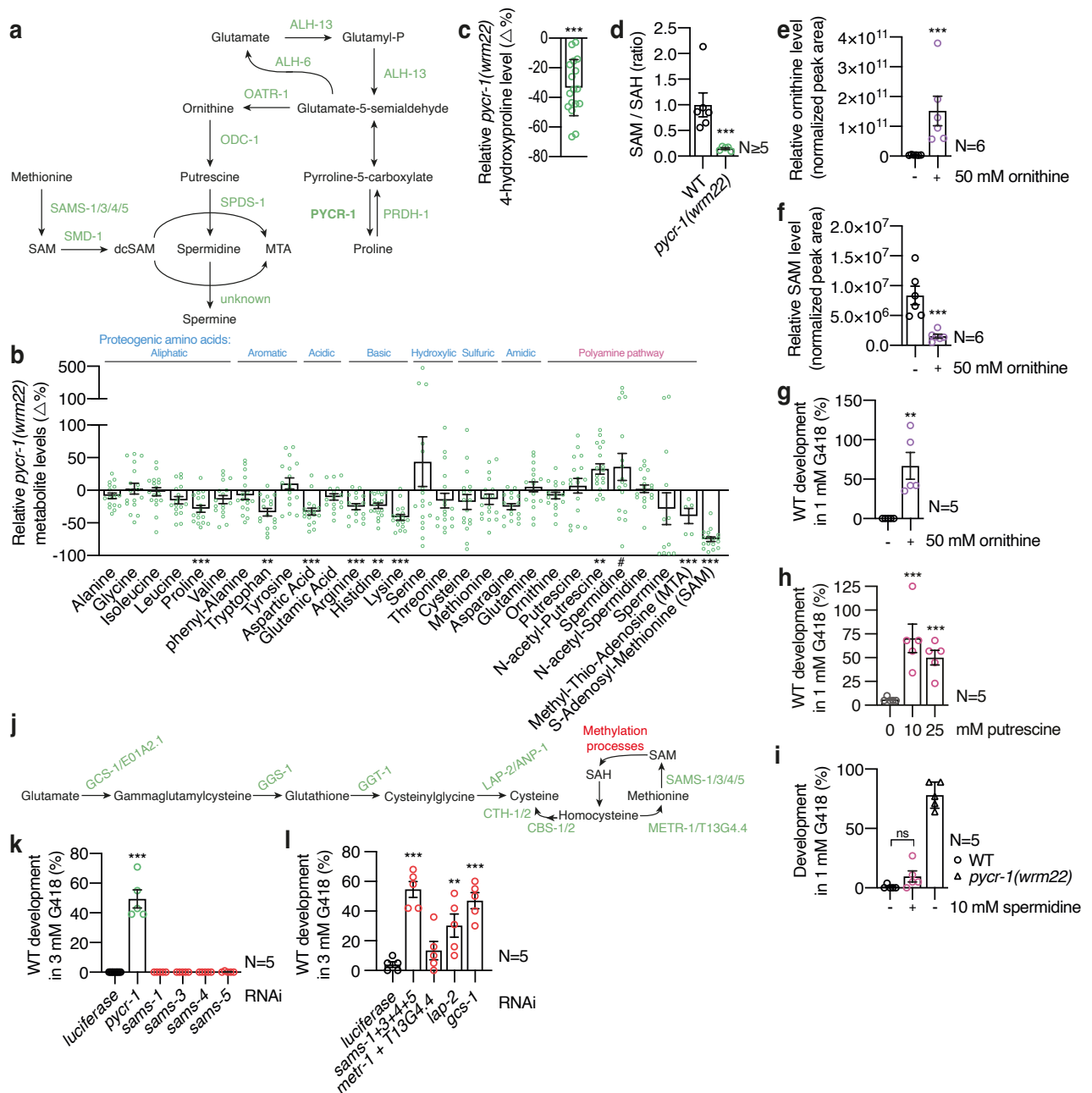


Figure 21: SAM depletion leads to G418 resistance

a, Schematic of the interlinked *de novo* proline and polyamine biosynthesis pathways. **b**, LC-MS-based metabolome analysis in *pycr-1(wrm22)* mutants compared to WT worms. Relative percent difference of

indicated metabolites is displayed (error bars represent \pm SEM calculated by error propagation of 6 independent experiments, two-sided Student's t-test, # $p=0.055$, * $p<0.05$, ** $p<0.01$, *** $p<0.001$, at least five biological replicates for each measurement). **c**, Relative percent difference of *pycr-1(wrm22)* 4-hydroxyproline levels compared to WT worms, measured by LC-MS (error bars represent \pm SEM calculated by error propagation of 6 independent experiments, two-sided Student's t-test, *** $p<0.001$, N=5 or N=6 biological replicates for each experiment). **d**, SAM/S-adenosylhomocysteine (SAH) ratio in day 1 adult WT and *pycr-1(wrm22)* mutants, measured by LC-MS (error bars represent \pm SEM calculated by error propagation of 6 independent experiments, two-sided Student's t-test, *** $p<0.001$, N=6 for WT and N=5 for *pycr-1(wrm22)*). **e**, Relative ornithine levels of day 1 WT worms treated with 50 mM ornithine for 3h, measured by LC-MS (error bars represent means \pm SEM, two-sided Student's t-test, *** $p<0.001$). **f**, Relative ornithine levels of day 1 adult WT worms treated with 50 mM ornithine for 3h, measured by LC-MS (error bars represent means \pm SEM, two-sided Student's t-test, *** $p<0.001$). **g, h, i**, Developmental G418 resistance assays of WT and *pycr-1(wrm22)* mutants treated from hatch with 50 mM ornithine (**g**), or, 10 or 25 mM putrescine (**h**), or, 10 mM spermidine (**i**) and 1 mM G418 (error bars represent means \pm SEM, two-sided Student's t-test, ns = not significant, ** $p<0.01$, *** $p<0.001$). **j**, Schematic of the interlinked *de novo* cysteine biosynthesis pathway and the methionine cycle. **k**, Developmental G418 resistance assay of synchronized WT progeny of worms grown a full generation on target RNAi, treated from hatch with 3 mM G418 and target RNAi (error bars represent means \pm SEM, 2-way ANOVA multiple comparisons Tukey test, *** $p<0.001$ vs worms treated from hatch with *luciferase* RNAi and 3 mM G418). **l**, Developmental G418 resistance assay of synchronized WT progeny of worms grown a full generation on target RNAi, treated from hatch with 3 mM G418 and target RNAi (error bars represent means \pm SEM, 2-way ANOVA multiple comparisons Tukey test, ** $p<0.01$, *** $p<0.001$ vs worms treated from hatch with *luciferase* RNAi and 3 mM G418).

worms (Figure 21k,l). Similarly, the simultaneous knockdown of methionine synthases METR-1 and T13G4.4 shows a trend for G418 resistance (Figure 21l). Methionine is recovered in the methionine cycle from homocysteine (Figure 21j). Homocysteine, however, can also be a substrate for cysteine biosynthesis. Thus, the depletion of cysteine is a potential alternative route to deplete methionine and SAM. Indeed, knockdown by RNAi of leucine aminopeptidase LAP-2 is sufficient to induce G418 resistance in WT worms (Figure 21k), indicating that cysteine depletion is indeed an alternative route to deplete SAM and induce G418 resistance. Additionally, the knockdown of gamma glutamylcysteine synthase GCS-1 by RNAi, which is further upstream and essential for cysteine biosynthesis, is similarly efficient to induce G418 resistance to WT worms (Figure 21k). Together, these data suggest that SAM depletion and not elevation of polyamines was linked to *pycr-1(wrm22)* G418 resistance.

2.10 SAM repletion abolishes G418 resistance and longevity in *pycr-1(wrm22)*

To prove that SAM depletion is causal for G418 resistance and longevity of *pycr-1(wrm22)* mutants, I hypothesized that SAM depletion is able to rescue these phenotypes. Since SAM is synthesized by SAM synthases from methionine⁷³, I supplemented *pycr-1(wrm22)* mutants

with 25 mM methionine, which was sufficient to elevate SAM levels (Figure 22a) and abolish G418 resistance (Figure 22b). Similarly, methionine supplementation suppressed the protective effect of ornithine (Figure 22c). Moreover, supplementing *pycr-1(wrm22)* worms with cysteine also abolished G418 resistance (Figure 22d). In conclusion, SAM repletion abolishes G418 resistance.

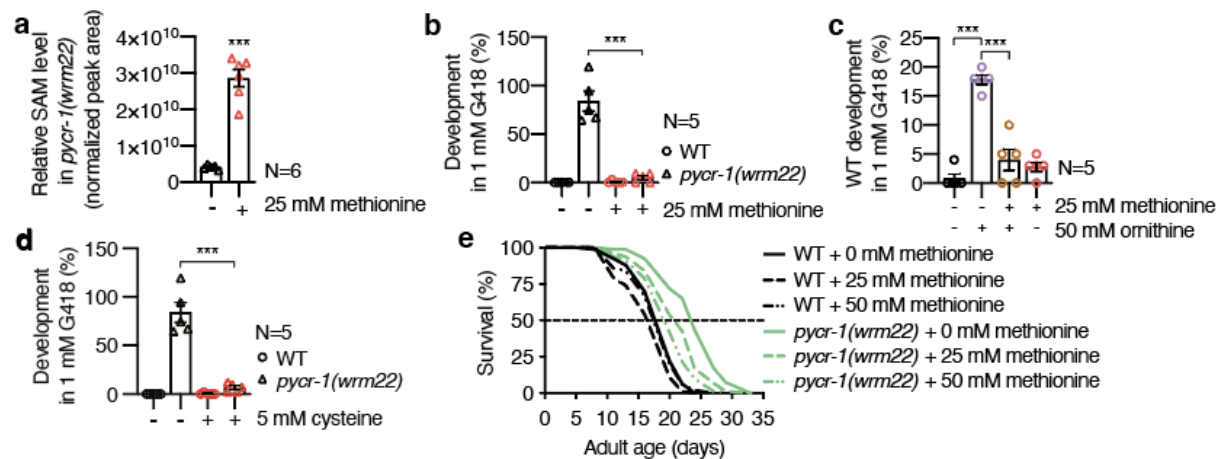


Figure 22: SAM repletion abolishes G418 resistance and longevity in *pycr-1(wrm22)*

a, Relative SAM levels of day 1 adult *pycr-1(wrm22)* mutants treated with 25 mM methionine for 3h, measured by LC-MS (error bars represent means \pm SEM, two-sided Student's t-test, ***p < 0.001). **b**, Developmental G418 resistance assay of WT and *pycr-1(wrm22)* mutants treated from hatch with 25 mM methionine and 1 mM G418 (error bars represent means \pm SEM, 2-way ANOVA multiple comparisons Tukey test, ***p < 0.001). **c**, Developmental G418 resistance assay of WT worms treated from hatch with 25 mM methionine, 50 mM ornithine and 1 mM G418 (error bars represent means \pm SEM, 2-way ANOVA multiple comparisons Tukey test, ***p < 0.001). **d**, Developmental G418 resistance assay of WT and *pycr-1(wrm22)* mutants treated from hatch with 5 mM cysteine and 1 mM G418 (error bars represent means \pm SEM, 2-way ANOVA multiple comparisons Tukey test, ***p < 0.001). **e**, Survival of WT and *pycr-1(wrm22)* mutants on freeze-killed OP50 bacteria treated from hatch with indicated doses of methionine. See Supplementary Table 1 for lifespan statistics.

Reduced SAM levels have been linked to longevity in the context of methionine restriction, metformin treatment, and *sams-1* knockdown^{73–75,108,110}. Thus, I next tested whether methionine supplementation could abrogate *pycr-1(wrm22)* longevity. Indeed, methionine supplementation significantly reduced *pycr-1(wrm22)* longevity in a dose-dependent manner without a consistent effect on WT survival (Figure 22e). This indicates a key role for reduced SAM level in *pycr-1(wrm22)* longevity.

2.11 Proteome and transcriptome analysis of *pycr-1(wrm22)*

To further characterize *pycr-1(wrm22)* mutants and identify pathways that might play a key role downstream of SAM in *pycr-1(wrm22)* longevity I performed transcriptome, transcriptome and proteome analyses. I first focused on the proteome, since this is a direct measure of the

differences in abundance of proteins in *pycr-1(wrm22)* worms, whereas the transcriptome and translome are indirect measures thereof. However, proteomics revealed only a small number (51) of proteins that showed significantly changed levels, of which only half (25) were identified by gene name. I tested the top three most significantly changed and identified proteins by RNA knockdown using silencing RNAs (siRNAs) in G418 resistance assays, to investigate their role in G418 resistance (Figure 23a). Although EPS-8 was significantly less abundant in *pycr-1(wrm22)* mutants, its knockdown by RNA interference (RNAi) was not sufficient to induce G418 resistance in WT worms (Figure 23b). *Vice versa*, the knockdown by RNAi of CATP-3 or PDE-2 was insufficient to sensitize *pycr-1(wrm22)* mutants to G418 (Figure 23b). The proteomics data set proved to be of limited use at this point.

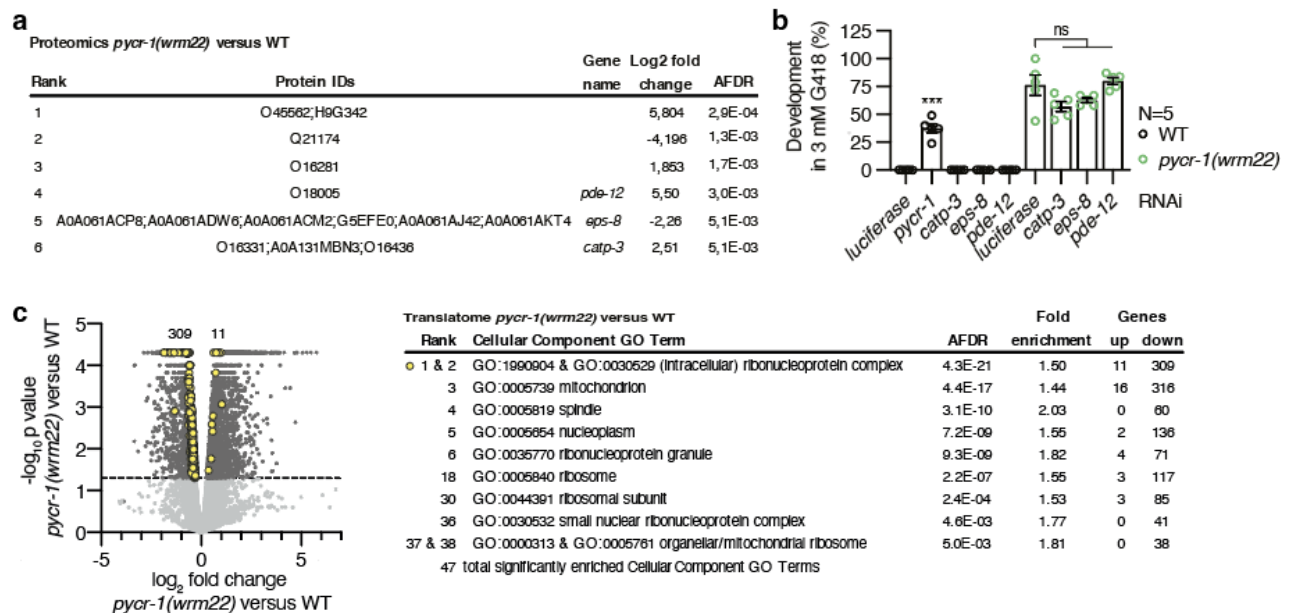


Figure 23: Proteome and translome analysis of *pycr-1(wrm22)*

a, Top six most significantly dysregulated proteins of day 1 adult *pycr-1(wrm22)* mutants vs WT proteomics, ranked by anticipated false discovery rate (AFDR). Full dataset under ProteomeXchange Consortium identifier PXD024215. **b**, Developmental G418 resistance assay of synchronized WT progeny of worms grown a full generation on target RNAi, treated from hatch with 3 mM G418 and target RNAi (error bars represent means \pm SEM, two-sided Student's t-test, ns = not significant, *** $p < 0.001$ vs worms treated from hatch with *luciferase* RNAi and 3 mM G418, unless indicated otherwise). **c**, (left) Volcano plot of polysome-associated mRNAs normalized to total mRNA levels between WT worms and *pycr-1(wrm22)* mutants. Full dataset under GEO Series accession number GSE149325 (two-sided Student's t-test, significance is reached for $p < 0.05$). (right) Selection of enriched Cellular Component GO Term analysis terms of differentially regulated genes, ordered by AFDR as calculated using DAVID^{111,112}.

Next, I characterized *pycr-1(wrm22)* mutants by GO term analysis of the total mRNA and ribosome protected mRNAs. This resulted in an overwhelming number of GO terms for the total mRNA dataset. Polysome association is indicative of higher selective translation of

mRNAs and I compared the ratio of polysome-associated mRNAs (three and more ribosomes/mRNA) normalized to total mRNA between WT and *pycr-1(wrm22)* mutants. In contrast to the overwhelming number of GO terms from the transcriptome analysis, the cellular component GO term analysis of the translome revealed 47 enriched GO terms (Fig 23c).

2.12 *pycr-1(wrm22)* mitochondrial stress is not rescued by SAM repletion

The third ranking GO term “mitochondrion” was of particular interest, because PYCR-1 resides in mitochondria. I speculated that PYCR-1 loss-of-function mutants could elicit a mitochondrial stress response. HSP-6 and HSP-60 are chaperones that mediate a protective response against mitochondrial unfolded protein stress and are frequently used as markers of the mitochondrial unfolded protein response¹¹³. I crossed *pycr-1(wrm22)* with the mitochondrial stress reporters *hsp-6::GFP* and *hsp-60::GFP*. Basal *hsp-6::GFP* level was very low in WT worms, but elevated in *pycr-1(wrm22)* (Figure 24a, b). *hsp-60::GFP* expression was unchanged in *pycr-1(wrm22)* (Figure 24c, d). The mitochondrial UPR prevents proteostasis collapse during ageing¹¹⁴, thus, *pycr-1(wrm22)* G418 resistance and longevity might similarly depend on a mitochondrial stress response. Therefore, I tested whether methionine supplementation would rescue elevated *hsp-6::GFP* expression in *pycr-1(wrm22)* mutants, which was not the case (Figure 24b). This indicates that *pycr-1(wrm22)* G418 resistance and longevity are mediated by an alternative pathway.

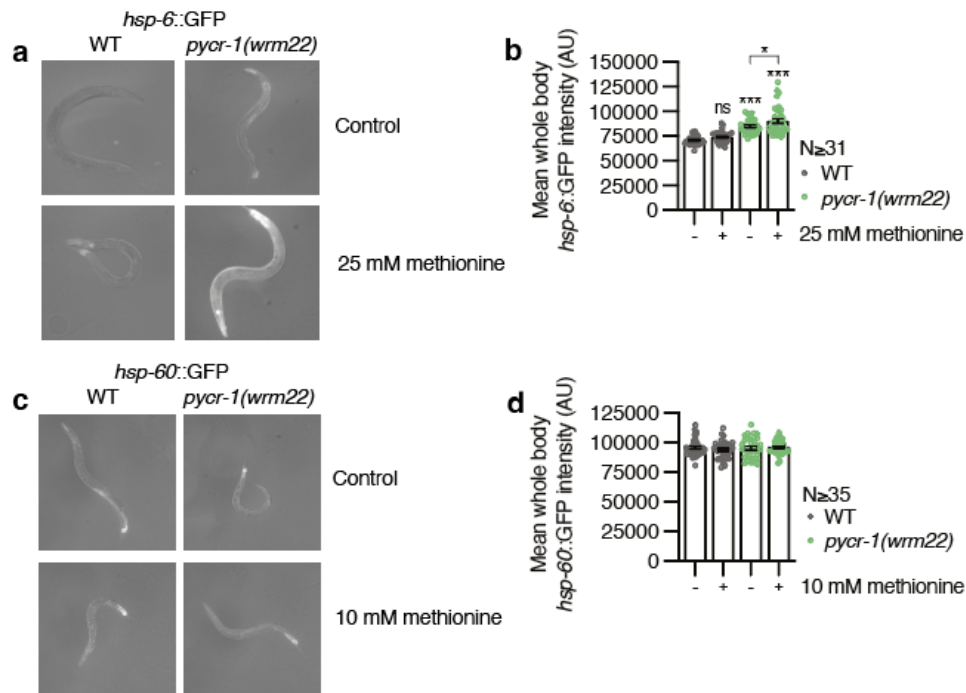


Figure 24: *pycr-1(wrm22)* mitochondrial stress is not rescued by SAM repletion

a, b, Representative images (**a**) and quantification (**b**) of *hsp-6::GFP* expression in *hsp-6::GFP* and *hsp-6::GFP;pycr-1(wrm22)* L4 stage larvae treated from hatch with 25 mM methionine (error bars represent means \pm SEM, 2-way ANOVA multiple comparisons Tukey test, ns = not significant, * $p < 0.05$, *** $p < 0.001$ vs untreated *hsp-6::GFP* worms, unless indicated otherwise). **c, d**, Representative images (**c**) and quantification (**d**) of *hsp-60::GFP* expression in *hsp-60::GFP* and *hsp-60::GFP;pycr-1(wrm22)* L4 stage larva treated from hatch with 10 mM methionine (error bars represent means \pm SEM, 2-way ANOVA multiple comparisons Tukey test, no significant differences were detected).

2.13 *pycr-1(wrm22)* *irg-1* signaling is not rescued by SAM repletion

The *irg-1/zip-2* signaling pathway is activated upon translation inhibition by *Pseudomonas aeruginosa* infection or independent thereof¹¹⁵. Since G418 inhibits protein synthesis, I hypothesized that elevated *irg-1/zip-2* signaling at basal conditions could be protective against G418 toxicity. Indeed, total mRNA RNA-seq data revealed increased *irg-1* transcription in *pycr-1(wrm22)*, which was confirmed by the *irg-1::GFP;pycr-1(wrm22)* cross (Figure 25a, b). Methionine supplementation abolishes G418 resistance and if this goes through increased *irg-1/zip-2* signaling, methionine supplementation should be able to rescue *irg-1::GFP*. However, counterintuitively, methionine supplementation further increased *irg-1::GFP* expression (Figure 25a, b). This indicated that *pycr-1(wrm22)* G418 resistance and longevity go through an alternative mechanism.

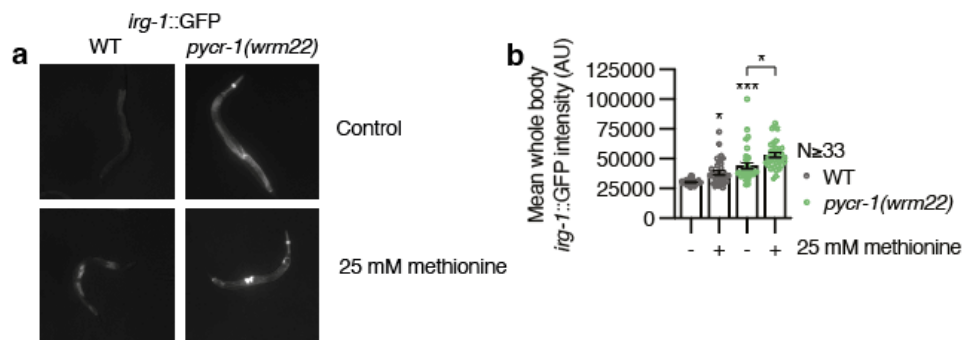


Figure 25: *pycr-1(wrm22)* *irg-1* signaling is not rescued by SAM repletion

a, b, Representative images (**a**) and quantification (**b**) of *irg-1::GFP* expression in *irg-1::GFP* and *irg-1::GFP;pycr-1(wrm22)* L4 stage larva treated from hatch with 25 mM methionine (error bars represent means \pm SEM, 2-way ANOVA multiple comparisons Tukey test, * $p < 0.05$, *** $p < 0.001$ vs untreated *irg-1::GFP* worms, unless indicated otherwise).

2.14 Dysregulated rRNA maturation in *pycr-1(wrm22)* associates with NRDE-3

nuclear localization, but not G418 resistance

Out of the 47 enriched cellular component GO terms, several GO terms were ribosome related (Fig 23c). G418 targets ribosomes and, therefore, ribosome related GO terms were of particular

interest. Polysome sequencing revealed a significant depletion of several mRNAs encoding proteins crucial in ribonucleoprotein complex biogenesis, including ribosomal proteins (Figure 23c, Supplementary Table 2). Surprisingly, total mRNA sequencing did not detect any changes in transcripts coding for cytoplasmic ribosomal proteins, but showed altered mRNA transcript levels of mitochondrial ribosomal proteins (Supplementary Table 2). These data suggest a translational downregulation of select ribogenesis components in *pycr-1(wrm22)* mutants. While the changes observed in ribosomal protein translation did not reach the level to perturb ribosome distribution in the polysome profiles (Figure 18c), they might reflect a compensated deregulation of ribosome biogenesis.

SAM is a key substrate in rRNA maturation (Figure 26a)¹¹⁶ and, thus, I hypothesized that low SAM levels could directly affect ribogenesis. Dysregulated ribogenesis could be associated with altered levels of rRNAs and pre-rRNAs, which I measured by qPCR (Figure 26b-f, Supplementary Table 5). Surprisingly, I found increased pre-rRNA and 18S rRNA levels in *pycr-1(wrm22)* mutants (Figure 26c, d), suggesting an imbalance between rRNA and ribosomal proteins. I observed no changes for 5.8S and 25S rRNA levels (Figure 26e, f). Defects in rRNA maturation, caused for example by mutations in the methyltransferase *susi-2*, have previously been shown to trigger the generation of 22G RNAs, which bind to the argonaute protein NRDE-3 to drive its nuclear localization in a feedback loop that represses rRNA expression^{57,117}. To use NRDE-3 nuclear localization as a sensor for ribosomal assembly stress, I crossed the *pycr-1(wrm22)* allele to the GFP::NRDE-3 reporter in the *eri-1(mg366)* background, which has reduced endogenous antisense ribosomal siRNAs that otherwise induce NRDE-3 nuclear localization⁵⁷. I found significantly increased GFP::NRDE-3 nuclear localization in *eri-1(mg366);GFP::NRDE-3;pycr-1(wrm22)* worms, and upon *susi-2* RNAi treatment in *eri-1(mg366);GFP::NRDE-3* worms as previously reported⁵⁷ (Figure 26g, h). To test whether NRDE-3 nuclear localization would be rescued similarly as G418 resistance and longevity by methionine supplementation, I treated *eri-1(mg366);GFP::NRDE-3;pycr-1(wrm22)* mutants with methionine and measured NRDE-3 localization. Unexpectedly, methionine supplementation did not rescue NRDE-3 nuclear localization (Figure 26i). Moreover, the *pycr-1(wrm22)* cross with the loss-of-function NRDE-3 mutant *nrde-3(gg66)* was equally G418 resistant as single *pycr-1(wrm22)* mutants (Figure 26j). Together, these results indicate that *pycr-1(wrm22)* G418 resistance and longevity is independent of NRDE-3 signaling. Alternatively, I speculated that loss of rRNA methylation could directly affect G418 toxicity by perturbing G418 binding to ribosomes, either by reducing rRNA methylation or by

altering rRNA methylation and consequently (pre-)rRNA levels. Therefore, I performed a mini-screen for G418 resistance by RNAi knockdown of rRNA methyltransferases in WT worms, but none induced G418 resistance (Figure 26k). Altogether, this suggests that perturbed ribogenesis in *pycr-1(wrm22)* mutants is mild and does not account for improved resistance to G418 toxicity or extended lifespan.

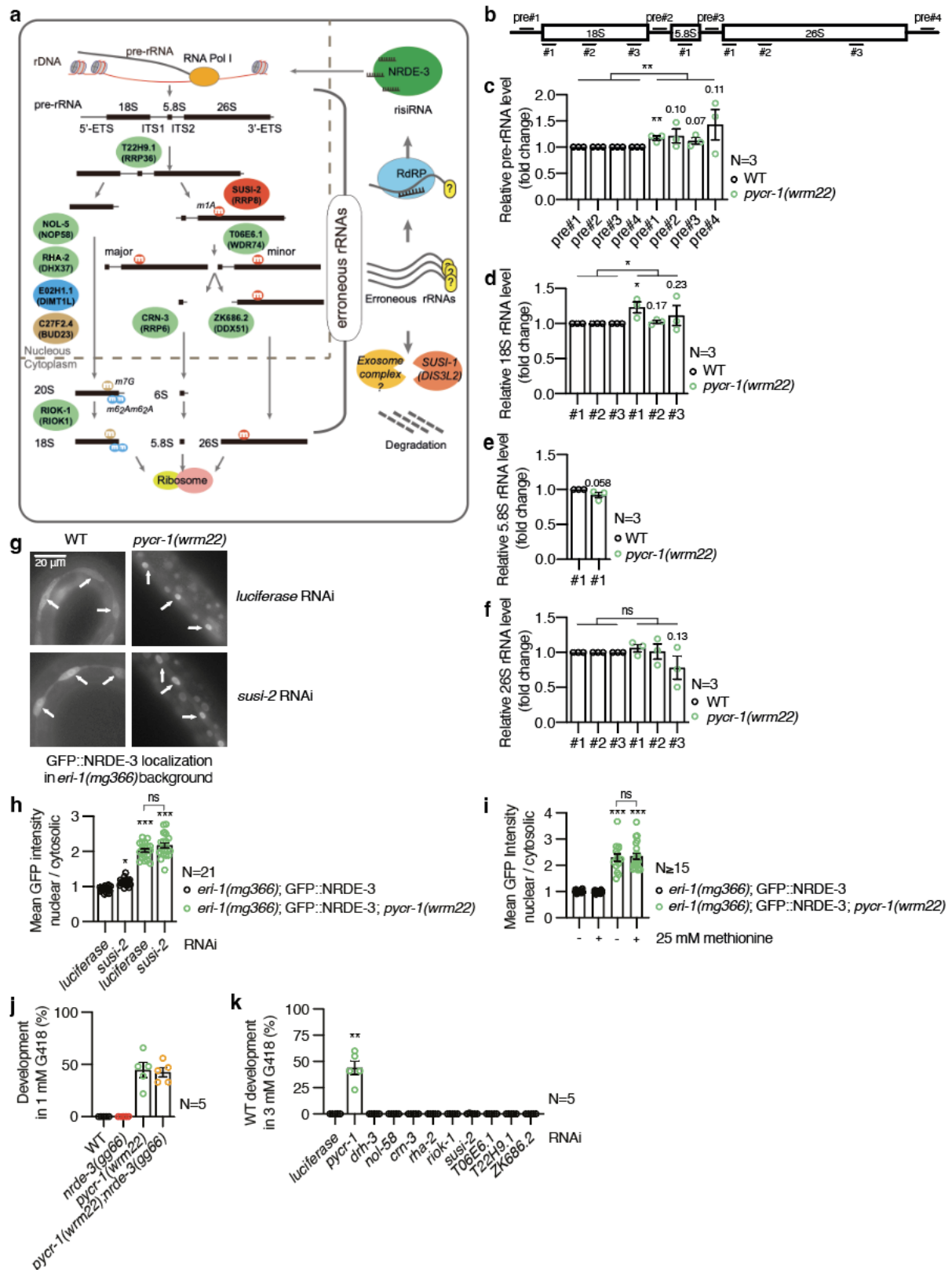


Figure 26: Dysregulated rRNA maturation in *pycr-1(wrm22)* associates with NRDE-3 nuclear localization, but not G418 resistance

a, Schematic of rRNA maturation and working model of risiRNA generation and subsequent activation of NRDE-3 mediated gene silencing to inhibit pre-rRNA expression. Adapted from Zhu et al., *PNAS* 2018⁵⁷. **b**, Schematic of rRNA and location of qRT-PCR target sequences to measure (pre-)rRNA levels. **c, d, e, f**, qRT-PCR assay of pre-, 18S, 5.8S or 26S rRNA levels, respectively, in WT and *pycr-1(wrm22)* worms, where *eft-3* served as an internal control (error bars represent means \pm SEM, two-sided Student's t-test, ns = not significant, * $p < 0.05$, ** $p < 0.01$ vs WT, unless indicated otherwise). **g, h**, GFP::NRDE-3 localization in seam cells of L3 stage larvae after two generations of RNAi treatment in *eri-1(mg366);GFP::NRDE-3* and *pycr-1(wrm22);eri-1(mg366);GFP::NRDE-3* worms. **g**, Representative images, arrows indicate nuclei. **h**, Relative quantification of mean GFP intensity of the nucleus compared to the cytosol of three seam cells per worm, each dot represents an individual worm (error bars represent means \pm SEM, 2-way ANOVA multiple comparisons Tukey test, ns = not significant, * $p < 0.05$, *** $p < 0.001$ vs WT worms treated from hatch with *luciferase* RNAi, unless indicated otherwise). **i**, GFP::NRDE-3 localization in seam cells of L3 stage larvae after 2 generations of 25 mM methionine treatment in *eri-1(mg366);GFP::NRDE-3* and *pycr-1(wrm22);eri-1(mg366);GFP::NRDE-3* worms (error bars represent means \pm SEM, 2-way ANOVA multiple comparisons Tukey test, ns = not significant, *** $p < 0.001$ vs untreated *eri-1(mg366);GFP::NRDE-3* worms, unless indicated otherwise). **j**, Developmental G418 resistance assay of WT and indicated mutants treated with 1 mM G418 (error bars represent means \pm SEM, two-sided Student's t-test, *** $p < 0.001$ vs WT worms treated from hatch with 1 mM G418). **k**, Developmental G418 resistance assay of synchronized WT progeny of worms grown a full generation on target RNAi, treated from hatch with 3 mM G418 and target RNAi (error bars represent means \pm SEM, 2-way ANOVA multiple comparisons Tukey test, ** $p < 0.01$ vs worms treated from hatch with *luciferase* RNAi and 3 mM G418).

2.15 Low SAM associates with small nuclei and is rescued by SAM repletion

Formation of the ribonucleoprotein complex starts with the transcription and maturation of rRNAs, which takes place in the nucleolus of the cell. *C. elegans* has only one nucleolus per cell and its size is indicative of ribogenesis activity¹¹⁸. Since GO term analysis revealed decreased ribogenesis, I hypothesized that nucleoli in *pycr-1(wrm22)* mutants are smaller in size, and that this would be mimicked by ornithine and putrescine supplementation. I measured nucleolar and nuclear size in WT and *pycr-1(wrm22)* and found both to be smaller in *pycr-1(wrm22)* mutants (Figure 27a, b). It had previously been shown by Tiku et al. that small nucleoli in *C. elegans* are strongly correlated with longevity¹¹⁹. Moreover, since SAM is a key substrate for rRNA maturation, *pycr-1(wrm22)* rRNA levels are dysregulated and that methionine supplementation abolished its G418 resistance and normalized its lifespan, I hypothesized that SAM repletion by methionine supplementation would rescue small nucleoli. Encouragingly, methionine supplementation at least partially rescued small nuclei, but not nucleoli (Figure 27a, b). Interestingly, ornithine and putrescine supplementation both phenocopied *pycr-1(wrm22)* small nuclei, but not nucleoli (Figure 27c, d). Together, this suggests that metabolic processes in the nucleus, but not nucleolus, are downstream of SAM and correlate with G418 resistance and longevity in *pycr-1(wrm22)* mutants.

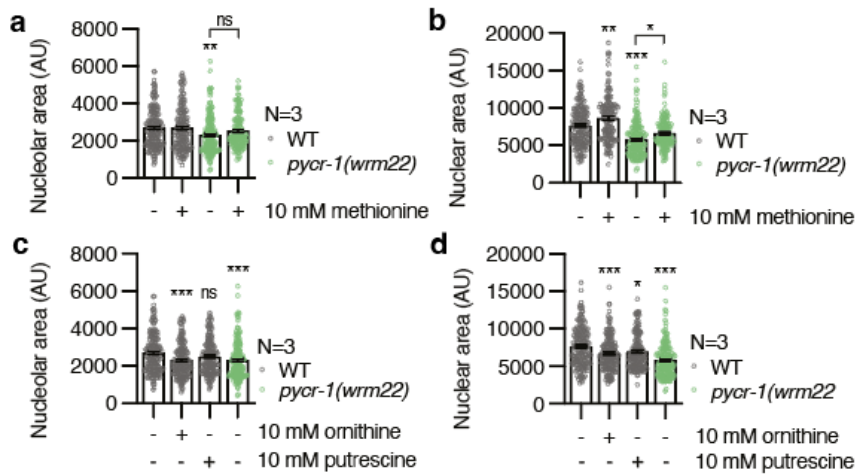


Figure 27: Low SAM associates with small nuclei and is rescued by SAM repletion

a, b, Nucleolar (**a**) and nuclear (**b**) size of seam cells of WT and *pycr-1(wrm22)* L3 larvae, treated from hatch with 10 mM methionine (error bars represent means \pm SEM, 2-way ANOVA multiple comparisons Tukey test, ns = not significant, * $p < 0.05$, ** $p < 0.01$, *** $p < 0.001$ vs untreated WT worms, unless indicated otherwise). **c, d,** Nucleolar (**c**) and nuclear (**d**) size of seam cells of WT and *pycr-1(wrm22)* L3 larvae, treated from hatch with 10 mM ornithine or putrescine (error bars represent means \pm SEM, 2-way ANOVA multiple comparisons Tukey test, ns = not significant, * $p < 0.05$, *** $p < 0.001$ vs untreated WT worms).

2.16 *pycr-1(wrm22)* transcriptional changes match with histone H3 markers

The small nuclei in *pycr-1(wrm22)* mutants indicate compact chromatin¹¹⁸. DNA in a loosely packed state is easily accessible to transcription factors, thus, an active state, and called euchromatin. In contrast, tightly packed DNA is largely inactive due to inability to bind transcription factors, and is called heterochromatin. Methylation and acetylation of DNA and histones modulates chromatin packing. However, whether *C. elegans* methylates its DNA is controversial^{120,121}. Instead, *C. elegans* depends on histone modifications to modify transcriptional activity. SAM serves as the sole histone methylation donor. Low SAM has been proposed to directly affect H3K4 methylation and is linked to ageing, but its mechanism remains elusive¹²². The rescue of small nuclei in *pycr-1(wrm22)* mutants by repleting SAM suggests that low SAM compacts chromatin by reduced histone methylation. Indeed, as shown by *pycr-1(wrm22)* RNAseq data, fewer mRNAs (2981) are significantly up- than downregulated (4529). To investigate whether transcriptional changes match with histone H3 markers, I intersected differentially expressed mRNAs with age-matched public ChIPseq data of histone H3 markers. Depending on the location of the lysine on the histone tail, its methylation can either be activating (H3K4, H3K23, H3K36 and H3K79) or repressing (H3K9 and H3K27) gene transcription^{123,124}. Surprisingly, transcriptional upregulation is associated with the absence of H3K4, H3K36 and H3K79 histone markers, and *vice versa*, transcriptional downregulation is associated with the presence of H3K4, H3K36 and H3K79 histone markers

(Table 1). This suggests that the epigenome is intimately linked to SAM level and potentially can be regulated by modulating its abundance.

a

H3K4	H3K9	H3K23	H3K27	H3K36	H3K79	
2172	647	23	226	2310	2310	Total counts
2054	265	12	168	2251	2251	Total matches
95	41	52	74	97	97	Match (%)

Table 1: *pycr-1(wrm22)* transcriptional changes match with histone H3 markers

a, Total counts: The number of gene bodies that were differentially expression in *pycr-1(wrm22)* transcriptome and associated with binding profiles of all public ChIP-seq data for H3K4, H3K9, H3K23, H3K27, H3K36 and H3K79 methylations from the ChIP-Atlas database^{125,126}. Total matches: The total number of gene bodies that matched, which was the case if the direction of the differential expression was in the same direction as is expected by loss of methylation of that histone marker. Match (%): The percentage of matches of the total counts for that histone marker.

Preliminary data showed that modulating H3K27 methylation affects G418 resistance of *pycr-1(wrm22)* mutants. I tested G418 resistance upon knockdown by RNAi of the H3K27 demethylases JMJD-3.1, JMJD-3.2 and UTX-1 and found that demethylation by JMJD-3.1 and UTX-1 are partially required for *pycr-1(wrm22)* G418 resistance (Figure 28a). Surprisingly, knockdown by RNAi of JMJD-3.2 improved G418 resistance (Figure 28a). Interestingly, similar counterintuitive results were reported for their contribution to lifespan, which was shown to be context-dependent¹²⁷. These promising preliminary data lead to testable hypotheses as to how histone H3 markers correlate with transcriptional changes of the entire transcriptome, and which transcriptional programs they activate to protect worms from G418 toxicity and extend lifespan. This I plan to investigate in future experiments.

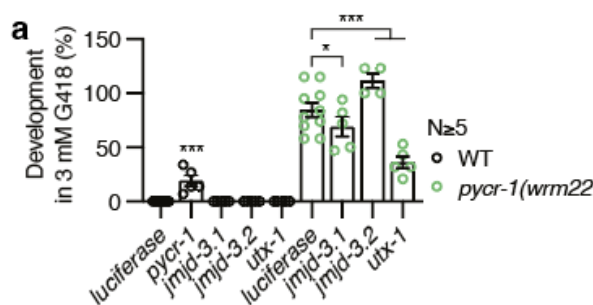


Figure 28: *pycr-1(wrm22)* G418 resistance can be modulated by H3K27 demethylases

a, Developmental G418 resistance assay of synchronized WT and *pycr-1(wrm22)* progeny of worms grown a full generation on target RNAi, treated from hatch with 3 mM G418 and target RNAi (error bars represent means \pm SEM, 2-way ANOVA multiple comparisons Tukey test, * $p < 0.05$, *** $p < 0.001$ vs worms treated from hatch with *luciferase* RNAi and 3 mM G418, unless indicated otherwise).

2.17 HSF-1 target genes confer G418 resistance and longevity in *pycr-1(wrm22)*

C. elegans ageing research has revealed distinct hallmarks of ageing under the control of master regulators that activate transcriptional programs to extend lifespan. This includes *atg-18* and *bec-1* (autophagy), *xbp-1* (endoplasmic reticulum (ER) stress signaling), *hsf-1* (heat shock response), *daf-16* (insulin signaling), *skn-1* (oxidative stress signaling) and *ncl-1* (ribogenesis)^{119,128–131}. To investigate their role in *pycr-1(wrm22)* longevity, I performed lifespan assays while knocking down these regulators by RNAi. As expected, RNAi against these master regulators reduced WT lifespan, and to a similar extent rescued *pycr-1(wrm22)* longevity (Supplementary table 1). The largest reduction (-50% mean lifespan) was achieved by *hsf-1* RNAi knockdown (Figure 29a). This indicates that *pycr-1(wrm22)* longevity is dependent on activation of a multitude of longevity pathways.

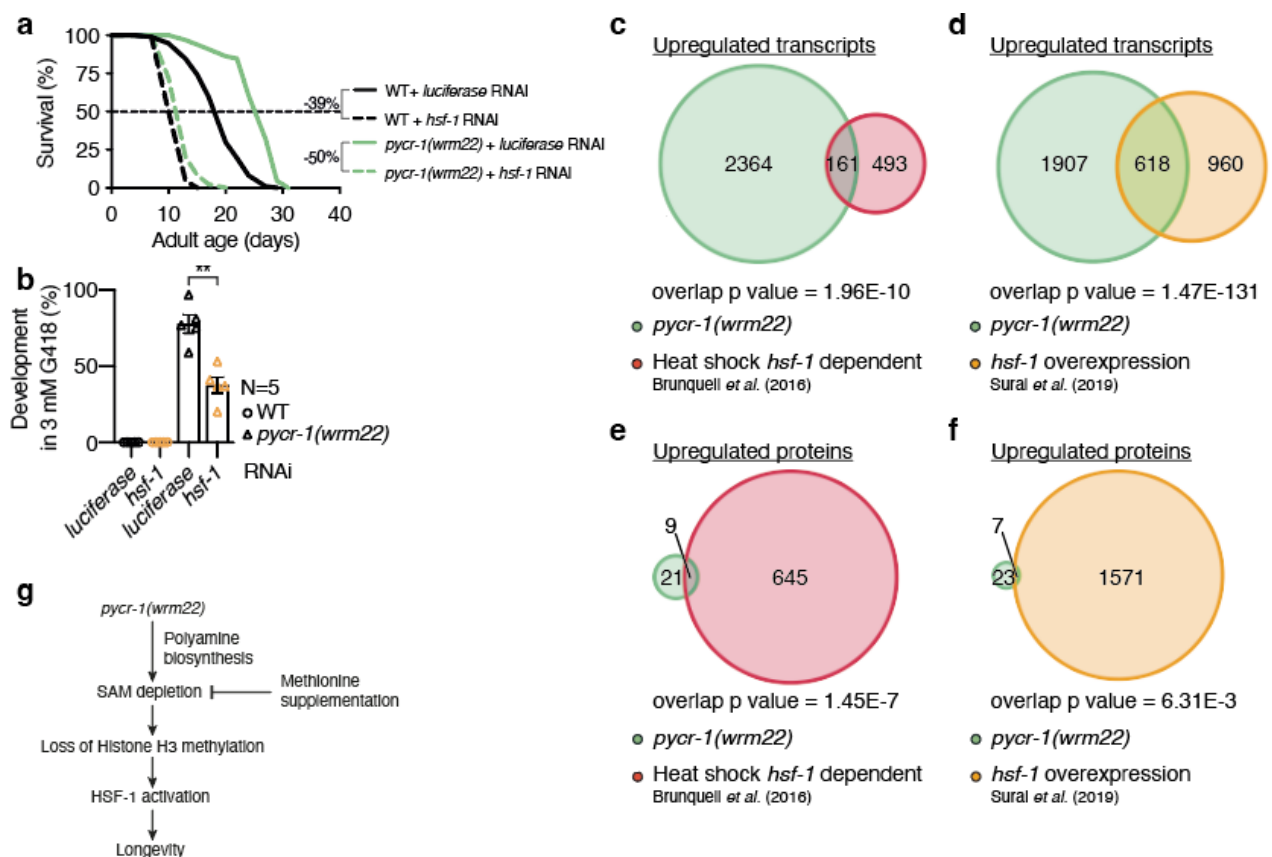


Figure 29: *hsf-1* target genes confer G418 resistance and longevity in *pycr-1(wrm22)*

a, Survival of WT and *pycr-1(wrm22)* mutants grown on *luciferase* RNAi and transferred to target RNAi at L4 stage. See Supplementary Table 1 for lifespan statistics. **b**, Developmental G418 resistance assay of synchronized WT and *pycr-1(wrm22)* progeny of worms grown a full generation on target RNAi, treated from hatch with 3 mM G418 and target RNAi (error bars represent means \pm SEM, 2-way ANOVA multiple comparisons Tukey test, ** $p < 0.01$). **c**, **d**, Venn diagrams showing overlap of upregulated mRNAs in *pycr-1(wrm22)* mutants with published datasets using HSF-1 activation^{50,114}. Hyper-geometric testing of overlap p value of upregulated transcripts of *pycr-1(wrm22)* and *hsf-1* dependent upregulated transcripts by heat shock (**c**) or upregulated transcripts by *hsf-1* overexpression (**d**). **e**, **f**, Venn diagrams showing overlap

of upregulated proteins in *pycr-1(wrm22)* mutants with published transcriptome datasets using HSF-1 activation. Hyper-geometric testing of overlap p value of upregulated proteins of *pycr-1(wrm22)* and *hsf-1* dependent upregulated transcripts by heat shock or upregulated transcripts by *hsf-1* overexpression (f). g, Working model for *pycr-1(wrm22)* longevity.

HSF-1 is a highly conserved transcription factor that induces target gene expression to maintain protein homeostasis in the presence of unassembled newly synthesized ribosomal proteins⁴⁸ or when protein homeostasis is challenged^{106,132,133}. Therefore, I hypothesized that activation of HSF-1 target gene expression might also confer G418 resistance in *pycr-1(wrm22)* mutants. To test this, I knocked down *hsf-1* mRNAs in *pycr-1(wrm22)* by RNAi and subjected the worms to G418. As expected, this sensitized *pycr-1(wrm22)* to G418 (Figure 29b). Together, this suggested that HSF-1 target gene expression is activated in *pycr-1(wrm22)* and plays a major role in its enhanced resistance to stressors, including stress induced by G418 toxicity and ageing.

To investigate whether transcriptional changes in *pycr-1(wrm22)* worms are regulated by HSF-1, I compared the transcriptome changes in *pycr-1(wrm22)* mutants with published data sets that used heat shock⁴⁹ or *hsf-1* overexpression⁵⁰ in *C. elegans*. I found a significant overlap between upregulated transcripts in *pycr-1(wrm22)* mutants and transcripts that are either upregulated by heat shock in a *hsf-1* dependent fashion (Figure 29c) or upregulated by *hsf-1* overexpression (Figure 29d). Similarly, proteome analyses of *pycr-1(wrm22)* mutants showed that a significant fraction of the upregulated proteins were *hsf-1* transcriptional targets (Figure 29e, f). Together, these data indicated that SAM depletion triggers HSF-1 target gene expression and extends *C. elegans* lifespan (Figure 29g).

2.18 SAM depletion is linked to HSF1 target gene expression in flies and mice

Longevity through dietary or methionine restriction is evolutionarily conserved and our data predict that these interventions deplete cellular SAM concentrations, eliciting an HSF-1-mediated transcriptional response to extend survival. In fruit flies (*Drosophila melanogaster*), an 80% dietary methionine restriction extended lifespan (Figure 30a). This treatment strongly depleted methionine and SAM, and interestingly also reduced SAH (Figure 30b, c, d). I matched RNA sequencing data of day 3 and day 7 old flies on methionine restriction with published HSF1 target genes¹³⁴ (Supplementary Table 2 of Gonsalves et al. 2011) and found a significant overlap at both time points (Figure 30e, f). Dietary restriction (DR) extends lifespan in many organisms, including mice and monkeys, however, the role for SAM in DR longevity

remains unclear^{66,135,136}. I therefore measured methionine, SAM, and SAH levels in the livers of DR and ad libitum (AL) fed mice aged two years. While methionine levels were increased (Figure 30g), I detected reduced SAM and unchanged SAH levels DR mice (Figure 30h, i). Liver transcriptomes of control AL and DR mice at 5 and 26 months of age¹³⁷ (publicly available under GSE92486) were analyzed for previously reported HSF1 target genes¹³⁸. Consistent with the data from worms and flies, I found significant HSF1 target gene regulation upon DR in the mouse (Figure 30j, k). Together, our data suggest that HSF1 responds to SAM depletion with transcriptional changes that extend lifespan, which is a conserved mechanism in flies and in mice.

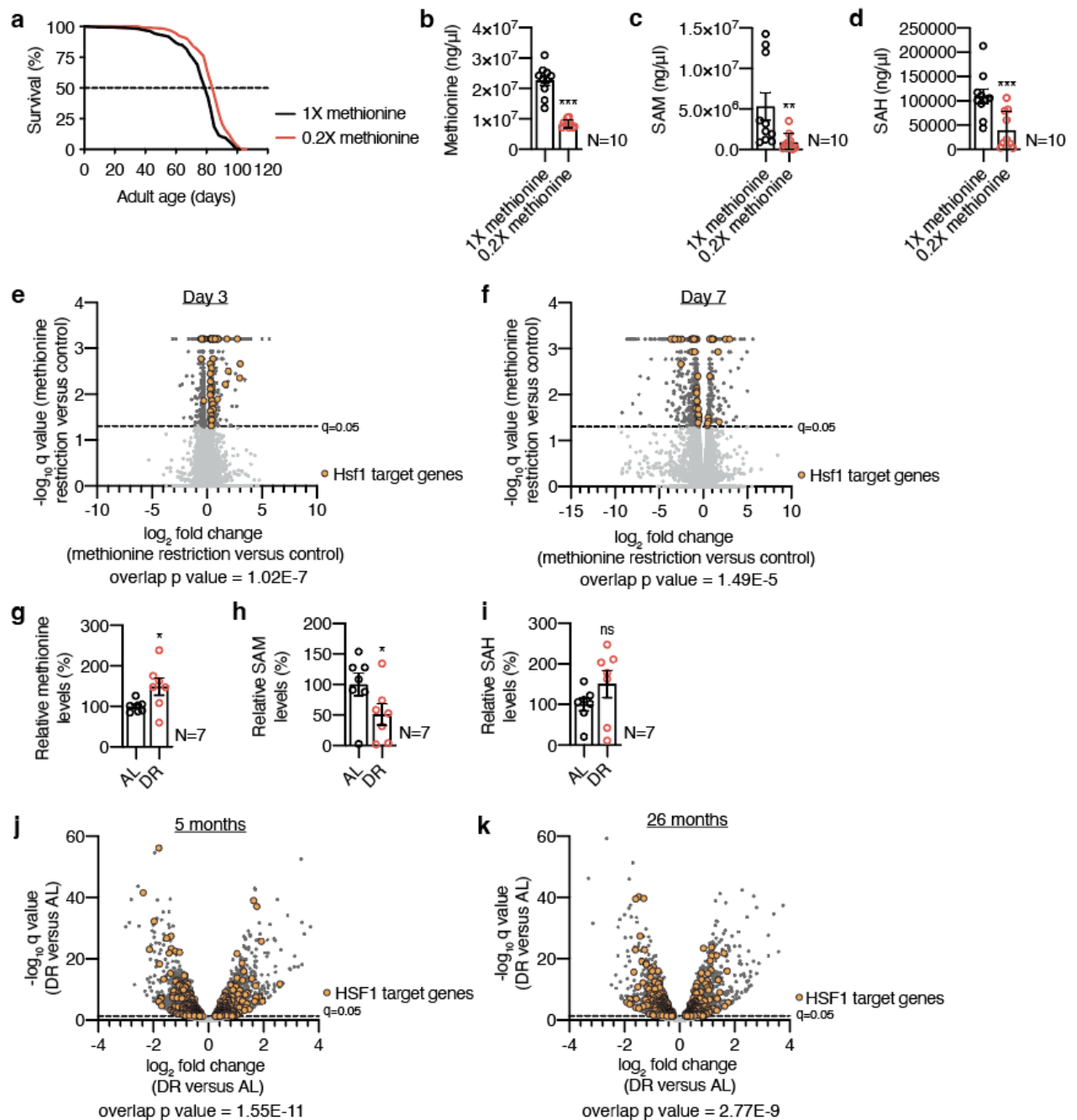


Figure 30: SAM depletion is linked to HSF1 target gene expression in longlived flies and mice

a, Fly survival on 1X and 0.2X methionine YAA diets, log-rank (Mantel-Cox) test $p < 0.0001$. See Supplementary Table 1 for lifespan statistics. **b, c, d**, Relative methionine (**b**), SAM (**c**) and SAH (**d**) levels of day 3 flies on 1X or 0.2X methionine YAA diets for 10 days, measured by LC-MS (error bars represent means \pm SEM, two-sided Student's t-test, $**p < 0.01$, $***p < 0.001$). **e, f**, Volcano plots showing overlap of differentially expressed mRNA transcripts in flies fed a diet lacking methionine for 3 (**e**) or 7 (**f**) days with a published dataset using Hsf1 activation. Hyper-geometric testing of overlap p value of differentially expressed transcripts of methionine restricted flies and Hsf1 target genes as previously published by Gonsalves et al. (Supplementary Table 2 of Gonsalves et al.¹³⁴). **g, h, i**, Relative methionine (**g**), SAM (**h**) and SAH (**i**) levels in livers of 24-month-old mice on ad libitum (AL) or 60% (DR) diets, measured by LC-MS (error bars represent means \pm SEM, two-sided Student's t-test, $*p < 0.05$). **j, k**, Volcano plots showing overlap of differentially expressed mRNA transcripts in livers of mice on DR versus AL for 5 (**j**) or 26 (**k**) months with a published dataset using HSF1 activation. Hyper-geometric testing of overlap p value of differentially expressed transcripts of mice on DR versus AL and HSF1 target genes as previously published by Hahn et al.¹³⁷, publicly available under GSE92486, and Kovács et al.¹³⁸.

3 Discussion

In this study, I delineate the metabolic control of the *de novo* proline biosynthesis pathway using a novel long-lived *pyrroline-5-carboxylate reductase 1* mutant *pycr-1(wrm22)*, which catalyzes the final step to synthesize proline. I focused my analyses on protein synthesis, ribosome biogenesis and stress response pathways, since all three contribute to protein homeostasis and become dysregulated during ageing. Moreover, *pycr-1(wrm2)* was found using a proxy screen to select for EMS mutagenized mutants that are resistant to a wildtype (WT) lethal concentration of the aminoglycoside geneticin (G418). G418 impairs ribosomal function and induces synthesis of mistranslated proteins, strain protein homeostasis. To study resistance to toxic levels of G418, I made use of developmental assays in liquid cultures, which allowed for easy setup and manipulation of variable growth conditions and testing of a high number of conditions in parallel. First, I confirmed that G418 resistant mutants could be generated using EMS mutagenesis. Using G418 resistance as a proxy, resulted in an enrichment of long-lived mutants. I selected the most long-lived mutant for further characterization. Second, I identified *pycr-1(wrm22)* as a loss-of-function mutant of *de novo* proline biosynthesis, and analyzed its metabolome, transcriptome, translatome and proteome. This revealed that impaired proline biosynthesis depletes S-adenosyl methionine (SAM) through increased polyamine biosynthesis. Third, I elucidated stress responses that were potentially regulated by SAM, and specifically focused on ribogenesis, because of the striking resistance of *pycr-1(wrm22)* to G418 toxicity, which directly impairs ribosomal function. Interestingly, ribogenesis was dysregulated on a transcriptional and translational level, which associated with altered pre-rRNA and rRNA levels, and reduced expression of ribosomal proteins. Perturbed ribogenesis has been implicated with heat shock factor 1 (HSF-1) target gene expression, which suggested a hormetic ribosomal assembly stress response in *pycr-1(wrm22)* mutants that promotes stress resilience and longevity. Strikingly, transcriptional changes of *pycr-1(wrm22)* mutants strongly associate with the presence of histone modifications in WT worms. This observation provides a plausible alternative mode-of-action by which low SAM modulates gene transcription and regulates HSF-1 target gene expression. Remarkably, I identified that low SAM induced by impaired *de novo* proline biosynthesis is a shared characteristic with polyamine supplementation regimes, as well as dietary and methionine restriction. Intriguingly, all three have been shown in various model organisms to extend lifespan. Finally, I showed that low SAM in the worm, fly and mouse associates with HSF-1 target gene expression and is a potential conserved key regulator of ageing.

3.1 G418 resistance screen enriches for novel long-lived mutants

The forward genetics screen I performed for resistance to G418 toxicity generated 16 G418-resistant mutants, by screening 1,250,000 genomes. Intriguingly, 7 out of 16 mutants had a median and mean lifespan extension of at least 15% (Figure 13b). A forward genetics screen for resistance to tunicamycin (TM) toxicity, performed by Martin Denzel and Nadia Storm published in *Cell* in 2014, generated 358 TM-resistant mutant strains, by screening 200,000 genomes⁴³. Of those, 109 had a median lifespan extension of over 15%. Compared to the TM-resistance screen, resistance to G418 toxicity by EMS is extremely rare. Moreover, using G418 toxicity as a proxy enriched more strongly than TM for longevity, 44% against 30% had an extended lifespan of at least 15%, respectively.

This thesis highlights the discoveries I made from characterizing the most long-lived mutant of the forward genetics G418-resistance screen I performed, *pycr-1(wrm22)*. However, 15 other uncharacterized mutants from the screen remain uncharacterized. In the future, these mutants will be characterized to elucidate whether the mechanisms by which they attain G418 resistance is similar to the mechanism in *pycr-1* mutants. Since G418 resistance is rare, it is possible that the mutants have partially overlapping resistance-mechanisms, but their analysis might still uncover novel routes to G418 resistance. It would be interesting to characterize both long-lived and short-lived mutants: Long-lived mutants are interesting, because they can teach us more about protective mechanisms that are also protective against ageing; Short-lived mutants are interesting, since they could tell us about potential otherwise overlooked mechanisms that are protective against G418 toxicity, but whose activation is detrimental for the ageing process. Alternatively, short-lived mutants could potentially reveal hormetic effects, where a low activation is beneficial for an organism, but a high activation is detrimental.

3.2 The SNP in *pycr-1* is the causal mutation of the *wrm22* allele

Identification of the single nucleotide polymorphism (SNP) in the gene *pycr-1* as the causal mutation of the *wrm22* allele was straightforward. First, I performed Hawaiian SNP mapping by outcrossing the mutant strain to the Hawaiian WT variant, while simultaneously selecting for G418 resistance, which I could do because the *wrm22* allele is dominant. Whole genome sequencing of a pool of a few dozen independent outcrossed lines provided linkage scores of loci that were enriched by selecting for G418 resistance. The highest linkage scores were found in the 9 to 14 Mb region of the X chromosome and provided a shortlist of 6 candidate genes

that had a SNP in the coding sequence (Figure 14b). The causal SNP could be either a loss-of-function or gain-of-function mutation, and, in case of the former, I hypothesized that RNAi of the causal gene would phenocopy the loss-of-function mutation for G418 resistance. Indeed, the knockdown of PYCR-1 by RNAi phenocopied G418 resistance of the EMS mutant we now termed *pycr-1(wrm22)*. I further validated the SNP in *pycr-1* as causal for G418 resistance with two CRISPR lines that were generated by SunyBiotech: a knockout of *pycr-1* and a point mutant of *pycr-1* with the same SNP that is found in the *wrm22* allele. Both CRISPR lines were strongly resistant to G418, thereby confirming the SNP in *pycr-1(wrm22)* as causative loss-of-function mutation.

3.3 Dimerization of PYCR-1 is possibly perturbed in *pycr-1(wrm22)*

The *pycr-1(wrm22)* SNP is positioned at the two-fold symmetry line of the PYCR-1 dimer (Figure 15b). Although that the altered amino acids are positioned in close proximity, they are not predicted to sterically interfere. However, the dimer forms by interlocking of two PYCR-1 monomers. For human PYCR1, the catalytic pocket requires dimerization¹³⁹. This is likely also the case for worm PYCR-1, due to the conserved secondary structure of PYCR-1 (Figure 15c). The WT G246 is part of a glycine loop with G245 that allows for flexible movement¹⁴⁰. The glycine loop is lost by G246E substitution, which potentially impairs dimerization, and thus catalytic activity, of PYCR-1. To test this hypothesis, I propose analytical size-exclusion chromatography measurements of PYCR-1(*wrm22*) proteins. In *pycr-1(wrm22)* mutants I expect to detect only monomers.

3.4 Impaired *de novo* proline biosynthesis indirectly depletes SAM

Abundance of the amino acid proline was found to be reduced by 28% in *pycr-1(wrm22)* mutants. Total RNAseq data of *pycr-1(wrm22)* revealed that proline biosynthesis pathway genes are upregulated. *Aldehyde dehydrogenase 13 (alh-13)*, which catalyzes the reaction to produce glutamate 5-semialdehyde (G-5-S) from glutamate, and *pycr-1* mRNAs are upregulated. This supports a compensatory mechanism of upregulation of *de novo* proline biosynthesis enzymes in a response to low proline. I hypothesized that a low proline level could be causal for *pycr-1(wrm22)* G418 resistance, surprisingly however, supplementation of proline to the food did not rescue *pycr-1* G418 resistance (Figure 17a). The proline synthesis and polyamine pathways are linked through the intermediate G-5-S (Figure 21a), which is expected to accumulate in the *pycr-1* mutant, as indicated by elevated ALH-13 expression. G-5-S is in a dynamic equilibrium with pyrroline-5-carboxylate (P-5-C)¹⁴¹, whose accumulation

is toxic^{142,143}. As a precursor to ornithine, G-5-S elevation plausibly increases metabolite flux in the polyamine pathway. Unfortunately, both P-5-C and G-5-S are very unstable and elude direct measurements. To find out which metabolic change was causal for *pycr-1(wrm22)* G418 resistance, I analyzed the metabolite levels of all the proteogenic amino acids and metabolites of the *de novo* polyamine biosynthesis pathway. I found an increase of N-acetyl-putrescine and spermidine in the polyamine pathway, and remarkably a reduced level of S-adenosylmethionine (SAM), which is a substrate for polyamine biosynthesis. This suggested that either increased polyamine levels or low SAM levels could be causal for *pycr-1(wrm22)* phenotypes.

To test this, I supplemented WT worms with the polyamine spermidine, and also with its precursors ornithine and putrescine (Figure 21a). Surprisingly, WT worms treated with ornithine or putrescine, but not spermidine, phenocopied SAM depletion and G418 resistance observed in *pycr-1(wrm22)* (Figure 21g-i). To test whether SAM depletion was causal, I repleted SAM by feeding *pycr-1(wrm22)* mutants with methionine, from which SAM is synthesized^{144,145}. Indeed, SAM repletion abolished *pycr-1* G418 resistance (Figure 22b). Moreover, I confirmed that SAM repletion in WT worms treated with ornithine and methionine were significantly less resistant to G418 than WT worms treated with ornithine alone (Figure 22c). I therefore conclude that *pycr-1* loss-of-function shifts metabolite flux in these interconnected pathways towards polyamine biosynthesis, which then depletes SAM, resulting in G418 resistance.

3.5 Improved stress resilience of *pycr-1(wrm22)*

The aminoglycoside G418 impairs cellular activity threefold: it inhibits translation, induces misreading of mRNAs and is a weak non-competitive inhibitor of ornithine decarboxylase^{37,146}. G418 toxicity is believed to be due to the production of misread, abnormal proteins^{101,147}. Indeed, low translation is associated with longevity, whereas expression of aberrant proteins is toxic and shortens lifespan^{26,41}. My data shows that *pycr-1(wrm22)* mutants were similarly sensitive to protein synthesis inhibition by G418 as WT worms, suggesting that the amount of mistranslated proteins upon G418 treatment is comparable. However, *pycr-1* mutants had increased HSF-1 target gene expression in non-stressed conditions. Activation of HSF-1 target gene expression is implicated with improved stress resistance and lifespan extension^{50,106,148}. HSF-1 target genes include chaperones that help refold misfolded proteins and resolubilize aggregated proteins. This indicates that *pycr-1* mutants have an increased capacity to respond

to insults of the protein homeostasis network due to an elevated protein folding capacity. Consistently, *pycr-1(wrm22)* animals are resistant to different classes of protein synthesis inhibitors that perturb a variety of translation steps, including aminoacyl-tRNA selection and accommodation, peptide-bond formation, mRNA-tRNA translocation, and termination³⁷. Furthermore, *pycr-1* mutants showed improved resilience against heat shock and oxidative stress. Both heat shock and oxidative stress resistance are regulated by heat shock proteins, which are upregulated upon HSF-1 activation¹⁴⁹. Interestingly, the PYCR-1 loss-of-function impairs proline cycling, which might result in reduced reactive oxygen species (ROS) generation⁸⁶. Therefore, *pycr-1* mutants are likely to have improved ROS scavenging capacity. Of note, low ROS is associated with cell survival and lifespan extension¹⁵⁰. This suggests that *pycr-1* mutants attain improved resilience by activating HSF-1 target gene expression. Indeed, my data shows that HSF-1 activity is required for *pycr-1* G418 resistance and longevity.

3.6 *pycr-1(wrm22)* phenocopies key aspects of methionine and dietary restriction

The drastic reduction of SAM by 75% in *pycr-1(wrm22)* mutants is similar to the 72% drop of SAM reported in metformin treated worms that are long-lived⁷⁴. Interestingly, metformin does not further extend the lifespan of the long-lived *sams-1(ok3033)* mutant, suggesting that SAM reduction is the key event in metformin longevity in *C. elegans*. In dietary restricted *eat-2(ad1116)* *C. elegans* mutants, *sams-1* mRNA is reduced threefold and knockdown of *sams-1* does not further extend lifespan of dietary restricted worms, likewise suggesting a key role of SAM levels in this longevity paradigm¹¹⁰. Similarly, *sams-5* expression is reduced in *eat-2(ad1116)* mutants, and its overexpression partially suppresses *eat-2(ad1116)* longevity¹⁴⁵. Methionine is an essential amino acid and the substrate for SAM synthases. In flies, mice, and rats dietary methionine restriction is a well characterized modulator of health- and lifespan^{151–153}. Interestingly, the transcriptional response to methionine deprivation was shown to depend on reduced SAM levels¹⁰⁸. Together, these data suggest that low SAM is a pivotal feature in longevity across species. The *pycr-1* mutation identified in this study thus phenocopies key aspects of methionine restriction.

3.7 Does mTORC1 signaling play a role in *pycr-1(wrm22)*?

Nutrient sensing by mammalian target of rapamycin complex 1 (mTORC1) regulates cell growth and organismal ageing by controlling protein synthesis^{154,155}. Active phosphorylated mammalian target of rapamycin (p-mTOR) increases ribosomal elongation speed, with a trade-off for translation fidelity. Conversely, inhibition of mTORC1 by rapamycin slows down

protein synthesis and improves the quality of protein synthesis. Interestingly, PYCR1 inhibition was recently shown to reduce multiple myeloma (MM) viability and proliferation, and to induce apoptosis, by reducing p-mTOR protein level¹⁵⁶. Moreover, PYCR1 knockdown has been shown to reduce p-mTOR level in renal cell carcinoma¹⁵⁷. As expected, in both studies this resulted in decreased protein synthesis^{156,157}. In contrast to reduced protein synthesis observed in MM cells upon PYCR1 silencing in cancer cells, PYCR-1 loss-of-function in *pycr-1(wrm22)* mutants was not associated with reduced protein synthesis. However, cancer cells have elevated protein synthesis rates, which might explain why such an effect is not seen in *pycr-1(wrm22)* mutants.

Moreover, inactive mTOR is associated with induced autophagy in mammalian cells¹⁵⁸. Similarly, a *C. elegans s-adenosyl methionine synthase 1 (sams-1)* deletion mutant showed reduced SAM level and increased autophagy¹⁵⁹. However, autophagy genes were significantly downregulated in the *pycr-1(wrm22)* transcriptome. These results show that PYCR1 inhibition or silencing in cells does not exhibit a similar response as with PYCR-1 loss-of-function in worms. This is supported by the surprising lack of any effect of *pycr-1* RNAi on lifespan of WT worms (data not shown). However, *pycr-1* RNAi induces G418 resistance in WT worms, and therefore, could be helpful to dissect resistance mechanisms from those extending lifespan. Together, the lack of conserved cellular responses between PYCR1 silencing on the one hand, and PYCR-1 loss-of-function on the other, indicate that PYCR-1 loss-of-function in *pycr-1(wrm22)* mutants promotes healthy ageing through a hormetic response.

3.8 Does the integrated stress response play a role in *pycr-1(wrm22)*?

The endoplasmic reticulum (ER) unfolded protein response (UPR^{ER}) can activate the integrated stress response (ISR), as a result of phosphorylation of its master regulator eukaryotic initiation factor 2 α (eIF2 α) by the ER kinase PERK¹⁶⁰. Additionally, amino acid shortage and mitochondrial stress trigger general control non-derepressible 2 (GCN-2) kinase signaling via eIF2 α ⁷². The reduced amino acid levels (Figure 21b) and the mild mitochondrial stress (Figure 24a, b) in *pycr-1(wrm22)* mutants might similarly trigger GCN-2 kinase signaling. Phosphorylated eIF2 α inhibits protein synthesis and activates an ATF-4-dependent transcriptional response¹⁶¹. The mammalian homologue ATF4 activates gene transcription of genes involved in oxidative stress and amino acid metabolism¹⁶⁰. Unfortunately, the transcriptional response triggered by *C. elegans* ATF-4 is not fully described. It would be interesting to investigate if ATF-4 target genes overlap with altered gene transcription in

pycr-1(wrm22) mutants, which would indicate that the ISR might play an important role. In *pycr-1(wrm22)* activation of UPR^{ER} or amino acid shortage could potentially trigger the ISR, however, SAM depletion has not been implicated in ISR activation. Furthermore, inhibition of the ISR and not its activation has been shown to extend lifespan previously¹⁶². Thus, the ISR is unlikely to play a key role in *pycr-1(wrm22)* stress response and its effects on ageing.

3.9 Does low SAM trigger a ribosome mediated hormetic stress response?

SAM-dependent methylation reactions have previously been linked to longevity, particularly in the context of histone modifications^{76,163}. SAM is also an important substrate for rRNA maturation and plays key roles in mRNA translation¹⁶⁴. In *pycr-1* mutants, rRNA methylation levels might be affected due to reduced substrate availability, leading to ribogenesis defects. My findings suggest a plausible link for the role of SAM in longevity with a ribosome mediated hormetic stress response I termed ribohormesis. This is supported by multiple lines of evidence. First, transcriptome analysis revealed a downregulation of mRNAs involved in ribogenesis in *pycr-1* mutants. Apparently, this was a mild change as, judged from polysome profiles, overall translation was not affected. Second, rRNA abundance was found to be dysregulated, which is relevant given the high abundance of rRNAs (Figure 26c, d). Third, transcriptome analysis of *pycr-1* mutants (Figure 29c, d), as well as lifespan analysis of *pycr-1(wrm22)* mutants treated with *hsf-1* RNAi (Figure 29a), indicated HSF-1 activation that was required for the longevity phenotype. Recent data from yeast describe a ribosome assembly stress response that occurs when ribosomal protein biogenesis is perturbed⁵⁶. This in turn activates Hsf1 target gene transcription. Our findings suggest a similar role of metazoan ribogenesis as a sensor of adverse metabolic conditions. Ribogenesis defects subsequently triggers a stress response involving HSF-1. Our data significantly extend this notion and demonstrate that availability of the metabolite SAM is a physiological upstream modulator of ribogenesis. SAM depletion elicited the HSF-1 stress response, which might be triggered by altered ribogenesis. Which effect by low SAM on ribogenesis triggers the plausible ribosome mediated hormetic response is currently unknown. SAM depletion did not rescue increased NRDE-3 nuclear localization (Figure 26i) or nucleolar size (Figure 27a), and RNAi of rRNA methylases failed to phenocopy *pycr-1(wrm22)*, but a plausible rescue of altered rRNA or ribosomal protein levels have not yet been investigated. Together, my observations suggest a potential link between SAM levels and a ribosomal stress response via HSF-1 in longevity mediated by methionine restriction.

3.10 Which alternative mechanisms could link SAM depletion to longevity?

How methionine restriction extends lifespan has been a longstanding open question¹⁵³ and I propose an explanation through a hormetic stress response triggered by low SAM. The low SAM level in *pycr-1* animals, about 25% compared to wildtype worms, is likely hormetic, because SAM is an essential methyl donor for vital cellular processes^{76,165,166}. The lifespan-extending compound metformin likewise depletes SAM⁷⁴. Importantly, DR in mice lowered SAM levels and was associated with HSF target gene expression, also shown in methionine restricted flies. HSF-1 overexpression in worms *per se* is sufficient for lifespan extension¹³². HSF1 activation as a consequence of SAM depletion is thus a conserved feature in longevity across distinct taxa. SAM depletion is thought to induce longevity in *pycr-1(wrm22)* by modifying gene expression by reduced histone methylation. I have excluded several mechanisms, which have been proposed by Parkhitko et al.⁷³, by which low SAM potentially improves health and lifespan. First, *pycr-1* mutants did not show reduced translation as shown by puromycin incorporation and ribosome profiling assays (Figures 18a-c). Second, transcriptome and translome analysis did not indicate improved autophagy, but instead showed a downregulation of autophagy gene transcription and translation. Third, induced mitochondrial stress, as shown by the mitochondrial UPR (mitoUPR) reporter HSP-6::GFP, indicated perturbation of mitochondria. Although perturbed mitochondrial function can extend lifespan, SAM repletion by methionine was unable to rescue the mitochondrial stress response, indicating that mitoUPR and longevity are uncoupled in *pycr-1* mutants. Finally, resilience to oxidative stress was improved in *pycr-1(wrm22)*, but SKN-1, which mediates oxidative stress resistance¹⁶⁷, was shown to be only partially required for *pycr-1* longevity (Supplementary Table 1). Moreover, Parkhitko et al. proposed SAM depletion could modulate gene transcription by reduced methylation of histone markers, which they based on studies showing association of high SAM to S-adenosyl-homocysteine (SAH) ratio with increased tri-methylation of H3K4, H3K36 and H3K79, and the modulation of lifespan by histone methylase and demethylase mutants⁷³. Interestingly, *pycr-1* mutants show significant SAM depletion, which strongly associates with transcriptional changes in *pycr-1(wrm22)* in the context of histone markers, as they are found in WT worms. It will be interesting to investigate the methylation status of histone markers in *pycr-1(wrm22)* and how this is linked to HSF-1 target gene expression. A plausible mechanism by which low SAM is sensed and regulates histone methylation is the protein phosphatase PP2A. In yeast, PP2A is demethylated in response to methionine restriction¹⁶⁸. This allows PP2A to phosphorylate histone demethylases which become activated. As a result, H3K4, H3K36 and H3K79 tri-methylation is decreased. PP2A

is a heterotrimer composed of scaffolding subunits, a single catalytic subunit and one of several possible regulatory subunits, which are conserved in *C. elegans*¹⁶⁹. It will be highly interesting to investigate if PP2A plays a significant role in relaying signaling of low SAM to modulate histone methylation, which in turn mediates HSF-1 target gene expression and promotes longevity in *pycr-1(wrm22)*.

3.11 Therapeutic potential of PYCR1 inhibition

Mutations in human PYCR1 have been linked to De Barsy syndrome, which is a rare autosomal recessive disease that is classified as a form of cutis laxa with progeroid features¹⁷⁰. Moreover, PYCR1 is highly expressed in various cancers and its suppression can significantly inhibit cell growth and malignancy^{100,157,171,172}. While this implicates PYCR1 in human lifespan, it remains unknown whether the human proline pathway might affect the methionine cycle. I expect that means of lowering SAM in humans might elicit the hormetic stress response I observed in the nematode, fly and mouse. In the future, reducing SAM or inhibiting PYCR1 in a targeted manner might be an effective therapeutic approach to tackle progeroid syndromes and age-associated diseases to promote a healthy lifespan in humans.

Interestingly, PYCR1 inhibitors have recently been developed for their potential anti-tumorigenic effects^{84,87}, and according to my data, they additionally have a potential for general benefits for healthy ageing. Interestingly, low SAM is both a characteristic of PYCR-1 loss-of-function, and dietary and methionine restriction, therefore, it will be interesting to test whether PYCR1 inhibition could be a novel route to deplete SAM in humans, and could serve as a dietary restriction mimic to promote healthy ageing.

4 Materials & Methods

4.1 *C. elegans* strains and culture

All *C. elegans* strains were maintained at 20°C on nematode growth medium (NGM) agar plates seeded with the *Escherichia coli* (*E. coli*) strain OP50, unless indicated otherwise²². To provide an isogenic background in all mutant strains, they were outcrossed against the wild type (WT) Bristol N2 strain. All strains used in this study are listed in Supplementary Table 3. Genotyping primers used in this study are listed in Supplementary Table 5.

4.2 Unbiased forward genetics G418 developmental resistance screen

The G418 developmental resistance screen was performed with the wild type Bristol N2 strain. L4 larvae were exposed to 0.2% ethyl methane sulfonate (EMS, Sigma-Aldrich) in M9 buffer for 4h at room temperature. After recovery overnight, young P0 adult animals were transferred to new plates. Gravid F1 progeny were bleached to obtain synchronized F2 eggs. F2 worms were treated in liquid culture, containing S-basal media and OP50, with 1 mM G418 and allowed to develop to adults for 5 days on a nutator shaker at 20°C. Independent mutants that were G418 resistant were selected for lifespan analysis and the mutant with the largest lifespan extension was selected for Hawaiian outcrossing and whole genome sequencing.

4.3 Mutant Hawaiian SNP mapping and sequence analysis

Genomic DNA was prepared using the QIAGEN Gentra Puregene Kit. Whole genome sequencing was conducted on the Illumina HiSeq2000 platform. Paired-end 100 bp reads were used; the average coverage was larger than 16-fold. Sequencing outputs were analyzed using the CloudMap Hawaiian and Variant Discovery Mapping on Hawaiian Mapped Samples (and Variant Calling) Workflow_2-7-2014 pipeline on Galaxy^{94,96}. The WS220/ce10 *C. elegans* assembly was used as reference genome.

4.4 Protein sequence alignment

Protein sequence alignments were created with UniProt IDs: *Caenorhabditis elegans* Q21544, and *Homo sapiens* P32322. The alignment of *C. elegans* PYCR-1 and *H. sapiens* PYCR1 was formatted with the ESPrpt3 server (esprpt.ibcp.fr/)¹⁷³.

4.5 Protein structures

The structure of human PYCR1 was taken from Protein Data Base (PDB ID: 5UAV). The protein sequence for *C. elegans* PYCR-1 and PYCR-1(*wrm22*) was created with UniProt ID: *Caenorhabditis elegans* Q21544. AlphaFold¹⁷⁴ was run on the online Flaski platform¹⁷⁵.

4.5 Lifespan assays

Synchronized populations used in lifespan assays were obtained by 3h egg-lay by gravid adults. The L4 stage was defined as day 0. Worms were kept at 20°C on NGM plates seeded with live OP50 *E. coli* bacteria at all times, except for RNAi lifespan assays or methionine supplementation lifespan assays. Animals in all RNAi lifespan assays were grown on NGM plates seeded HT115 *E. coli* expressing *luciferase* RNAi from hatch on and moved to target RNAi at L4 stage. Animals in all methionine supplementation lifespan assays were grown from hatch on NGM plates containing the indicated concentration of L-methionine (Sigma-Aldrich) seeded with dead OP50 (derived by three cycles of snap freezing and thawing). The animals were transferred every second day to fresh plates until they reached the post-reproductive stage. Scoring was performed generally every second day by monitoring (touch-provoked) movement and pharyngeal pumping. In all lifespan experiments, worms that had undergone internal hatching, vulval bursting, or worms crawling off the plates were censored. Throughout the experiment, strain and/or treatment were unknown to researchers. Data were assembled on completion of the experiment. Statistical analyses were performed with the Mantel-Cox log rank method in Prism (Version 8.2.0).

4.6 RNAi experiments

For RNAi mediated knockdown of specific genes, HT115 *E. coli* carrying vectors for dsRNA of the target gene under a promotor inducible by isopropyl β -D-1-thiogalactopyranoside (IPTG) and an ampicillin resistance cassette were used. RNAi expression was induced by treatment with 1 mM IPTG (Roth) in the presence of 100 μ g/ μ L ampicillin (Merck Millipore). RNAi against *luciferase* was used as nontargeting control. All RNAi clones were obtained from Ahringer and Vidal RNAi libraries, kindly provided by Adam Antebi^{176,177}. Clones were validated by plasmid purification (QIAprep Spin Miniprep Kit, Qiagen) and sequencing using the L4440 Reverse primer. All bacterial RNAi strains used in this study are listed in Supplementary Table 4, including source. Genotyping primers used in this study are listed in Supplementary Table 5.

4.7 Developmental G418 resistance assays

Synchronized eggs were obtained by bleaching gravid adults. Roughly 25 eggs were transferred by pipetting to 2 mL tubes containing 500 μ L liquid culture consisting of S-basal, 1 mM Geneticin (G418) (AppliChem) and a 1.5-fold concentrate of freeze-killed OP50 *E. coli*. Concentrated freeze-killed OP50 bacteria was obtained by three cycles of snap-freezing and thawing pelleted overnight OP50 bacterial cultures. For G418 developmental assays with methionine, ornithine or proline supplementation, eggs were obtained by bleaching gravid worms that were grown on NGM plates containing the indicated concentration of the amino acid (AA). Additionally, the AAs were added to the liquid culture at the indicated concentration. For G418 developmental assays with RNA knockdown live HT115 bacteria expressing target RNAi were used instead of freeze-killed OP50. RNAi expression of overnight HT115 bacterial cultures grown in LB media with 100 μ g/ μ L ampicillin (Merck Millipore) were induced for three hours with 1 mM IPTG at 37°C. The bacteria were pelleted and resuspended in S-basal containing 100 μ g/ μ L ampicillin (Merck Millipore), 1 mM IPTG (Roth) and 3 mM Geneticin (G418) (AppliChem). F1 animals for RNA knockdown assays were obtained by bleaching gravid P0 that were grown on NGM plates containing 100 μ g/ μ L ampicillin (Merck Millipore) and 1 mM IPTG (Roth) and seeded with HT115 bacteria expressing target RNAi. RNAi against *luciferase* was used as nontargeting control. For all G418 developmental assays, worms were kept in the tubes for 4 to 5 days on a nutator mixer at 20°C, after which adult worms were scored. Throughout the experiment, strain and/or treatment were unknown to researchers. Data were assembled on completion of the experiment. At least 3 independent experiments were performed. Error bars represent means \pm SEM and statistical significance was calculated with two-sided Student's t-test or 2-way ANOVA multiple comparisons Tukey test.

4.8 Developmental paraquat resistance assays

Synchronized L4 stage worms were transferred to NGM plates containing 200 mM methyl viologen (paraquat) (AppliChem) seeded with freeze-killed OP50 *E. coli*. Freeze-killed OP50 bacteria was obtained by three cycles of snap-freezing and thawing pelleted overnight OP50 bacterial cultures. Worms were kept at 20°C and scored every hour by monitoring (touch-provoked) movement and pharyngeal pumping. Throughout the experiment, strain identity was unknown to researchers. Data were assembled on completion of the experiment. Three independent experiments were performed. Error bars represent means \pm SEM and statistical significance was calculated with the Mantel-Cox log-rank test.

4.9 Heat stress survival assays

Worms were synchronized by egg-lay and allowed to develop to day 1 adulthood on NGM plates seeded with OP50 *E. coli* at 20°C, when the plates were transferred to a 35°C incubator. The worms were scored live or dead by touch-provoking every 2h. Three independent experiments were performed with at least 20 worms per experimental condition. Throughout the experiment, strain identity was unknown to researchers. Data were assembled on completion of the experiment. Error bars represent means \pm SEM and statistical significance was calculated with two-sided Student's t-test.

4.10 Generation time

Worms were synchronized by a 1h egg-lay, which counts as time-point 0. The worms were allowed to develop to adulthood and the generation time is defined as the time it took them to lay the first egg. After 64h, worms were scored every 2h with at least 24 worms analyzed per genotype. Throughout the experiment, strain identity was unknown to researchers. Data were assembled on completion of the experiment. Error bars represent means \pm SEM and statistical significance was calculated with two-sided Student's t-test.

4.11 Brood size assay

Worms were synchronized by a 1h egg-lay and L4 worms were placed on individual NGM plates seeded with OP50 bacteria. Worms were transferred to fresh plates every 24h until no more eggs were laid. The number of viable progeny on each plate was counted in 24h bins. Per genotype at least 10 worms were counted for each time point. Throughout the experiment, strain identity was unknown to researchers. Data were assembled on completion of the experiment. Error bars represent means \pm SEM and statistical significance was calculated with two-sided Student's t-test.

4.12 Metabolite analysis sample preparation

For worm samples: Per replicate approximately 500 synchronized day 1 adult worms grown on NGM plates seeded with OP50 were collected in 15 mL tubes by washing them off with M9. For assays with methionine, ornithine or proline supplementation, before collection, worms were transferred to 5 mL tubes in 1.25 mL liquid culture containing dead OP50 obtained by three freeze-thaw cycles and the amino acid supplemented at the indicated concentration in S-basal. The worms were incubated for 3h on a nutator mixer at 20°C. Then, the samples were collected by centrifugation for 2 min at 2000 g and the supernatant discarded. Worms were

washed twice with M9 and once with ddH₂O to remove bacteria and salts. 25 µL worm pellets were transferred to 2 mL Eppendorf tubes and snap-frozen in liquid nitrogen. For fly samples: 150 flies per diet group were maintained at a density of 15 flies per vial with 10 replicates. Flies were transferred to fresh vials every 2 days and killed on day 10 by directly snap-freezing in liquid nitrogen in 2 mL Eppendorf tubes. For mouse samples: For each measurement a minimum of five biological replicates were collected. Pellets were lysed by metal bead beating for 1 min at 25 Hz. 1 mL mixture of methanol:acetonitrile:mili-Q ultrapure water (40:40:20 [v:v]), containing 25 µL internal standards U-¹³C¹⁵N amino acids (Cambridge isotopes), was added to each sample. The samples were incubated for 30 min on an orbital mixer at 4°C and 1,500 rpm. Then, the samples were sonicated for 10 min in a bath-type sonicator, which was cooled with ice. Subsequently, the samples were centrifuged for 10 min at 14,500 g for 10 min at 4°C. The supernatants were collected in a fresh Eppendorf tube and after vacuum centrifugation, in a SpeedVac concentrator set to 20°C at 1000 rpm for 4-6h stored at -80°C prior to analysis, while the insoluble pellets were dried by aspirating the remaining liquid off and used for protein quantification using the PierceTM BCA Protein Assay Kit (Thermo Fisher Scientific) and following the manufacturer's protocol.

4.13 Polysome profiling

For the analysis and translation via polysome profiling based on Derisbourg et al.¹⁶² and Ding and Großhans¹⁷⁸, synchronized gravid day 1 adults were grown on NGM plated seeded with OP50 bacteria. Per genotype and replicate ~12,000 worms were harvested and washed twice with M9: first with M9 supplemented with 1 mM cycloheximide (Sigma-Aldrich) and then with lysis buffer (20 mM Tris pH 8.5, 140 mM KCl, 1.5 mM MgCl₂, 0.5% Nonidet P40, 1 mM DTT, 1 mM cycloheximide). Worms were pelleted and resuspended in 350 µL cold lysis buffer supplemented with 1% sodium deoxycholate (DOC, Sigma-Aldrich). Resuspended worms were lysed using a chilled Dounce homogenizer. Ribonuclease inhibitor RNasin (Promega) was added to samples at a concentration of 0.4 Units/µL. Samples were then mixed and incubated on ice for 30 min, followed by a centrifugation step (12,000 g, 10 min, 4°C) for clearance. The pellet was discarded and the RNA concentration of the supernatant was measured by absorbance measurement at 260 nm.

To prepare sucrose gradients, 15% (w/v) and 60% (w/v) sucrose solutions were prepared in basic lysis buffer (20 mM Tris pH 8.5, 140 mM KCl, 1.5 mM MgCl₂, 1 mM DTT, 1 mM cycloheximide). Linear sucrose gradients were produced using a Gradient Master (Biocomp).

Equivalent amounts of sample (around 400 µg RNA) were loaded on the gradient and centrifuged at 39,000 g for 3h at 4°C, using an Optima L-100 XP Ultracentrifuge (Beckman Coulter) and the SW41Ti rotor. To analyze the sample on the gradient during fractionation, absorbance at 254 nm was measured and recorded (Econo UV monitor EM-1, Biorad) using the Gradient Profiler software (version 2.07). Gradient fractionation was performed from the top down using a Piston Gradient Fractionator (Biocomp) and a fraction collector (Model 2110, Biorad). For precise analysis of ribosomal fractions, they were collected by hand according to their absorbance profile; for RNAseq, fractions containing three or more ribosomes per mRNA were collected per sample. RNA extraction from total lysates and from each fraction was performed using the Direct-zol RNA MicroPrep Kit (Zymo Research) according to the manufacturer's recommendations.

4.14 Polysome sequencing

For polysome sequencing, monosome extracts, polysome extracts (excluding disomes), and corresponding total RNA were collected as detailed above. cDNA libraries were generated with ribosomal RNA depletion at the Cologne Center for Genomics and sequenced on the Illumina HiSeq2000 platform.

For data analysis, raw reads from all RNAseq and polysome sequencing replicates were mapped to the *C. elegans* reference genome (ENSEMBL 91) using HISAT2 (v2.1.0)¹⁷⁹. After guided transcriptome assembly with StringTie (v1.3.4d), transcriptomes were merged with Cuffmerge and quantification was performed with Cuffquant¹⁸⁰. The analysis for differential gene expression for total, monosomal and polysomal RNA was performed with Cuffdiff (Cufflinks v2.2.1)^{181,182}. To analyse the translome, the abundance of each mRNA in the polysomal fraction was normalized to its abundance in the total input mRNA. Respective normalized values were used to identify changes between different conditions using two-sided Student's t-test. DAVID analysis was performed to identify significantly enriched gene ontology (GO) terms¹⁸³.

4.15 Immunofluorescence assays

F1 animals for RNA knockdown assays of worms carrying *eri-1(mg366);GFP::NRDE-3* transgenes were obtained by bleaching gravid P0 that were grown on NGM plates containing 100 µg/µL ampicillin (Merck Millipore) and 1 mM IPTG (Roth) and seeded with HT115 bacteria expressing target RNAi. RNAi against *luciferase* was used as nontargeting control.

Liquid cultures were obtained from growing HT115 bacterial cultures overnight at 37°C in LB media with 100 µg/µL ampicillin (Merck Millipore) at 37°C and 180 rpm. The cultures were induced for three hours with 1 mM IPTG (Roth) at 37°C and 180 rpm. The bacteria were pelleted and fully resuspended in S-basal containing 100 µg/µL ampicillin (Merck Millipore) and 1 mM IPTG (Roth). Larva were allowed to grow from hatch in 2 mL Eppendorf tubes containing liquid culture for 4 days on a nutator mixer at 20°C, after which L3 larvae were collected and mounted on a tissue slide using 200 mM levamisole (Sigma-Aldrich).

F1 animals for methionine supplementation assays of worms carrying *hsp-6::GFP*, *hsp-60::GFP* or *eri-1(mg366);GFP::NRDE-3* transgenes were obtained by bleaching gravid P0 that were grown on NGM plates containing the indicated methionine concentration. Synchronized eggs were transferred by pipetting to 2 mL tubes containing 500 µL liquid culture consisting of S-basal and a 1.5-fold concentrate of freeze-killed OP50 *E. coli*. Concentrated freeze-killed OP50 bacteria was obtained by three cycles of snap-freezing and thawing pelleted overnight OP50 bacterial cultures. Additionally, methionine was added to the liquid culture at the indicated concentration. Larva carrying *hsp-6::GFP* or *hsp-60::GFP* transgenes were allowed to grow from hatch for 5 days on a nutator mixer at 20°C, after which L4 larvae were collected and mounted on a tissue slide using 200 mM levamisole (Sigma-Aldrich). Larva carrying *eri-1(mg366);GFP::NRDE-3* transgenes were allowed to grow from hatch for 4 days on a nutator mixer at 20°C, after which L3 larvae were collected and mounted on a tissue slide using 200 mM levamisole (Sigma-Aldrich).

For assays with *hsp-6::GFP* or *hsp-60::GFP* transgenics, images were captured using a Leica SPX-8 confocal microscope and 63X objective. For each worm the mean intensity of the entire animal was quantified. For assays with *eri-1(mg366);GFP::NRDE-3* transgenics, images were captured using a Leica SPX-8 confocal microscope and 100X objective. For each worm the average ratio of the mean intensity of three seam cell's nuclei versus cytosol was quantified. Immunofluorescent densities were quantified using ImageJ software. At least three independent experiments were performed of at least seven worms per condition. Throughout each experiment, strain and/or treatment were unknown to the researchers. Data were assembled on completion of the experiment. Error bars represent means ± SEM and statistical significance was calculated with the 2-way ANOVA multiple comparisons Tukey test.

4.16 Quantitative Reverse Transcription-PCR (qRT-PCR)

L3 larval stage worms were collected in TRI Reagent (Zymo Research) and snap-frozen using liquid nitrogen. Following the manufacturer's recommendations, RNA extraction was performed using the Direct-zol RNA MicroPrep Kit (Zymo Research) and cDNA synthesis using the iScript cDNA Synthesis Kit (BioRad). Relative RT-qPCR was performed using the Power SYBR Green PCR Master Mix (Applied Biosystems) on a ViiA 7 Real-Time PCR System (Applied Biosystems). Primers for the gene *eft-3* were used as internal control. Primer sequences are found in Supplementary Table 5. Error bars represent means \pm SEM from at least three independent biological replicates and assays were analyzed by two-sided Student's t-test.

4.17 Protein extraction for proteomics

Around 2000 worms were collected in M9 buffer, washed twice and a third wash was performed in water. Worms were pelleted and snap frozen in liquid N₂. Worm pellets were solubilized in lysis buffer: 6 M guanidium chloride (Sigma-Aldrich); 2.5 mM Tris(2-carboxyethyl)phosphine (Invitrogen); 10 mM chloroacetamide (Merck); 100 mM Tris-HCl (Sigma-Aldrich). Samples were heated at 95°C for 10 min, sonicated with a Bioruptor (30 sec sonication, 30 sec breaks, 10 cycles) and centrifuged at 20,000 g for 20 min at 4°C. Protein normalization was performed with the Nanodrop prior to enzymatic digestion. For each sample, a total of 300 µg of protein, diluted 10 times in 20 mM Tris, was digested with trypsin (Promega) overnight at 37°C. The digest was acidified with 50% of formic acid at the final concentration of 1% (v/v). The samples were centrifuged at 20,000 g for 10 min. Peptides were then cleaned up with StageTip Empore C18-SD desalting [3M] according to the manufacturer's protocol. After elution, samples were dried with a Speed Vac (Eppendorf) and re-suspend with 20 µL of 0.1% (v/v) of formic acid. Peptide concentration was measured using NanoDrop 2000 (Thermo Fisher Scientific). The solution was further dried and the peptide concentration was adjusted to 1 µg/µL; three microliters I used for mass spectrometric analysis.

4.18 LC-MS/MS analysis for proteomics

Peptides were separated on a 200 cm µPACTM column (PharmaFluidics) using an EASY-nLC 1200 (Thermo Fisher Scientific). Maximum pressure was set at 320 Bar. Buffer A and B were 0.1% formic acid in water and 0.1% formic acid in 80% acetonitrile. Peptides were separated on a segmented gradient from 6% to 28% buffer B for 120 min and from 28% to 50% buffer B for 25 min at 350 nL/min. Eluting peptides were analyzed on a Q Exactive HF mass

spectrometer (Thermo Fisher Scientific). Precursor m/z was measured at 120,000 resolution in the 300 to 1800 m/z range. The top ten most intense precursors with charge states from 2 to 7 only were selected for HCD fragmentation using 25% normalized collision energy. Fragment m/z values were measured at a resolution of 15,000 using a minimum AGC target of 1E4, an AGC target of 1E5, and 120 ms maximum injection time. Upon fragmentation, precursors were put on a dynamic exclusion list for 30 sec.

4.19 Protein identification and quantification

The raw data were analyzed with MaxQuant version 1.6.1.0¹⁸⁴ using the integrated Andromeda search engine¹⁸⁵. Peptide fragmentation spectra were searched against the canonical and isoform sequences of the *C. elegans* reference proteome (proteome ID UP000001940, downloaded September 2018 from UniProt). Methionine oxidation and protein N-terminal acetylation were set as variable modifications; cysteine carbamidomethylation was set as fixed modification. The digestion parameters were set to “specific” and “Trypsin/P”. The minimum number of peptides and razor peptides for protein identification was 1; the minimum number of unique peptides was 0. Protein identification was performed at a peptide spectrum matches and protein false discovery rate of 0.01. The “second peptide” option was on. Successful identifications were transferred between the different raw files using the “Match between runs” option. Label-free quantification (LFQ)¹⁸⁶ was performed using an LFQ minimum ratio count of two. Data wrangling and exploratory data analysis was done in R¹⁸⁷ using the dplyr and ggplot packages from the tidyverse¹⁸⁸. LFQ intensities were filtered for at least two valid values in at least one group and imputed from a normal distribution with a width of 0.3 and down shift of 1.8. Differential expression analysis was performed using limma¹⁸⁹.

4.20 Fly maintenance and survival analysis

Females of the outbred white Dahomey wild type strain¹⁹⁰ were used in all experiments. Flies were maintained on 1.0x SYA (10% (w/v) brewer’s yeast, 5% (w/v) sucrose and 1.5% (w/v) agar) food. Experimental flies were generated by transferring 20 μ L of eggs to culture bottles containing SYA medium, ensuring standard larval density. Newly emerged adults were collected over a period of 24h and transferred to fresh SYA food and allowed to mate for 48h. Subsequently, female flies were sorted under brief CO₂ anaesthesia and transferred to experimental vials containing chemically defined medium¹⁹¹. As control diet the yeast based YAA medium was prepared according to Piper et al.¹⁹¹. Methionine restriction was achieved by reducing its concentration to 20% of that of the YAA control diet (0.2X M). For lifespan

experiments, 150 female flies were maintained at a density of 10 flies per vial with 15 replicates. Flies were transferred to fresh vials every 2–3 days and the number of dead flies was scored on the day of transfer. Data were recorded in Excel, and log-rank test was performed to test for significant differences between groups. All fly experiments were performed at 25°C on a 12h:12h light:dark cycle at constant humidity (65%).

4.21 RNA-Sequencing sample preparation of fly samples

For RNA-Seq, 3 replicates of 25 female flies per diet were kept for 3 days on either the YAA 1X methionine control diet or on YAA with 0.2X methionine. Flies were snap-frozen in liquid nitrogen and total RNA was extracted from head and thorax of 25 frozen flies using Trizol (Invitrogen). The RNase free DNase kit (Qiagen) was used to remove DNA. Libraries for sequencing were generated using 2 µg of total RNA as input and polyA purification protocol. Library generation and RNA sequencing with 100 bp single-end reads and 35 million reads per sample was performed on an Illumina HiSeq 2500 platform at the Max Planck Genome Center, Cologne, Germany.

4.22 Mouse dietary restriction (DR) protocol

The mouse DR study was performed in accordance with the recommendations and guidelines of the Federation of the European Laboratory Animal Science Association (FELASA), with all protocols approved by the Landesamt für Natur, Umwelt und Verbraucherschutz, Nordrhein-Westfalen, Germany (reference no. 84-02.04.2015.A437). Details about mouse husbandry and implementation of DR were previously published¹⁹². In brief, female F₁ hybrid mice (C3B6F1) were generated in-house by crossing C3H/HeOJ females with C57BL/6NCrl males (strain codes 626 and 027, respectively, Charles River Laboratories). Animals were maintained in groups of 5 females in individually ventilated cages under specific-pathogen-free conditions with constant temperature (21°C), 50–60% humidity and a 12-hour light–dark cycle. All mice had constant access to nesting material and chew sticks and received commercially available rodent chow (ssniff R/M-H autoclavable, ssniff Spezialdiäten) and were provided with sterile-filtered water ad libitum. Food consumption of the AL group was measured weekly, and DR animals received 60% of the food amount consumed by AL animals. For metabolomic analysis, seven mice per diet group were killed at the age of 24 months by cervical dislocation, and tissues were collected and snap-frozen in liquid nitrogen.

4.23 Statistical analysis

Unless stated otherwise, results are presented as means \pm SEM. Unless noted otherwise, statistical tests were performed using two-sided Student's t-test, log-rank Mantel-Cox test, hypergeometric testing, two-way ANOVA multiple comparisons Tukey test or two-way ANOVA with Dunnet's multiple comparison test. Significance levels are indicated as * $p < 0,05$, ** $p < 0,01$, and *** $p < 0,001$ versus WT controls unless noted otherwise. Experiments were carried out with at least three biological replicates unless noted otherwise.

Reference list

1. UN. *World Population Prospects 2019 - Volume II: Demographic Profiles. World Population Prospects 2019 - Volume II: Demographic Profiles II*, (2020).
2. Pyrkov, T. V. *et al.* Longitudinal analysis of blood markers reveals progressive loss of resilience and predicts human lifespan limit. *Nat. Commun.* **12**, 1–10 (2021).
3. Ganceviciene, R., Liakou, A. I., Theodoridis, A., Makrantonaki, E. & Zouboulis, C. C. Skin anti-aging strategies. **4**, 308–319 (2012).
4. de Cabo, R. & Mattson, M. P. Effects of Intermittent Fasting on Health, Aging, and Disease. *N. Engl. J. Med.* **381**, 2541–2551 (2019).
5. Kulkarni, A. S. *et al.* Metformin regulates metabolic and nonmetabolic pathways in skeletal muscle and subcutaneous adipose tissues of older adults. *Aging Cell* **17**, e12723 (2018).
6. Benner, S. A. Defining Life. *Astrobiology* **10**, 1021 (2010).
7. Fujita, S., Kuranaga, E. & Nakajima, Y. Regeneration potential of jellyfish: Cellular mechanisms and molecular insights. *Genes (Basel)*. **12**, (2021).
8. Kemoun, P. *et al.* A gerophysiology perspective on healthy ageing. *Ageing Res. Rev.* **73**, 101537 (2022).
9. López-Otín, C., Blasco, M. A., Partridge, L., Serrano, M. & Kroemer, G. The hallmarks of aging. *Cell* **153**, 1194 (2013).
10. Kolora, S. R. R. *et al.* Origins and evolution of extreme life span in pacific ocean rockfishes. *Science (80-.)*. **374**, 842–847 (2021).
11. Nielsen, J. *et al.* Eye lens radiocarbon reveals centuries of longevity in the Greenland shark (*Somniosus microcephalus*). *Science* **353**, 702–704 (2016).
12. Terman, A. Garbage catastrophe theory of aging: imperfect removal of oxidative damage? <http://dx.doi.org/10.1179/135100001101535996> **6**, 15–26 (2013).
13. Quin, J. E. *et al.* Targeting the nucleolus for cancer intervention. *Biochim. Biophys. Acta - Mol. Basis Dis.* **1842**, 802–816 (2014).
14. Nussbaum-Krammer, C. I., Neto, M. F., Brielmann, R. M., Pedersen, J. S. & Morimoto, R. I. Investigating the Spreading and Toxicity of Prion-like Proteins Using the Metazoan Model Organism *C. elegans*. *J. Vis. Exp.* 52321 (2015). doi:10.3791/52321
15. Kim, E. B. *et al.* Genome sequencing reveals insights into physiology and longevity of the naked mole rat. *Nature* **479**, 223–7 (2011).

16. Lezzerini, M. & Budovskaya, Y. A dual role of the Wnt signaling pathway during aging in *Caenorhabditis elegans*. *Aging Cell* **13**, 8–18 (2014).
17. Kirkwood, T. B. L. Evolution of ageing. *Nat. 1977 2705635* **270**, 301–304 (1977).
18. Kreider, J. J., Pen, I. & Kramer, B. H. Antagonistic pleiotropy and the evolution of extraordinary lifespans in eusocial organisms. *Evol. Lett.* **5**, 178–186 (2021).
19. B. Friedman, D. & E. Johnson, T. A Mutation in the age-1 Gene in *Caenorhabditis elegans* Lengthens Life and Reduces Hermaphrodite Fertility. *Genetics* **118**, 75–86 (1988).
20. Hansen, M. *et al.* Lifespan extension by conditions that inhibit translation in *Caenorhabditis elegans*. *Aging Cell* **6**, 95–110 (2007).
21. Shmookler Reis, R. J., Ayyadevara, S., Crow, W. A., Lee, T. & Delongchamp, R. R. Gene categories differentially expressed in *C. elegans* age-1 mutants of extraordinary longevity: new insights from novel data-mining procedures. *J. Gerontol. A. Biol. Sci. Med. Sci.* **67**, 366–75 (2012).
22. Brenner, S. The genetics of *Caenorhabditis elegans*. *Genetics* **77**, 71–94 (1974).
23. Schumacher, B., Pothof, J., Vijg, J. & Hoeijmakers, J. H. J. The central role of DNA damage in the ageing process. *Nat. 2021 5927856* **592**, 695–703 (2021).
24. Labbadia, J. & Morimoto, R. I. The Biology of Proteostasis in Aging and Disease. *Annu. Rev. Biochem.* **84**, 150317182619002 (2014).
25. Walther, D. M. *et al.* Widespread Proteome Remodeling and Aggregation in Aging *C. elegans*. *Cell* **161**, 919–932 (2015).
26. McQuary, P. R. *et al.* *C. elegans* S6K Mutants Require a Creatine-Kinase-like Effector for Lifespan Extension. *Cell Rep.* **14**, 2059–2067 (2016).
27. Yang, J.-R., Chen, X. & Zhang, J. Codon-by-codon modulation of translational speed and accuracy via mRNA folding. *PLoS Biol.* **12**, e1001910 (2014).
28. Takauji, Y. *et al.* Restriction of protein synthesis abolishes senescence features at cellular and organismal levels. *Sci. Reports 2016 61* **6**, 1–10 (2016).
29. Javidnia, S. *et al.* Mendelian randomization analyses implicate biogenesis of translation machinery in human aging. *Genome Res.* **32**, 258–265 (2022).
30. Essers, P. *et al.* Reduced insulin/insulin-like growth factor signaling decreases translation in *Drosophila* and mice. *Sci. Rep.* **6**, 30290 (2016).
31. Depuydt, G., Shanmugam, N., Rasulova, M., Dhondt, I. & Braeckman, B. P. Increased Protein Stability and Decreased Protein Turnover in the *Caenorhabditis elegans* Ins/IGF-1 daf-2 Mutant. *J. Gerontol. A. Biol. Sci. Med. Sci.* **71**, 1553–1559 (2016).

32. Dever, T. E. & Green, R. The elongation, termination, and recycling phases of translation in eukaryotes. *Cold Spring Harb. Perspect. Biol.* **4**, a013706 (2012).
33. Shcherbakov, D. *et al.* Ribosomal mistranslation leads to silencing of the unfolded protein response and increased mitochondrial biogenesis. *Commun. Biol.* **2**, (2019).
34. Mohler, K. & Ibba, M. Translational fidelity and mistranslation in the cellular response to stress. *Nat. Microbiol.* **2**, 1–9 (2017).
35. Prabhakar, A., Choi, J., Wang, J., Petrov, A. & Puglisi, J. D. Dynamic basis of fidelity and speed in translation: Coordinated multistep mechanisms of elongation and termination. *Protein Sci.* **26**, 1352–1362 (2017).
36. Novoa, E. M. & Ribas De Pouplana, L. Speeding with control: codon usage, tRNAs, and ribosomes. *Trends Genet.* **28**, 574–581 (2012).
37. Prokhorova, I. *et al.* Aminoglycoside interactions and impacts on the eukaryotic ribosome. *Proc. Natl. Acad. Sci. U. S. A.* **114**, E10899–E10908 (2017).
38. Keeling, K. M., Xue, X., Gunn, G. & Bedwell, D. M. Therapeutics based on stop codon readthrough. *Annu. Rev. Genomics Hum. Genet.* **15**, 371–94 (2014).
39. Garreau De Loubresse, N. *et al.* Structural basis for the inhibition of the eukaryotic ribosome. *Nature* **513**, 517–523 (2014).
40. Ferreira, N. *et al.* Stress signaling and cellular proliferation reverse the effects of mitochondrial mistranslation. *EMBO J.* **38**, 1–19 (2019).
41. Balchin, D., Hayer-Hartl, M. & Hartl, F. U. In vivo aspects of protein folding and quality control. *Science (80-.).* **353**, (2016).
42. Vihervaara, A. & Sistonen, L. HSF1 at a glance. *J. Cell Sci.* **127**, 261–266 (2014).
43. Denzel, M. S. *et al.* Hexosamine pathway metabolites enhance protein quality control and prolong life. *Cell* **156**, 1167–1178 (2014).
44. Shalgi, R. *et al.* Widespread Regulation of Translation by Elongation Pausing in Heat Shock. *Mol. Cell* **49**, 439–452 (2013).
45. Parodi, A. J. Role of N-oligosaccharide endoplasmic reticulum processing reactions in glycoprotein folding and degradation. *Biochem. J.* **348 Pt 1**, 1–13 (2000).
46. Choe, Y.-J. *et al.* Failure of RQC machinery causes protein aggregation and proteotoxic stress. *Nature* 1–17 (2016). doi:10.1038/nature16973
47. Kirstein-Miles, J., Scior, A., Deuerling, E. & Morimoto, R. I. The nascent polypeptide-associated complex is a key regulator of proteostasis. *EMBO J.* **32**, 1451–68 (2013).
48. Brandman, O. *et al.* A ribosome-bound quality control complex triggers degradation of nascent peptides and signals translation stress. *Cell* **151**, 1042–1054 (2012).

49. Brunquell, J., Morris, S., Lu, Y., Cheng, F. & Westerheide, S. D. The genome-wide role of HSF-1 in the regulation of gene expression in *Caenorhabditis elegans*. *BMC Genomics* **17**, 1–18 (2016).
50. Sural, S., Lu, T. C., Jung, S. A. & Hsu, A. L. HSB-1 inhibition and HSF-1 overexpression trigger overlapping transcriptional changes to promote longevity in *Caenorhabditis elegans*. *G3 Genes, Genomes, Genet.* **9**, 1679–1692 (2019).
51. Turi, Z., Lacey, M., Mistrik, M. & Moudry, P. Impaired ribosome biogenesis: mechanisms and relevance to cancer and aging. **11**, 2512–2540 (2019).
52. Henras, A. K., Plisson-Chastang, C., O'Donohue, M. F., Chakraborty, A. & Gleizes, P. E. An overview of pre-ribosomal RNA processing in eukaryotes. *Wiley Interdiscip. Rev. RNA* **6**, 225–242 (2015).
53. Frazier, M. N., Pillon, M. C., Kocaman, S., Gordon, J. & Stanley, R. E. Structural overview of macromolecular machines involved in ribosome biogenesis. *Curr. Opin. Struct. Biol.* **67**, 51–60 (2021).
54. Li, D. & Wang, J. Ribosome heterogeneity in stem cells and development. *J. Cell Biol.* **219**, (2020).
55. Barandun, J., Hunziker, M. & Klinge, S. Assembly and structure of the SSU processome — a nucleolar precursor of the small ribosomal subunit. *Curr. Opin. Struct. Biol.* **49**, 85–93 (2018).
56. Albert, B. *et al.* A ribosome assembly stress response regulates transcription to maintain proteome homeostasis. *Elife* **8**, (2019).
57. Zhu, C. *et al.* Erroneous ribosomal RNAs promote the generation of antisense ribosomal siRNA. *Proc. Natl. Acad. Sci. U. S. A.* **115**, 10082–10087 (2018).
58. Tye, B. W. *et al.* Proteotoxicity from aberrant ribosome biogenesis compromises cell fitness. *Elife* **8**, 1–29 (2019).
59. Liang, X. H., Liu, Q. & Fournier, M. J. Loss of rRNA modifications in the decoding center of the ribosome impairs translation and strongly delays pre-rRNA processing. *RNA* **15**, 1716 (2009).
60. Kondrashov, N. *et al.* Ribosome-mediated specificity in Hox mRNA translation and vertebrate tissue patterning. *Cell* **145**, 383–397 (2011).
61. Ingolia, N. T. Ribosome Footprint Profiling of Translation throughout the Genome. *Cell* **165**, 22–33 (2016).
62. Mathis, A. D. *et al.* Mechanisms of In Vivo Ribosome Maintenance Change in Response to Nutrient Signals. *Mol. Cell. Proteomics* **16**, 243–254 (2017).

63. Mediani, L. *et al.* Defective ribosomal products challenge nuclear function by impairing nuclear condensate dynamics and immobilizing ubiquitin. *EMBO J.* 1–19 (2019). doi:10.15252/embj.2018101341
64. Dennis, P. B. *et al.* Mammalian TOR: A Homeostatic ATP Sensor. *Science* (80-.). **294**, 1102–1105 (2001).
65. Kapahi, P. *et al.* With TOR, Less Is More: A Key Role for the Conserved Nutrient-Sensing TOR Pathway in Aging. *Cell Metab.* **11**, 453–465 (2010).
66. Fontana, L. & Partridge, L. Promoting health and longevity through diet: From model organisms to humans. *Cell* **161**, 106–118 (2015).
67. Bröer, S. & Bröer, A. Amino acid homeostasis and signalling in mammalian cells and organisms. *Biochem. J.* **474**, 1935–1963 (2017).
68. Wu, C. C. C., Peterson, A., Zinshteyn, B., Regot, S. & Green, R. Ribosome Collisions Trigger General Stress Responses to Regulate Cell Fate. *Cell* **182**, 404–416.e14 (2020).
69. Lu, J. *et al.* Sestrin is a key regulator of stem cell function and lifespan in response to dietary amino acids. *Nat. Aging* 2020 11 **1**, 60–72 (2020).
70. Bartke, A., Westbrook, R., Sun, L. & Ratajczak, M. Links between growth hormone and aging. *Endokrynol. Pol.* **64**, 46–52 (2013).
71. Delaney, J. R. *et al.* Sir2 deletion prevents lifespan extension in 32 long-lived mutants. *Aging Cell* **10**, 1089–91 (2011).
72. Edwards, C. *et al.* Mechanisms of amino acid-mediated lifespan extension in *Caenorhabditis elegans*. *BMC Genet.* **16**, 1–24 (2015).
73. Parkhitko, A. A., Jouandin, P., Mohr, S. E. & Perrimon, N. Methionine metabolism and methyltransferases in the regulation of aging and lifespan extension across species. *Aging Cell* 1–18 (2019). doi:10.1111/ace1.13034
74. Cabreiro, F. *et al.* Metformin retards aging in *C. elegans* by altering microbial folate and methionine metabolism. *Cell* **153**, 228–239 (2013).
75. Liu, Y. J. *et al.* Glycine promotes longevity in *Caenorhabditis elegans* in a methionine cycle-dependent fashion. *PLOS Genet.* **15**, e1007633 (2019).
76. Haws, S. A. *et al.* Methyl-Metabolite Depletion Elicits Adaptive Responses to Support Heterochromatin Stability and Epigenetic Persistence. *Mol. Cell* **78**, 210–223.e8 (2020).
77. Ching, T.-T., Paal, A. B., Mehta, A., Zhong, L. & Hsu, A.-L. drr-2 encodes an eIF4H that acts downstream of TOR in diet-restriction-induced longevity of *C. elegans*. *Aging Cell* **9**, 545–557 (2010).

78. Wu, G., Flynn, N. E. & Knabe, D. A. Enhanced intestinal synthesis of polyamines from proline in cortisol-treated piglets. *Am. J. Physiol. Metab.* **279**, E395–E402 (2017).
79. Dever, T. E. & Ivanov, I. P. Roles of polyamines in translation. *J. Biol. Chem.* **293**, 18719–18729 (2018).
80. Minois, N., Carmona-Gutierrez, D. & Madeo, F. Polyamines in aging and disease. *Aging (Albany, NY)*. **3**, (2011).
81. Hussain, S. S., Ali, M., Ahmad, M. & Siddique, K. H. M. Polyamines: Natural and engineered abiotic and biotic stress tolerance in plants. *Biotechnol. Adv.* **29**, 300–311 (2011).
82. Eisenberg, T. *et al.* Induction of autophagy by spermidine promotes longevity. *Nat. Cell Biol.* **11**, 1305–1314 (2009).
83. Furukawa, K. *et al.* Polyamine synthesis from arginine and proline in tissues of developing chickens. *Amino Acids* **53**, 1739–1748 (2021).
84. Milne, K. *et al.* A fragment-like approach to PYCR1 inhibition. *Bioorganic Med. Chem. Lett.* **29**, 2626–2631 (2019).
85. Phang, J. M., Donald, S. P., Pandhare, J. & Liu, Y. The metabolism of proline, a stress substrate, modulates carcinogenic pathways. *Amino Acids* **35**, 681–690 (2008).
86. Tanner, J. J., Fendt, S. M. & Becker, D. F. The Proline Cycle As a Potential Cancer Therapy Target. *Biochemistry* **57**, 3433–3444 (2018).
87. Christensen, E. M. *et al.* In crystallo screening for proline analog inhibitors of the proline cycle enzyme PYCR1. *J. Biol. Chem.* **295**, 18316–18327 (2020).
88. Flibotte, S. *et al.* Whole-genome profiling of mutagenesis in *Caenorhabditis elegans*. *Genetics* **185**, 431–441 (2010).
89. Ruegenberg, S., Mayr, F. A. M. C., Atanassov, I., Baumann, U. & Denzel, M. S. Protein kinase A controls the hexosamine pathway by tuning the feedback inhibition of GFAT-1. *Nat. Commun.* 2021 121 **12**, 1–14 (2021).
90. Guerrero, G. A. *et al.* Nhr-8 and p-glycoproteins uncouple xenobiotic resistance from longevity in chemosensory c. *Elegans* mutants. *Elife* **10**, 1–18 (2021).
91. Bar-Nun, S., Shneyour, Y. & Beckmann, J. S. G-418, an elongation inhibitor of 80 S ribosomes. *Biochim. Biophys. Acta - Gene Struct. Expr.* **741**, 123–127 (1983).
92. Bidou, L., Allamand, V., Rousset, J.-P. & Namy, O. Sense from nonsense: therapies for premature stop codon diseases. *Trends Mol. Med.* **18**, 679–688 (2012).
93. Wangen, J. R. & Green, R. Stop codon context influences genome-wide stimulation of

- termination codon readthrough by aminoglycosides. *Elife* **9**, 1–29 (2020).
94. Minevich, G., Park, D. S., Blankenberg, D., Poole, R. J. & Hobert, O. CloudMap: a cloud-based pipeline for analysis of mutant genome sequences. *Genetics* **192**, 1249–69 (2012).
 95. Tabara, H., Grishok, A. & Mello, C. C. RNAi in *C. elegans*: soaking in the genome sequence. *Science* **282**, 430–1 (1998).
 96. Doitsidou, M., Poole, R. J., Sarin, S., Bigelow, H. & Hobert, O. *C. elegans* mutant identification with a one-step whole-genome-sequencing and SNP mapping strategy. *PLoS One* **5**, e15435 (2010).
 97. Meng, Z. *et al.* Crystal Structure of Human Pyrroline-5-carboxylate Reductase. *J. Mol. Biol.* **359**, 1364–1377 (2006).
 98. Bogner, A. N., Stiers, K. M. & Tanner, J. J. Structure, biochemistry, and gene expression patterns of the proline biosynthetic enzyme pyrroline-5-carboxylate reductase (PYCR), an emerging cancer therapy target. *Amino Acids* **53**, 1817–1834 (2021).
 99. Chen, D., Pan, K. Z., Palter, J. E. & Kapahi, P. Longevity determined by developmental arrest genes in *Caenorhabditis elegans*. *Aging Cell* **6**, 525–533 (2007).
 100. Zhuang, J. *et al.* PYCR1 interference inhibits cell growth and survival via c-Jun N-terminal kinase/insulin receptor substrate 1 (JNK/IRS1) pathway in hepatocellular cancer. *J. Transl. Med.* **17**, 343 (2019).
 101. Heier, C. R. & DiDonato, C. J. Translational readthrough by the aminoglycoside geneticin (G418) modulates SMN stability in vitro and improves motor function in SMA mice in vivo. *Hum. Mol. Genet.* **18**, 1310–1322 (2009).
 102. Gaubatz, J., Prashad, N. & Cutler, R. G. Ribosomal RNA gene dosage as a function of tissue and age for mouse and human. *Biochim. Biophys. Acta* **418**, 358–75 (1976).
 103. Halle, J. P., Müller, S., Simm, A. & Adam, G. Copy number, epigenetic state and expression of the rRNA genes in young and senescent rat embryo fibroblasts. *Eur. J. Cell Biol.* **74**, 281–8 (1997).
 104. Simsek, D. *et al.* The Mammalian Ribo-interactome Reveals Ribosome Functional Diversity and Heterogeneity. *Cell* **169**, 1051–1065.e18 (2017).
 105. Aguilaniu, H., Gustafsson, L., Rigoulet, M. & Nyström, T. Asymmetric inheritance of oxidatively damaged proteins during cytokinesis. *Science* **299**, 1751–3 (2003).
 106. Kern, A., Ackermann, B., Clement, A. M., Duerk, H. & Behl, C. HSF1-controlled and age-associated chaperone capacity in neurons and muscle cells of *C. elegans*. *PLoS*

- One* **5**, e8568 (2010).
107. Reynolds, R. M. & Phillips, P. C. Natural variation for lifespan and stress response in the nematode *Caenorhabditis remanei*. *PLoS One* **8**, e58212 (2013).
 108. Wu, J. *et al.* Comprehensive Profiling of Amino Acid Response Uncovers Unique Methionine-Deprived Response Dependent on Intact Creatine Biosynthesis. *PLOS Genet.* **11**, e1005158 (2015).
 109. Yordanova, M. M. *et al.* AMD1 mRNA employs ribosome stalling as a mechanism for molecular memory formation. *Nature* **553**, 356–360 (2018).
 110. Hansen, M., Hsu, A.-L., Dillin, A. & Kenyon, C. New genes tied to endocrine, metabolic, and dietary regulation of lifespan from a *Caenorhabditis elegans* genomic RNAi screen. *PLoS Genet.* **1**, 119–28 (2005).
 111. Huang, D. W., Sherman, B. T. & Lempicki, R. A. Systematic and integrative analysis of large gene lists using DAVID bioinformatics resources. *Nat. Protoc.* **4**, 44–57 (2009).
 112. Huang, D. W., Sherman, B. T. & Lempicki, R. A. Bioinformatics enrichment tools: paths toward the comprehensive functional analysis of large gene lists. *Nucleic Acids Res.* **37**, 1–13 (2009).
 113. Liu, P., Li, D., Li, W. & Wang, D. Mitochondrial Unfolded Protein Response to Microgravity Stress in Nematode *Caenorhabditis elegans*. *Sci. Rep.* **9**, 1–9 (2019).
 114. Labbadia, J. *et al.* Mitochondrial Stress Restores the Heat Shock Response and Prevents Proteostasis Collapse during Aging. *Cell Rep.* **21**, 1481–1494 (2017).
 115. Dunbar, T. L., Yan, Z., Balla, K. M., Smelkinson, M. G. & Troemel, E. R. C. *elegans* detects pathogen-induced translation inhibition to active immune signaling. *Cell Host Microbe* (2012). doi:10.1007/s10955-011-0269-9. Quantifying
 116. Létoquart, J. *et al.* Structural and functional studies of Bud23–Trm112 reveal 18S rRNA N7-G1575 methylation occurs on late 40S precursor ribosomes. *Proc. Natl. Acad. Sci.* **111**, E5518–E5526 (2014).
 117. Mao, H. *et al.* The Nrde Pathway Mediates Small-RNA-Directed Histone H3 Lysine 27 Trimethylation in *Caenorhabditis elegans*. *Curr. Biol.* **25**, 2398–2403 (2015).
 118. Mukherjee, R. N., Chen, P. & Levy, D. L. Recent advances in understanding nuclear size and shape. *Nucleus* **7**, 167–186 (2016).
 119. Tiku, V. *et al.* Small nucleoli are a cellular hallmark of longevity. *Nat. Commun.* **8**, (2016).
 120. Greer, E. L. *et al.* DNA Methylation on N6-Adenine in *C. elegans*. *Cell* **161**, 868–878

- (2015).
121. Kong, Y. *et al.* Critical assessment of DNA adenine methylation in eukaryotes using quantitative deconvolution. *Science (80-.).* **375**, 515–522 (2022).
 122. Hsu, C. L., Lo, Y. C. & Kao, C. F. H3K4 methylation in aging and metabolism. *Epigenomes* **5**, 1–19 (2021).
 123. Murgatroyd, C. & Spengler, D. Histone tales: Echoes from the past, prospects for the future. *Genome Biol.* **11**, 10–12 (2010).
 124. Booth, L. N. & Brunet, A. The Aging Epigenome. *Mol. Cell* **62**, 728–744 (2016).
 125. Oki, S. *et al.* ChIP-Atlas: a data-mining suite powered by full integration of public ChIP-seq data. *EMBO Rep.* **19**, e46255 (2018).
 126. Oki, S. & Ohta, T. ChIP-Atlas. *ChIP-Atlas* (2015).
 127. Guillermo, A. R. R. *et al.* H3K27 modifiers regulate lifespan in *C. elegans* in a context-dependent manner. *BMC Biol.* **19**, 1–17 (2021).
 128. Blackwell, T. K., Steinbaugh, M. J., Hourihan, J. M., Ewald, C. Y. & Isik, M. SKN-1/Nrf, stress responses, and aging in *Caenorhabditis elegans*. *Free Radic. Biol. Med.* **88**, 290–301 (2015).
 129. Takacs, Z. *et al.* ATG-18 and EPG-6 are Both Required for Autophagy but Differentially Contribute to Lifespan Control in *Caenorhabditis elegans*. *Cells* **8**, 236 (2019).
 130. Morley, J. F. & Morimoto, R. I. Regulation of Longevity in *Caenorhabditis elegans* by Heat Shock Factor and Molecular Chaperones. *Mol. Biol. Cell* **15**, 657–664 (2004).
 131. Henis-Korenblit, S. *et al.* Insulin/IGF-1 signaling mutants reprogram ER stress response regulators to promote longevity. *Proc. Natl. Acad. Sci. U. S. A.* **107**, 9730–9735 (2010).
 132. Hsu, A.-L., Murphy, C. T. & Kenyon, C. Regulation of Aging and Age-Related Disease by DAF-16 and Heat-Shock Factor. *Science (80-.).* **300**, 1142–1145 (2003).
 133. Liang, V. *et al.* Altered proteostasis in aging and heat shock response in *C. elegans* revealed by analysis of the global and de novo synthesized proteome. *Cell. Mol. Life Sci.* **71**, 3339–61 (2014).
 134. Gonsalves, S. E., Moses, A. M., Razak, Z., Robert, F. & Westwood, J. T. Whole-Genome Analysis Reveals That Active Heat Shock Factor Binding Sites Are Mostly Associated with Non-Heat Shock Genes in *Drosophila melanogaster*. *PLoS One* **6**, e15934 (2011).
 135. Weindruch, R., Walford, R. L., Fligiel, S. & Guthrie, D. The retardation of aging in

- mice by dietary restriction: Longevity, cancer, immunity and lifetime energy intake. *J. Nutr.* **116**, 641–654 (1986).
136. Mattison, J. A. *et al.* Caloric restriction improves health and survival of rhesus monkeys. *Nat. Commun.* **8**, (2017).
 137. Hahn, O. *et al.* Dietary restriction protects from age-associated DNA methylation and induces epigenetic reprogramming of lipid metabolism. *Genome Biol.* **18**, 1–18 (2017).
 138. Kovács, D. *et al.* HSF1Base: A comprehensive database of HSF1 (heat shock factor 1) target genes. *Int. J. Mol. Sci.* **20**, 1–24 (2019).
 139. Christensen, E. M. *et al.* Resolving the cofactor-binding site in the proline biosynthetic enzyme human pyrroline-5-carboxylate reductase 1. *J. Biol. Chem.* **292**, 7233–7243 (2017).
 140. Steinert, P. M. *et al.* Glycine loops in proteins: their occurrence in certain intermediate filament chains, loricrins and single-stranded RNA binding proteins. *Int. J. Biol. Macromol.* **13**, 130–139 (1991).
 141. Hayzer, D. J. & Leisinger, T. The Gene-Enzyme Relationships of Proline Biosynthesis in *Escherichia coli*. *Microbiology* **118**, 287–293 (1980).
 142. Deuschle, K. *et al.* The Role of Δ^1 -Pyrroline-5-Carboxylate Dehydrogenase in Proline Degradation. *Plant Cell* **16**, 3413 (2004).
 143. Pang, S. & Curran, S. P. Adaptive Capacity to Bacterial Diet Modulates Aging in *C. elegans*. *Cell Metab.* **19**, 221–231 (2014).
 144. Zhang, T. *et al.* Overexpression of methionine adenosyltransferase II alpha (MAT2A) in gastric cancer and induction of cell cycle arrest and apoptosis in SGC-7901 cells by shRNA-mediated silencing of MAT2A gene. *Acta Histochem.* **115**, 48–55 (2013).
 145. Chen, C. C., Lim, C. Y., Lee, P. J., Hsu, A. L. & Ching, T. T. S-adenosyl methionine synthetase SAMS-5 mediates dietary restriction-induced longevity in *Caenorhabditis elegans*. *PLoS One* **15**, 1–10 (2020).
 146. Jackson, L. K., Goldsmith, E. J. & Phillips, M. A. X-ray Structure Determination of *Trypanosoma brucei* Ornithine Decarboxylase Bound to D-Ornithine and to G418 INSIGHTS INTO SUBSTRATE BINDING AND ODC CONFORMATIONAL FLEXIBILITY* Downloaded from. *J. Biol. Chem.* **278**, 22037–22043 (2003).
 147. Cridge, A. G., Crowe-Mcauliffe, C., Mathew, S. F. & Tate, W. P. Eukaryotic translational termination efficiency is influenced by the 3 nucleotides within the ribosomal mRNA channel. *Nucleic Acids Res.* 1–18 (2018). doi:10.1093/nar/gkx1315
 148. Williams, R., Laskovs, M., Williams, R. I., Mahadevan, A. & Labbadia, J. A

- Mitochondrial Stress-Specific Form of HSF1 Protects against Age-Related Proteostasis Collapse. *Dev. Cell* **54**, 758–772.e5 (2020).
149. Szyller, J. & Bil-Lula, I. Heat Shock Proteins in Oxidative Stress and Ischemia/Reperfusion Injury and Benefits from Physical Exercises: A Review to the Current Knowledge. *Oxid. Med. Cell. Longev.* **2021**, (2021).
 150. Liang, X., Zhang, L., Natarajan, S. K. & Becker, D. F. Proline Mechanisms of Stress Survival. *Antioxidants Redox Signal.* **19**, 998–1011 (2013).
 151. Sun, L., Sadighi Akha, A. A., Miller, R. A. & Harper, J. M. Life-Span Extension in Mice by Prewaning Food Restriction and by Methionine Restriction in Middle Age. *J Gerontol A Biol Sci Med Sci* **64A**, 711–722 (2009).
 152. Lee, B. C. *et al.* Methionine restriction extends lifespan of *Drosophila melanogaster* under conditions of low amino-acid status. *Nat. Commun.* **5**, 3592 (2014).
 153. Orentreich, N., Matias, J. R., DeFelice, A. & Zimmerman, J. A. Low Methionine Ingestion by Rats Extends Life Span. *J. Nutr.* **123**, 269–274 (1993).
 154. Conn, C. S. & Qian, S. B. Nutrient signaling in protein homeostasis: An increase in quantity at the expense of quality. *Sci. Signal.* **6**, 1–10 (2013).
 155. Oudaert, I. *et al.* Pyrroline-5-Carboxylate Reductase 1: a novel target for sensitizing multiple myeloma cells to bortezomib by inhibition of PRAS40-mediated protein synthesis. *J. Exp. Clin. Cancer Res.* 2022 411 **41**, 1–17 (2022).
 156. Ou, R. *et al.* Downregulation of pyrroline-5-carboxylate reductase-2 induces the autophagy of melanoma cells via AMPK/mTOR pathway. *Tumor Biol.* **37**, 6485–6491 (2016).
 157. Wang, Q. L. & Liu, L. PYCR1 is associated with papillary renal cell carcinoma progression. *Open Med.* **14**, 586–592 (2019).
 158. Kitada, M., Xu, J., Ogura, Y., Monno, I. & Koya, D. Mechanism of Activation of Mechanistic Target of Rapamycin Complex 1 by Methionine. *Front. Cell Dev. Biol.* **8**, 1–7 (2020).
 159. Schmeisser, K. & Parker, J. A. Pleiotropic effects of mTOR and autophagy during development and aging. *Front. Cell Dev. Biol.* **7**, 192 (2019).
 160. Pakos-Zebrucka, K. *et al.* The integrated stress response. *EMBO Rep.* **17**, 1374–1395 (2016).
 161. Cabianca, D. S. *et al.* Active chromatin marks drive spatial sequestration of heterochromatin in *C. elegans* nuclei. *Nature* **569**, 734–739 (2019).
 162. Derisbourg, M. J., Wester, L. E., Baddi, R. & Denzel, M. S. Mutagenesis screen

- uncovers lifespan extension through integrated stress response inhibition without reduced mRNA translation. *Nat. Commun.* 1–14 (2021). doi:10.1038/s41467-021-21743-x
163. Maro, G. S., Han, S., Banko, M. R., Gozani, O. & Brunet, A. Members of the Histone H3 Lysine 4 Trimethylation Complex Regulate Lifespan in a Germline-dependent Manner in *C. elegans*. **466**, 2009 (2010).
 164. Schosserer, M. *et al.* Methylation of ribosomal RNA by NSUN5 is a conserved mechanism modulating organismal lifespan. *Nat. Commun.* **6**, (2015).
 165. Ishiguro, K., Arai, T. & Suzuki, T. Depletion of S-adenosylmethionine impacts on ribosome biogenesis through hypomodification of a single rRNA methylation. *Nucleic Acids Res.* **47**, 4226–4239 (2019).
 166. Kishita, Y. *et al.* Intra-mitochondrial methylation deficiency due to mutations in SLC25A26. *Am. J. Hum. Genet.* **97**, 761–768 (2015).
 167. Park, S. K., Tedesco, P. M. & Johnson, T. E. Oxidative stress and longevity in *Caenorhabditis elegans* as mediated by SKN-1. *Aging Cell* **8**, 258–269 (2009).
 168. Ye, C. *et al.* Demethylation of the Protein Phosphatase PP2A Promotes Demethylation of Histones to Enable Their Function as a Methyl Group Sink. *Mol. Cell* **73**, 1115–1126.e6 (2019).
 169. Qadota, H. *et al.* Protein phosphatase 2A is crucial for sarcomere organization in *Caenorhabditis elegans* striated muscle. *Mol. Biol. Cell* **29**, 2084–2097 (2018).
 170. Lin, D. S. *et al.* Compound heterozygous mutations in PYCR1 further expand the phenotypic spectrum of De Barsy syndrome. *Am. J. Med. Genet. Part A* **155**, 3095–3099 (2011).
 171. Chen, S. *et al.* SIRT3 regulates cancer cell proliferation through deacetylation of PYCR1 in proline metabolism. *Neoplasia* **21**, 665–675 (2019).
 172. Cai, F. *et al.* Pyrroline-5-carboxylate reductase 1 promotes proliferation and inhibits apoptosis in non-small cell lung cancer. *Oncol. Lett.* **15**, 731–740 (2016).
 173. Robert, X. & Gouet, P. Deciphering key features in protein structures with the new ENDscript server. *Nucleic Acids Res.* **42**, 320–324 (2014).
 174. Jumper, J. & Hassabis, D. Protein structure predictions to atomic accuracy with AlphaFold. *Nat. Methods* 2022 191 **19**, 11–12 (2022).
 175. Iqbal, A., Duitama, C., Metge, F., Rosskopp, D. & Boucas, J. Flaski. *Flaski* (2021). doi:10.5281/zenodo.4849515
 176. Kamath, R. & Ahringer, J. Genome-wide RNAi screening in *Caenorhabditis elegans*.

- Methods* **30**, 313–321 (2003).
177. Rual, J.-F., Ceron, J., Koreth, J., Hao, T. & al., et. Toward Improving *Caenorhabditis elegans* Phenome Mapping With an ORFeome-Based RNAi Library. *Genome Res.* **14**, 2162–2168 (2004).
 178. Ding, X. C. & Großhans, H. Repression of *C. elegans* microRNA targets at the initiation level of translation requires GW182 proteins. *EMBO J.* **28**, 213 (2009).
 179. Kim, D., Langmead, B. & Salzberg, S. L. HISAT: a fast spliced aligner with low memory requirements. *Nat. Methods* **12**, 357–360 (2015).
 180. Pertea, M. *et al.* StringTie enables improved reconstruction of a transcriptome from RNA-seq reads. *Nat. Biotechnol.* **33**, 290–295 (2015).
 181. Trapnell, C. *et al.* Transcript assembly and quantification by RNA-Seq reveals unannotated transcripts and isoform switching during cell differentiation. *Nat. Biotechnol.* **28**, 511–515 (2010).
 182. Trapnell, C. *et al.* Differential analysis of gene regulation at transcript resolution with RNA-seq. *Nat. Biotechnol.* **31**, 46–53 (2013).
 183. Fresno, C. & Fernandez, E. A. RDAVIDWebService: a versatile R interface to DAVID. *Bioinformatics* **29**, 2810–2811 (2013).
 184. Cox, J. & Mann, M. MaxQuant enables high peptide identification rates, individualized p.p.b.-range mass accuracies and proteome-wide protein quantification. *Nat. Biotechnol.* **26**, 1367–1372 (2008).
 185. Cox, J. *et al.* Andromeda: A peptide search engine integrated into the MaxQuant environment. *J. Proteome Res.* **10**, 1794–1805 (2011).
 186. Cox, J. *et al.* Accurate proteome-wide label-free quantification by delayed normalization and maximal peptide ratio extraction, termed MaxLFQ. *Mol. Cell. Proteomics* **13**, 2513–2526 (2014).
 187. Team, R. C. R: A Language and Environment for Statistical Computing. *R Foundation for Statistical Computing* (2017). Available at: <https://www.r-project.org/>.
 188. Wickham, H. *et al.* Welcome to the Tidyverse. *J. Open Source Softw.* **4**, 1686 (2019).
 189. Ritchie, M. E. *et al.* Limma powers differential expression analyses for RNA-sequencing and microarray studies. *Nucleic Acids Res.* **43**, e47 (2015).
 190. Grönke, S., Clarke, D. F., Broughton, S., Andrews, T. D. & Partridge, L. Molecular evolution and functional characterization of *Drosophila* insulin-like peptides. *PLoS Genet.* **6**, (2010).
 191. Piper, M. & Partridge, L. Preparation of a holidic medium for *Drosophila*

- melanogaster. *Protoc. Exch.* 1–4 (2013). doi:10.1038/protex.2013.082
192. Hahn, O. *et al.* A nutritional memory effect counteracts benefits of dietary restriction in old mice. *Nat. Metab.* **1**, 1059–1073 (2019).
193. Perez-Riverol, Y. *et al.* The PRIDE database and related tools and resources in 2019: Improving support for quantification data. *Nucleic Acids Res.* **47**, D442–D450 (2019).

Supplementary Information

Date	Strain	Treatment	Mean LS (days)	Δ (%)	dead/censored animals	Reference control	p value	Reference control	p value	Appears in
2017-11-27	wildtype N2 Bristol	none	23	0	85/65					Figure 13e
	<i>pycr-1(wrm22) X.</i>	none	30	34	65/85	vs wildtype control	<0.01			
2019-05-28	wildtype N2 Bristol	200 mM paraquat	3 (median)	0	60/0					Figure 20a
	<i>pycr-1(wrm22) X.</i>	200 mM paraquat	5 (median)	67	60/0	vs wildtype paraquat	<0.01			
2020-05-26	wildtype N2 Bristol	35°C	5.5 h (median)	0	60/0					Figure 20b
	<i>pycr-1(wrm22) X.</i>	35°C	6 h (median)	9	60/0	vs wildtype 35°C	<0.05	vs wildtype at 6 h	<0.01	
2020-01-08	wildtype N2 Bristol	Control	19	0	85/15					Figure 22e
	wildtype N2 Bristol	25 mM methionine	17	-9	92/8	vs wildtype control	<0.01			
	wildtype N2 Bristol	50 mM methionine	18	-2	51/49	vs wildtype control	0.78			
	<i>pycr-1(wrm22) X.</i>	Control	14	29	54/46	vs wildtype control	<0.01			
	<i>pycr-1(wrm22) X.</i>	25 mM methionine	22	15	72/28	vs wildtype control	<0.01	vs <i>pyr-1(wrm22)</i> control	<0.01	
	<i>pycr-1(wrm22) X.</i>	50 mM methionine	20	8	70/30	vs wildtype control	<0.01	vs <i>pyr-1(wrm22)</i> control	<0.01	
2019-08-29	wildtype N2 Bristol	Control	18	0	109/16					
	wildtype N2 Bristol	25 mM methionine	18	2	97/28	vs wildtype control	0.72			
	wildtype N2 Bristol	50 mM methionine	15	-16	106/19	vs wildtype control	<0.01			
	<i>pycr-1(wrm22) X.</i>	Control	23	27	67/58	vs wildtype control	<0.01			
	<i>pycr-1(wrm22) X.</i>	25 mM methionine	15	-14	119/6	vs wildtype control	<0.01	vs <i>pyr-1(wrm22)</i> control	<0.01	
	<i>pycr-1(wrm22) X.</i>	50 mM methionine	18	3	88/37	vs wildtype control	0.31	vs <i>pyr-1(wrm22)</i> control	<0.01	
2019-06-08	wildtype N2 Bristol	Control	18	0	26/99					
	wildtype N2 Bristol	25 mM methionine	18	3	87/38	vs wildtype control	0.4			
	<i>pycr-1(wrm22) X.</i>	Control	23	26	55/70	vs wildtype control	<0.01			
	<i>pycr-1(wrm22) X.</i>	25 mM methionine	21	18	75/50	vs wildtype control	<0.01	vs <i>pyr-1(wrm22)</i> control	0.08	
2020-01-12	wildtype N2 Bristol	<i>luciferase</i>	20	0	63/37					

	wildtype N2 Bristol	<i>hsf-1</i>	10	-49	74/26	vs wildtype luciferase	<0.01	
	<i>pycr-1(wrm22) X.</i>	<i>luciferase</i>	25	25	68/32	vs wildtype luciferase	<0.01	
	<i>pycr-1(wrm22) X.</i>	<i>hsf-1</i>	13	-35	73/27	vs wildtype luciferase	<0.01	vs <i>pyr-1(wrm22)</i> <i>luciferase</i> <0.01
2020-01-07	wildtype N2 Bristol	<i>luciferase</i>	19	0	96/4			
	wildtype N2 Bristol	<i>hsf-1</i>	12	-39	45/55	vs wildtype luciferase	<0.01	
	<i>pycr-1(wrm22) X.</i>	<i>luciferase</i>	27	43	88/12	vs wildtype luciferase	<0.01	
	<i>pycr-1(wrm22) X.</i>	<i>hsf-1</i>	13	-33	85/15	vs wildtype luciferase	<0.01	vs <i>pyr-1(wrm22)</i> <i>luciferase</i> <0.01
								Figure 29a
2019-04-10	wildtype N2 Bristol	<i>luciferase</i>	20	0	46/54			
	wildtype N2 Bristol	<i>hsf-1</i>	8	-59	49/51	vs wildtype luciferase	<0.01	
	<i>pycr-1(wrm22) X.</i>	<i>luciferase</i>	29	43	21/79	vs wildtype luciferase	<0.01	
	<i>pycr-1(wrm22) X.</i>	<i>hsf-1</i>	10	-50	34/66	vs wildtype luciferase	<0.01	vs <i>pyr-1(wrm22)</i> <i>luciferase</i> <0.01
2020-10-05	Female white Dahomey wildtype	1X methionine YAA	81 (median)	0	157/3			
		0.2X methionine YAA						
	Female white Dahomey wildtype		85 (median)	5	146/4	vs 1X YAA	<0.01	Figure 30a
2019-02-07	wildtype N2 Bristol	<i>luciferase</i>	13	0	84/66			
	wildtype N2 Bristol	<i>atg-18</i>	16	27	104/46	vs wildtype luciferase	<0.01	
	wildtype N2 Bristol	<i>daf-16</i>	16	31	119/31	vs wildtype luciferase	<0.01	
	wildtype N2 Bristol	<i>skn-1</i>	18	40	108/42	vs wildtype luciferase	<0.01	
	wildtype N2 Bristol	<i>xbp-1</i>	18	43	125/25	vs wildtype luciferase	<0.01	
	<i>pycr-1(wrm22) X.</i>	<i>luciferase</i>	24	94	106/44	vs wildtype luciferase	<0.01	
	<i>pycr-1(wrm22) X.</i>	<i>atg-18</i>	18	46	100/50	vs wildtype luciferase	<0.01	vs <i>pyr-1(wrm22)</i> <i>luciferase</i> <0.01
	<i>pycr-1(wrm22) X.</i>	<i>daf-16</i>	16	24	62/88	vs wildtype luciferase	<0.01	vs <i>pyr-1(wrm22)</i> <i>luciferase</i> <0.01
	<i>pycr-1(wrm22) X.</i>	<i>skn-1</i>	20	58	110/40	vs wildtype luciferase	<0.01	vs <i>pyr-1(wrm22)</i> <i>luciferase</i> <0.01
	<i>pycr-1(wrm22) X.</i>	<i>xbp-1</i>	11	-15	106/81	vs wildtype luciferase	<0.01	vs <i>pyr-1(wrm22)</i> <i>luciferase</i> <0.01
2019-04-10	wildtype N2 Bristol	<i>luciferase</i>	20	0	46/54			
	wildtype N2 Bristol	<i>atg-18</i>	17	-18	59/41	vs wildtype luciferase	<0.01	
	wildtype N2 Bristol	<i>bec-1</i>	15	-28	54/46	vs wildtype luciferase	<0.01	
	wildtype N2 Bristol	<i>daf-16</i>	12	-41	65/35	vs wildtype luciferase	<0.01	

	wildtype N2 Bristol	<i>ncl-1</i>	11	-44	45/55	vs wildtype luciferase	<0.01		
	wildtype N2 Bristol	<i>skn-1</i>	17	-18	76/24	vs wildtype luciferase	<0.01		
	wildtype N2 Bristol	<i>xbp-1</i>	18	-13	71/29	vs wildtype luciferase	<0.01		
	<i>pycr-1(wrm22) X.</i>	<i>luciferase</i>	29	43	21/79	vs wildtype luciferase	<0.01		
	<i>pycr-1(wrm22) X.</i>	<i>atg-18</i>	28	36	42/58	vs wildtype luciferase	<0.01	vs <i>pyr-1(wrm22)</i> <i>luciferase</i>	0,44
	<i>pycr-1(wrm22) X.</i>	<i>bec-1</i>	18	-12	16/84	vs wildtype luciferase	0,03	vs <i>pyr-1(wrm22)</i> <i>luciferase</i>	<0.01
	<i>pycr-1(wrm22) X.</i>	<i>daf-16</i>	16	-21	57/43	vs wildtype luciferase	<0.01	vs <i>pyr-1(wrm22)</i> <i>luciferase</i>	<0.01
	<i>pycr-1(wrm22) X.</i>	<i>ncl-1</i>	14	-29	48/52	vs wildtype luciferase	<0.01	vs <i>pyr-1(wrm22)</i> <i>luciferase</i>	<0.01
	<i>pycr-1(wrm22) X.</i>	<i>skn-1</i>	22	7	48/52	vs wildtype luciferase	<0.01	vs <i>pyr-1(wrm22)</i> <i>luciferase</i>	<0.01
	<i>pycr-1(wrm22) X.</i>	<i>xbp-1</i>	22	8	55/45	vs wildtype luciferase	0,18	vs <i>pyr-1(wrm22)</i> <i>luciferase</i>	<0.01
2020-01-07	wildtype N2 Bristol	<i>luciferase</i>	19	0	97/3				
	wildtype N2 Bristol	<i>ncl-1</i>	15	-19	59/41	vs wildtype luciferase	<0.01		
	<i>pycr-1(wrm22) X.</i>	<i>luciferase</i>	26	34	66/34	vs wildtype luciferase	<0.01		
	<i>pycr-1(wrm22) X.</i>	<i>ncl-1</i>	19	-2	73/27	vs wildtype luciferase	0,49	vs <i>pyr-1(wrm22)</i> <i>luciferase</i>	<0.01

Supplementary Table 1: Lifespan assay statistics

Gene name	Total mRNA			Polysome-associated mRNA		
	log2(fold change)	p value	q value	log2(fold change)	p value	q value
<i>rpl-1</i>	-0,15523	0,3123	0,409165	-0,320332	0,05075	0,0911588
<i>rpl-2</i>	-0,0050984	0,9749	0,982036	-0,372017	0,02565	0,0508761
<i>rpl-3</i>	-0,191166	0,23825	0,329758	-0,292709	0,10525	0,168554
<i>rpl-4</i>	-0,113462	0,47385	0,571307	-0,303591	0,08115	0,135531
<i>rpl-5</i>	-0,0379178	0,80435	0,85541	-0,306181	0,0724	0,123071
<i>rpl-6</i>	-0,000372727	0,9985	0,998793	-0,358449	0,0644	0,111478
<i>rpl-7</i>	0,0194812	0,90245	0,928666	-0,248006	0,1326	0,203992
<i>rpl-7A</i>	-0,111348	0,46975	0,567428	-0,368923	0,0264	0,0521521
<i>rpl-9</i>	-0,0175771	0,9056	0,931147	-0,499826	0,0021	0,00583415
<i>rpl-10</i>	-0,0439011	0,77485	0,832445	-0,280159	0,09255	0,151369
<i>rpl-11.1</i>	-0,294487	0,04995	0,0899521	-0,526581	0,0022	0,0060789
<i>rpl-11.2</i>	0,162143	0,2666	0,35983	0,618128	0,00005	0,000207195
<i>rpl-12</i>	-0,145934	0,33795	0,435992	-0,263543	0,0986	0,159598
<i>rpl-13</i>	-0,0594121	0,7033	0,774996	-0,271521	0,0951	0,154807
<i>rpl-14</i>	-0,0584545	0,69755	0,77035	-0,347491	0,02785	0,0545651
<i>rpl-15</i>	-0,0948664	0,5366	0,629629	-0,356824	0,0343	0,0652253
<i>rpl-16</i>	0,0162606	0,917	0,939736	-0,325436	0,05385	0,095819
<i>rpl-17</i>	0,00400903	0,98055	0,985988	-0,242875	0,1253	0,194727
<i>rpl-18</i>	-0,0990953	0,50695	0,602063	-0,473448	0,0031	0,00818628
<i>rpl-19</i>	0,077349	0,6099	0,695364	-0,174461	0,2722	0,36597
<i>rpl-20</i>	-0,0587207	0,7016	0,77367	not detected		
<i>rpl-21</i>	-0,00947738	0,94745	0,96273	-0,431569	0,0073	0,0172838
<i>rpl-22</i>	-0,107306	0,4642	0,562165	-0,24083	0,1036	0,166294
<i>rpl-23</i>	-0,126552	0,3998	0,499439	-0,289062	0,0704	0,120227
<i>rpl-24.1</i>	0,0440108	0,76945	0,828192	-0,396004	0,0142	0,0306853
<i>rpl-24.2</i>	-0,127336	0,5933	0,680999	-0,124986	0,4867	0,583426
<i>rpl-25.1</i>	0,338501	0,0283	0,0553135	0,744317	0,00005	0,000207195
<i>rpl-25.2</i>	-0,105191	0,47595	0,57329	-0,41268	0,00875	0,0202054
<i>rpl-26</i>	-0,00299574	0,9833	0,987781	-0,297277	0,05205	0,0931082
<i>rpl-27</i>	-0,056493	0,70385	0,775453	-0,319689	0,044	0,0806962
<i>rpl-28</i>	-0,0585601	0,6853	0,760237	-0,463454	0,00225	0,00619824
<i>rpl-29</i>	-0,0322796	0,81645	0,864697	-0,405602	0,00395	0,010126
<i>rpl-30</i>	0,0336594	0,81985	0,867288	-0,196831	0,1877	0,271407
<i>rpl-31</i>	0,00289516	0,9852	0,98916	-0,341706	0,0191	0,039535
<i>rpl-32</i>	-0,0922572	0,5602	0,651137	-0,327355	0,04045	0,0751056
<i>rpl-33</i>	0,0366214	0,80635	0,856863	-0,385569	0,0108	0,0242478
<i>rpl-34</i>	-0,0548455	0,70505	0,776505	-0,36335	0,01605	0,0340727
<i>rpl-35</i>	-0,00175652	0,9905	0,992865	-0,344203	0,0284	0,0554901
<i>rpl-36</i>	0,170272	0,2493	0,341744	-0,526829	0,0012	0,00358868
<i>rpl-36.A</i>	-0,0076659	0,95745	0,970029	-0,42424	0,0058	0,0141576

<i>rpl-37</i>	0,104839	0,6644	0,742509	-0,381286	0,1327	0,204111
<i>rpl-38</i>	-0,0203392	0,89085	0,920149	-0,620398	0,00005	0,000207195
<i>rpl-39</i>	-0,0162417	0,9087	0,933384	-0,503441	0,00055	0,00181303
<i>rpl-41.1</i>	-0,0889542	0,5531	0,644637	-0,366544	0,0544	0,0966723
<i>rpl-41.2</i>	-0,0951903	0,53145	0,624847	-0,619907	0,0003	0,00105745
<i>rpl-42</i>	0,512531	0,03375	0,0643499	0,484466	0,0708	0,120827
<i>rpl-43</i>	-0,0442248	0,7636	0,823535	-0,453715	0,00235	0,00643706
<i>rps-0</i>	-0,0554471	0,72595	0,793628	-0,403214	0,02605	0,0515615
<i>rps-1</i>	0,0212322	0,8892	0,918971	-0,387938	0,02	0,0411385
<i>rps-2</i>	-0,127283	0,3996	0,499264	-0,361559	0,02675	0,0527449
<i>rps-3</i>	-0,213225	0,17315	0,253992	-0,378059	0,02385	0,0477946
<i>rps-4</i>	-0,0554998	0,71655	0,786157	-0,289608	0,07905	0,132513
<i>rps-5</i>	-0,08928	0,55215	0,643864	-0,316776	0,05535	0,0981064
<i>rps-6</i>	-0,121893	0,41785	0,517305	-0,451637	0,00745	0,0175901
<i>rps-7</i>	-0,0225326	0,88295	0,914548	-0,460565	0,0083	0,0192986
<i>rps-8</i>	0,0134197	0,9279	0,947863	-0,352314	0,0296	0,0575059
<i>rps-9</i>	-0,0542589	0,72425	0,792288	-0,358671	0,03595	0,0678981
<i>rps-10</i>	-0,0376392	0,80355	0,854717	-0,603792	0,0003	0,00105745
<i>rps-11</i>	-0,16795	0,2657	0,358852	-0,540263	0,0013	0,00384632
<i>rps-12</i>	-0,202909	0,18845	0,27232	-0,421657	0,0048	0,0120038
<i>rps-13</i>	-0,120878	0,4085	0,508187	-0,233273	0,1214	0,189724
<i>rps-14</i>	-0,0643183	0,66725	0,74487	-0,286587	0,06785	0,116548
<i>rps-15</i>	-0,0150836	0,9199	0,941752	-0,372125	0,01835	0,038214
<i>rps-16</i>	-0,11817	0,44765	0,546514	-0,28036	0,07195	0,122439
<i>rps-17</i>	0,0162838	0,9123	0,936214	-0,254753	0,0912	0,149502
<i>rps-18</i>	0,016067	0,91595	0,938953	-0,229708	0,136	0,208267
<i>rps-19</i>	-0,0911308	0,61845	0,70262	-0,293647	0,0915	0,149932
<i>rps-20</i>	-0,00380725	0,9778	0,983998	-0,374023	0,01805	0,0376738
<i>rps-20</i>	-0,00380725	0,9778	0,983998	-0,374023	0,01805	0,0376738
<i>rps-21</i>	-0,0607083	0,6824	0,757788	-0,569287	0,0001	0,00039319
<i>rps-22</i>	0,0150132	0,91875	0,940921	-0,376659	0,01365	0,0296473
<i>rps-23</i>	-0,169725	0,27445	0,368467	-0,407884	0,0146	0,0314196
<i>rps-24</i>	-0,0306481	0,84315	0,88492	-0,469857	0,0049	0,0122236
<i>rps-25</i>	-0,100609	0,49875	0,594598	-0,587305	0,00025	0,000899945
<i>rps-26</i>	-0,100262	0,504	0,599489	-0,462001	0,0031	0,00818628
<i>rps-27</i>	0,0936417	0,522	0,616147	-0,238527	0,10025	0,161884
<i>rps-28</i>	0,0151955	0,91605	0,939024	-0,411338	0,00495	0,0123333
<i>rps-29</i>	-0,169695	0,24785	0,340213	-0,41054	0,0039	0,0100143
<i>rps-30</i>	-0,0210184	0,8895	0,919168	-0,405994	0,00925	0,0211991
<i>mrpl-1</i>	-0,407047	0,01095	0,0245379	-0,355649	0,02325	0,0467635
<i>mrpl-2</i>	-0,254794	0,1046	0,167671	-0,380698	0,01285	0,0281532
<i>mrpl-4</i>	-0,367722	0,02895	0,0564076	-0,285308	0,07075	0,120762
<i>mrpl-9</i>	-0,184847	0,2302	0,320673	-0,422092	0,0068	0,0162469

mrpl-10	-0,432665	0,0235	0,0471961	-0,46841	0,00505	0,0125433
mrpl-11	-0,281674	0,07615	0,128403	-0,286951	0,066	0,113838
mrpl-12	-0,543537	0,0033	0,00864957	-0,635227	0,00005	0,000207195
mrpl-13	-0,252278	0,14225	0,216089	-0,21827	0,191	0,275308
mrpl-14	-0,195357	0,5046	0,600071	-0,406159	0,04405	0,0807734
mrpl-15	-0,363456	0,0205	0,0420044	-0,26728	0,0811	0,135465
mrpl-16	-0,395162	0,0187	0,0388347	-0,407636	0,01075	0,0241527
mrpl-17	-0,504605	0,00355	0,00922723	-0,54937	0,0005	0,00166607
mrpl-18	-0,588881	0,00065	0,0020946	-0,342936	0,0363	0,0684663
mrpl-19	-0,482743	0,306	0,40265	-0,429387	0,2182	0,306676
mrpl-20	-0,545373	0,0023	0,00631799	-0,248884	0,13155	0,202638
mrpl-21	-0,4527	0,01165	0,0259044	-0,343335	0,0421	0,0777265
mrpl-22	-0,273272	0,09835	0,15926	-0,312482	0,045	0,082266
mrpl-23	-0,21959	0,193	0,277707	-0,486772	0,00295	0,00784561
mrpl-24	-0,506351	0,02245	0,0453928	-0,430541	0,0164	0,0347051
mrpl-28	-0,379139	0,1098	0,17463	-0,384523	0,0548	0,0972835
mrpl-30	-0,366313	0,0356	0,0673283	-0,394639	0,01505	0,0322221
mrpl-32	-0,495308	0,0039	0,0100143	-0,483728	0,00465	0,0116757
mrpl-34	-0,410472	0,03275	0,0627582	-0,235861	0,1829	0,265686
mrpl-35	-0,375008	0,14585	0,22057	-0,501451	0,0244	0,0487406
mrpl-36	-0,398213	0,02645	0,0522374	-0,399316	0,02815	0,0550648
mrpl-37	-0,237649	0,1356	0,207752	-0,311061	0,0397	0,0739145
mrpl-38	-0,435639	0,0059	0,0143688	-0,590718	0,0001	0,00039319
mrpl-39	-0,509574	0,00265	0,00715036	-0,349963	0,02795	0,05474
mrpl-40	-0,560667	0,0011	0,00332335	-0,445609	0,0066	0,0158299
mrpl-41	-0,298979	0,0811	0,135465	-0,496681	0,0015	0,00435783
mrpl-45	-0,474439	0,0032	0,00841964	-0,35422	0,01815	0,0378541
mrpl-46	-0,421145	0,01535	0,032788	-0,447441	0,00695	0,0165605
mrpl-47	-0,348851	0,03245	0,0622612	-0,333803	0,034	0,064758
mrpl-49	-0,559755	0,0018	0,0051039	-0,556849	0,00065	0,0020946
mrpl-50	-0,326323	0,0397	0,0739145	-0,326551	0,03525	0,0667529
mrpl-51	-0,527479	0,0013	0,00384632	-0,404869	0,01055	0,0237684
mrpl-53	-0,142574	0,44815	0,546994	-0,312471	0,07865	0,131948
mrpl-54	-0,503751	0,0096	0,0218921	-0,441019	0,0148	0,0317809
mrpl-55	-0,408218	0,0244	0,0487406	-0,285277	0,09745	0,158026
mrps-2	-0,342217	0,034	0,064758	-0,408751	0,0092	0,021104
mrps-5	-0,227649	0,1341	0,205852	-0,389671	0,0097	0,0220916
mrps-6	-0,34462	0,03515	0,0665951	-0,376901	0,01835	0,038214
mrps-7	-0,32704	0,0538	0,0957449	-0,359838	0,0274	0,0538084
mrps-9	-0,432919	0,0077	0,0181004	-0,351067	0,0217	0,0441024
mrps-10	-0,568513	0,00135	0,00397506	-0,422016	0,0115	0,0256087
mrps-11	-0,234837	0,16935	0,249317	-0,372944	0,0444	0,0813276
mrps-12	-0,173542	0,3058	0,402474	-0,524596	0,0017	0,0048631

<i>mrps-14</i>	-0,196933	0,20735	0,294243	-0,226176	0,1442	0,218499
<i>mrps-15</i>	-0,505701	0,0018	0,0051039	-0,586088	0,00005	0,000207195
<i>mrps-16</i>	-0,530221	0,0093	0,0213026	-0,526762	0,00245	0,00667993
<i>mrps-17</i>	-0,36746	0,0382	0,0714998	-0,332891	0,0494	0,0891135
<i>mrps-18A</i>	-0,256688	0,1183	0,185783	-0,322472	0,0539	0,0958913
<i>mrps-18B</i>	-0,160042	0,34455	0,442742	-0,255514	0,11025	0,175179
<i>mrps-18C</i>	-0,404966	0,01	0,0226872	-0,376864	0,01155	0,0257044
<i>mrps-21</i>	-0,484927	0,00845	0,0196052	-0,340775	0,0449	0,0821256
<i>mrps-22</i>	-0,547951	0,00055	0,00181303	-0,368221	0,01665	0,0351758
<i>mrps-23</i>	-0,448085	0,29475	0,390587	-0,362013	0,159	0,236546
<i>mrps-24</i>	-0,409435	0,01895	0,0392714	-0,0916259	0,5774	0,666829
<i>mrps-25</i>	-0,32144	0,0581	0,102241	-0,406926	0,01105	0,024733
<i>mrps-26</i>	-0,32656	0,0398	0,0740707	-0,496053	0,00095	0,0029233
<i>mrps-28</i>	-0,304642	0,07885	0,13223	-0,200263	0,22755	0,317487
<i>mrps-30</i>	-0,482744	0,00275	0,00738291	-0,552709	0,0001	0,00039319
<i>mrps-31</i>	-0,551927	0,001	0,00305761	-0,461803	0,00365	0,00945241
<i>mrps-33</i>	-0,29977	0,08785	0,144863	-0,643586	0,00005	0,000207195
<i>mrps-34</i>	-0,630994	0,00045	0,00151768	-0,470516	0,00315	0,0083021
<i>mrps-35</i>	-0,439752	0,0064	0,0154134	-0,510405	0,0006	0,00195417

Supplementary Table 2: Ribosomal protein total and polysome-associated mRNAs in *pycr-1(wrm22)*

Identifier	Genotype
MSD331	N2 Bristol wildtype
CB4856	Hawaiian wildtype
CB1370	<i>daf-2(e1370)III.</i>
AD405	<i>eat-2(ad495)II.</i>
AA1074	<i>glp-1(2141ts)III.</i>
MSD348	<i>pycr-1(wrm22)X.</i>
MSD406	<i>rsk-1(sv31)III.</i>
YY178	<i>eri-1(mg366)IV::gglS1[GFP::nrde-3]</i>
MSD545	<i>eri-1(mg366)IV::gglS1[GFP::nrde-3];pycr-1(wrm22)X.</i>

Supplementary Table 3: Worm strains used in this study

Identifier	Vector backbone / plasmid	Source / construction information
CELE_BA1811	HT115 [L4440:: <i>luciferase</i>]	A. Antebi. <i>luc2</i> cloned from pGL4.11
CELE_M153.1	HT115 [L4440:: <i>pycr-1</i>]	Ahringer RNAi library
CELE_F29G6.3	HT115 [L4440:: <i>hpo-34</i>]	Ahringer RNAi library
CELE_trpp-9	HT115 [L4440:: <i>trpp-9</i>]	Ahringer RNAi library
CELE_ZK889.6	HT115 [L4440:: <i>ZK889.6</i>]	Ahringer RNAi library
CELE_C49F5.1	HT115 [L4440:: <i>sams-1</i>]	Vidal RNAi library
CELE_C06E7.1	HT115 [L4440:: <i>sams-3</i>]	Vidal RNAi library
CELE_C06E7.3	HT115 [L4440:: <i>sams-4</i>]	Vidal RNAi library
CELE_T13A10.11	HT115 [L4440:: <i>sams-5</i>]	Vidal RNAi library
CELE_C01B10.8	HT115 [L4440:: <i>C01B10.8</i>]	Vidal RNAi library
CELE_C23G10.7	HT115 [L4440:: <i>C23G10.7</i>]	Vidal RNAi library
CELE_C37A2.6	HT115 [L4440:: <i>C37A2.6</i>]	Vidal RNAi library
CELE_C09H5.2	HT115 [L4440:: <i>catp-3</i>]	Vidal RNAi library
CELE_Y57G11C.24	HT115 [L4440:: <i>eps-8</i>]	Vidal RNAi library
CELE_F25H2.12	HT115 [L4440:: <i>F25H2.12</i>]	Vidal RNAi library
CELE_K07H8.10	HT115 [L4440:: <i>K07H8.10</i>]	Vidal RNAi library
CELE_W02B12.10	HT115 [L4440:: <i>metl-1</i>]	Vidal RNAi library
CELE_C18A3.1	HT115 [L4440:: <i>metl-4</i>]	Vidal RNAi library
CELE_C38D4.9	HT115 [L4440:: <i>metl-5</i>]	Ahringer RNAi library
CELE_ZK1058.5	HT115 [L4440:: <i>metl-6</i>]	Vidal RNAi library
CELE_T03G11.6	HT115 [L4440:: <i>metl-9</i>]	Vidal RNAi library
CELE_F32A7.4	HT115 [L4440:: <i>metl-17</i>]	Vidal RNAi library
CELE_K01A11.2	HT115 [L4440:: <i>metl-18</i>]	Vidal RNAi library
CELE_T20F5.3	HT115 [L4440:: <i>mrrf-1</i>]	Ahringer RNAi library
CELE_Y53F4B.4	HT115 [L4440:: <i>nsun-5</i>]	Vidal RNAi library
CELE_R17.2	HT115 [L4440:: <i>pde-12</i>]	Vidal RNAi library
CELE_F07D10.1	HT115 [L4440:: <i>rpl-11.2</i>]	Vidal RNAi library
CELE_F55D10.2	HT115 [L4440:: <i>rpl-25.1</i>]	Vidal RNAi library
CELE_F45G2.9	HT115 [L4440:: <i>F45G2.9</i>]	Vidal RNAi library
CELE_T07A9.8	HT115 [L4440:: <i>susi-2</i>]	Vidal RNAi library
CELE_Y53C10A.12	HT115 [L4440:: <i>hsf-1</i>]	Ahringer RNAi library
CELE_W07G4.4	HT115 [L4440:: <i>lap-2</i>]	Ahringer RNAi library
CELE_F37B12.2	HT115 [L4440:: <i>gcs-1</i>]	Vidal RNAi library
CELE_R03D7.1	HT115 [L4440:: <i>metr-1</i>]	Ahringer RNAi library
CELE_T13G4.4	HT115 [L4440:: <i>T13G4.4</i>]	Ahringer RNAi library
CELE_D2005.5	HT115 [L4440:: <i>drh-3</i>]	Vidal RNAi library
CELE_W01B11.3	HT115 [L4440:: <i>nol-58</i>]	Ahringer RNAi library
CELE_C14A4.4	HT115 [L4440:: <i>crn-3</i>]	Vidal RNAi library
CELE_C06E1.10	HT115 [L4440:: <i>rha-2</i>]	Ahringer RNAi library

CELE_M01B12.5	HT115 [L4440:: <i>riok-1</i>]	Ahringer RNAi library
CELE_T06E6.1	HT115 [L4440:: <i>T06E6.1</i>]	Ahringer RNAi library
CELE_T22H9.1	HT115 [L4440:: <i>T22H9.1</i>]	Ahringer RNAi library
CELE_ZK686.2	HT115 [L4440:: <i>ZK686.2</i>]	Ahringer RNAi library
CELE_F18E9.5	HT115 [L4440:: <i>jmjd-3.1</i>]	Ahringer RNAi library
CELE_F2312.5	HT115 [L4440:: <i>jmjd-3.2</i>]	Ahringer RNAi library
CELE_D2021.1	HT115 [L4440:: <i>utx-1</i>]	Ahringer RNAi library
CELE_F41E6.13	HT115 [L4440:: <i>atg-18</i>]	Vidal RNAi library
CELE_T19E7.3	HT115 [L4440:: <i>bec-1</i>]	Vidal RNAi library
CELE_R13H8.1	HT115 [L4440:: <i>daf-16</i>]	Ahringer RNAi library
CELE_ZK112.2	HT115 [L4440:: <i>ncl-1</i>]	A. Antebi. <i>luc2</i> cloned from pGL4.11
CELE_T19E7.2	HT115 [L4440:: <i>skn-1</i>]	Vidal RNAi library
CELE_R74.3	HT115 [L4440:: <i>xbp-1</i>]	Vidal RNAi library
CELE_R04A9.2	HT115 [L4440:: <i>nrde-3</i>]	Ahringer RNAi library

Supplementary Table 4: Bacterial strains used for RNAi in this study

Target	Direction	Sequence 5' to 3'
<i>pycr-1(wrm22) and pycr-1(syb2745)</i>	Forward	CACGTGACCTTGCTCTGAAG
<i>pycr-1(wrm22) and pycr-1(syb2745)</i>	Reverse	TCAGGCCAAGTGACCCTATT
<i>pycr-1(syb2874)</i>	Forward	CTTTCTTGTTTAGATTTTTCTCAAAATG
<i>pycr-1(syb2874)</i>	Reverse	CAGGGAAATTTGTAAATTTTCTGCAC
<i>eft-3</i>	Forward	GTAAGGGATCTTTCAAGTACGC
<i>eft-3</i>	Reverse	CATCGATGATGGTGATGTAGTAC
pre-rRNA #1	Forward	TCATTGCGCCGATCCATAGAT
pre-rRNA #1	Reverse	CAAGACCAATACCGCAACATCA
pre-rRNA #2	Forward	CACGGTCAGTTGAGTGTCGA
pre-rRNA #2	Reverse	GTAGTTTTGGAATAACTGCCACG
pre-rRNA #3	Forward	TATCGGAGGAGCTGCCAAATGG
pre-rRNA #3	Reverse	GGAGCGACGACACATTCTGAC
pre-rRNA #4	Forward	GGACACACCACCAAAGTCTCAA
pre-rRNA #4	Reverse	TTGAGAGACGGCAGACAACG
5.8S #1	Forward	TTGCTGCGTTACTTACCA
5.8S #1	Reverse	GAACCAGACGTACCAACT
18S #1	Forward	ATACCTGATTGATTCTGTC
18S #1	Reverse	TTCCGCAGTTATCCATAT
18S #2	Forward	CATTAGGACTGACAGATTGAA
18S #2	Reverse	TCGCTCGTTATCGGAATA
18S #3	Forward	AACCGTTGAAATTCTTCCA
18S #3	Reverse	GCTGATGACTCACACTTAC
26S #1	Forward	TGAACTCAGTCGTGATTACC
26S #1	Reverse	CACTCGCCGTTACTAAGG
26S #2	Forward	GTTTAGTTACGCTAGTGTG
26S #2	Reverse	CAATCCGTGTTTCAAGAC
26S #3	Forward	GGAATCCGACTGTCTAAT
26S #3	Reverse	CGCTTACTCGAATTACTAC
L4440	Forward	TACGACTCACTATAGGGAGAC
L4440	Reverse	CCACTCACGACGTTGTAAAACG

Supplementary Table 5: Primers used in this study

Appendix

Acknowledgments

First and foremost, I want to thank my family, especially my mother Ellen. They have always supported my ambition for science. Even though I might not have picked the easiest University bachelors' study for me, and that it took me *a bit* longer for finishing it, you always believed in me. Thank you for the unwavering support that allowed me to follow up on my dream to become a scientist.

I want to thank my sister Sandra and my brother-in-law Earl Waal. We will always remember the *amazing* housing opportunities we came across. You were also there when I took my first baby steps into the Denzel lab. Still waiting for you to pick me up.

I also want to express my thanks to Dennis Rütze and Padriac Déseach, who helped me move my belongings and furniture on several daunting travels. Even a blizzard and careless drivers can't stop us.

The Denzel lab feels like a family, and will always be so. I thank all current and previous members for helpful work and non-work-related discussions. We are a great and successful team.

I want to express great thanks to boss and supervisor Martin Denzel for the great experiences we have shared. You welcomed me as a master student into your lab and I am grateful for the opportunities you provided me to do science in an amazing team and excellent scientific environment. You helped shape me as a scientist, and I am grateful for that. I think, through our trials and tribulations, we have learned to become a great team and I am excited to continue working together.

There are many current and previous lab members of both the Denzel lab as the Antebi lab that I would like to express my gratitude to, which I will do in person. I want to mention a few. I want to thank Gabe for eating lots of falafel with me at the beginning of our Germany adventure. I want to thank Maxime and Sabine for excellent collaborations. I want to thank Virginia and Kira for providing that family feeling. You were there for me always to support me, and your input has been tremendously valuable.

I thank the Antebi lab for providing worm strains, bacterial RNAi clones, and many things more. Moreover, the Antebi lab has been a great source of scientific input and welcome distractions. I want to thank Adam Antebi for creating an environment for out of the box thinking and excellent scientific environment for me to grow in.

Although he has left the institute for some years now, Christoph Geisen I will always remember fondly. In fact, I am writing at this moment at his old dining table. I will be happily taking this sturdy table, with its characteristic scratches, with me for some more years. The two have some

things in common. Thanks, you have been a great help in the development of my first years at the institute.

I will miss, already do, my favorite lunch buddies Andrea Annibal, Christian Latza and Joachim Steiner. Even when we took more than an hour, it was time well spent. It helped keep my sanity in check, provide comic relief, and provided critical insights into our personal lives, but also scientifically.

I want to thank Dennis Gadalla, Anchal Srivastava and Sebastian Grönke from the Partridge lab for excellent collaboration. Moreover, I want to thank Linda Partridge for her scientific input that helped mature my project.

I want to thank Daniela Morick, the PhD coordinator at our institute, for her reminders and quick thinking, to guide me through all the procedures that come with being part of a graduate school, which I did not always give much attention to.

I want to thank the members of my advisory committee David Vilchez and Peter Tessarz. You were instrumental for the development of my project. Thank you for the time to attend the meetings and giving me valuable feedback for my PhD thesis.

I want to thank my thesis committee members Björn Schumacher and Ulrich Baumann for agreeing to evaluate my thesis and participate in my defense.

There are some additional professional thanks I want to express. First and foremost, I want to thank all the scientific and administrative support, from the front to the back-end, that the Max Planck Institute for Biology of Ageing provides. I thank Shouhong Guang from the University of Science and Technology of China for providing worm strains. I thank the CGC for providing worm strains, which is funded by the NIH Office of Research Infrastructure Programs (P40 OD010440). I thank Silvina Perin, Yvonne Hinze, and Patrick Giavalisco from the MPI AGE metabolomics core facility. I thank Franziska Metge, Ayesha Iqbal, and Jorge Boucas from the MPI AGE bioinformatics core facility. Mass spectrometry proteomics analysis was performed in the MPI AGE proteomics core facility. I thank Xinping Li and Ilian Atanassov from the MPI AGE proteomics core facility. This work was supported by the European Commission (ERC-2014-StG-640254-MetAGEn), and by the Max Planck Society.

I have not mentioned you, or I could have done a better job, gratitude is expressed best in person anyway!

Work contributions

I performed all the experiments described in this thesis independently, except for:

All mouse experiments were done by Anchal Srivastava and Sebastian Grönke from the laboratory of Linda Partridge at the MPI AGE.

All fly experiments and analyses were done by Dennis S. Gadalla and Sebastian Grönke from the laboratory of Linda Partridge at the MPI AGE.

Paraquat survival assays were performed by Gabriel A. Guerrero from the laboratory of Martin Denzel at the MPI AGE.

Heat stress survival assays and polysome footprinting experiments were performed by Maxime J. Derisbourg from the laboratory of Martin Denzel at the MPI AGE. He also prepared the samples for mass spectrometry proteomics analysis.

Mass spectrometry proteomics analysis was performed by Xingping Li and Ilian Atanassov in the MPI AGE proteomics core facility.

LC-MS analysis was performed by Silvina Perin, Yvonne Hinze, and Patrick Giavalisco from the MPI AGE metabolomics core facility.

The *pycr-1(syb2745)* and *pycr-1(syb2874)* *C. elegans* alleles were generated by SunyBiotech (China).

Whole genome sequencing was done at the Cologne Center for Genomics.

I want to express my sincere gratitude for their important contributions.